A STATISTICAL METHOD FOR DETERMINING AND REPRESENTING FORMABILITY

Innovation Report

by

Neil Small

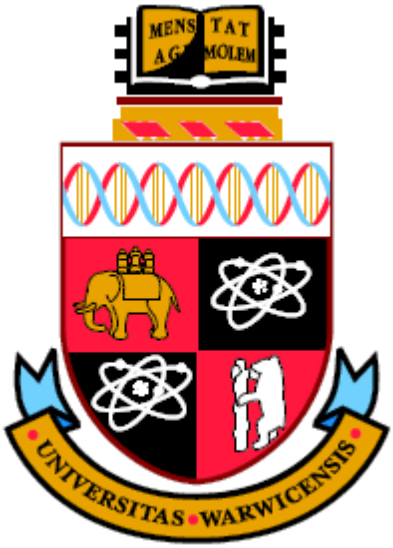

An innovation report submitted in partial fulfilment of the requirements for the degree of

Engineering Doctorate

University of Warwick, Warwick Manufacturing Group

June 2015

“If at first you don’t succeed,
Try, try, try again”

Proverb

ABSTRACT

Formability, conventionally characterised by the Forming Limit Curve (FLC), is a critical measure used to define the working limit of sheet metal in a forming operation. The FLC defines the limit strain the material can undergo before failure occurs. The importance of this failure criterion means it is used at various stages in the development of automotive body panels: during material selection; during stamping simulations; and in the purchase of stamping tools before commencing serial production.

To mitigate against the risk that the FLC is positioned incorrectly; that mechanical property variation between blanks causes reduced formability; and that conditions imposed by the stamping operation itself cause premature failure, a safety margin is introduced. The size of the safety margin is based on the industrial sponsor's prior experience and attitude to risk, as opposed to an objective analysis of each of the risks posed to formability. Uncertainty around the position of an FLC arises from the dispersed limit strains that characterise the results of standardised formability tests. The aim of this research was to understand and characterise the uncertainty of the formability test, and develop a more accurate and precise method for determining and representing formability.

Initial tests were carried out according to the standard ISO method, and a digital image correlation (DIC) technique was used to measure full-field strains on each specimen throughout the tests. Two observations were made. Firstly, the method of analysis advocated by the ISO standard requires subjective interpretation to define a limit strain. Secondly, the full-field strain measurements showed a "noisy" strain distribution overlaid over the expected strain field. This "noise" was significant compared to the uncertainty of the DIC instrument.

A solution was developed by adopting a statistical attitude to model surface strain measurements. Strains from the beginning of deformation up to fracture were characterised by a fundamental analysis. The analysis showed that the forming limit of an individual test is statistical in nature, and that the strains' statistical character exhibits recognisable trends that evolve from the start of the tests up to necking. A new 'time-dependent' method based on the innovative application of a Gaussian Mixture Model (GMM) was developed to characterise these trends, and quantify the forming limit. The GMM was used to objectively identify the locus of a localised neck; identify the onset of necking; and characterise the neck at the forming limit. Rather than selectively analysing strains in a pre-determined area of a specimen, and at a selected time of the test, the developed technique eliminates the subjectivity that is required by the current ISO-standard method.

The new GMM technique describes formability as a probabilistic risk of failure. Strain measurements made on single specimens were turned into a complimentary statistical formability criterion using the logistic regression technique proposed by **Strano & Colosimo** (**2006**). Formability Maps (FMs) were constructed to show the probability of failure contours on the Forming Limit Diagram (FLD). FMs derived from the GMM provide the precise representation of formability that is missing from the FLC, and that is required to objectively interpret the risk of failure for an industrial panel.

It was postulated that the presence of a surface roughness is responsible for surface strain variation because of the geometry of its asperities. Its evolution is controlled by underlying changes to the microstructure during the course of plastic deformation. A modified M-K model was used to predict the range of strains that arise from surface roughening at the forming limit. Formability predictions correspond well to FLCs drawn from ISO-standard limit strains, but less well to the FMs drawn from the GMM. It was concluded that surface roughening alone does not explain the heterogeneous strain behaviour measured in this research.

DECLARATION

This innovation report is submitted to the University of Warwick in support of my application for the degree of Engineering Doctorate. It has been composed by myself, and is being resubmitted following the recommendations of the examination panel subsequent to the oral examination which was conducted on 19/05/14.

The work presented (including data generated and data analysis) was carried out by myself, except where explicitly stated.

ENGINEERING DOCTORATE MENTORS

Academic Mentors: Dr Sumit Hazra, Prof Rajat Roy, Dr Darren Hughes
Industrial Mentor: Mr Richard Aylmore

INDUSTRIAL SPONSOR

Jaguar Land Rover, Abbey Road, Whitley, Coventry, CV3 4LF, UK

ACKNOWLEDGEMENTS

I wish to offer my deepest thanks for the assistance and guidance I have received from Dr Sumit Hazra. This project would not have been nearly as enjoyable without Sumit's unwavering patience, enthusiasm, and support.

I would like to thank Dave Williams and Professor Rajat Roy from WMG for their many words of wisdom, and their constructive feedback and support. Thanks also to Dr Tom Nichols for providing an informative insight and engaging discussions on the application and intricacies of statistical models.

From Jaguar Land Rover, I would like to thank Richard Aylmore and Dominic Hollingdale for their support and direction throughout this process.

I would like to thank everyone at WMG and Jaguar Land Rover who have provided me with their time, assistance, and expert knowledge.

I am grateful to both the Engineering and Physical Sciences Research Council and Jaguar Land Rover for financially supporting this project.

I am also grateful to my examiners not only for dedicating their valuable time to reading my research, but also for providing me with clear and concise feedback.

Finally, thank you to all of my family and friends who have helped and supported me. Thank you for helping me retain at least a modicum of sanity after the all the long working days, evenings, and weekends.

CONTENTS

LIST OF FIGURES

LIST OF TABLES

GLOSSARY

ACRONYMS

ANOVA	Analysis of Variance
BCC	Body Centre Cubic
BiW	Body-in-White
CCD	Charge-Coupled Device
CGA	Circle Grid Analysis
DIC	Digital Image Correlation
EBSD	Electron Back-Scatter Diffraction
EDA	Exploratory Data Analysis
EM	Expectation Maximization
EU	European Union
FCC	Face Centre Cubic
FLB	Forming Limit Band
FLC	Forming Limit Curve
FLC_0	Major limit strain in plane strain
FLD	Forming Limit Diagram
FLSC	Forming Limit Stress Curve
FM	Formability Map
GMM	Gaussian Mixture Model
HCP	Hexagonal Close Packed
ISO	International Organization for Standardization
KDE	Kernel Density Estimation
M-K	FLC prediction model developed by **Marciniak & Kuczyński** (**1967**)
MKG	Strain analysis technique of **Merklein et al.** (**2010**)
NEDC	New European Driving Cycle
PDF	Probability Density Function
PLC	Portevin-Le-Chatelier effect
SEM	Scanning Electron Microscopy
VH	Strain analysis technique of **Volk & Hora** (**2010**)
WMG	Warwick Manufacturing Group

MATHEMATICAL SYMBOLS

Plasticity Modelling

$\overline{\sigma}_0$	Initial yield stress
$\overline{\sigma}_{sat}$	Stress at hardening curve saturation point
σ_b	Stress in equibiaxial tension
σ_i	Principal stress, where *i* = 1, 2, 3
σ_p	Stress in plane strain
$\overline{\sigma}$	Flow stress
$\overline{\varepsilon}$	Equivalent strain
$\dot{\varepsilon}$	Strain rate

ε_i	Principal strain, where *i* = 1, 2, 3
ε_i^*	Principal limit strain
ρ	Strain path
K	Strength coefficient in power law hardening models
ΔR	Planar anisotropy
$\overline{R}$	Normal anisotropy
R_i	Anisotropy at angle to rolling direction, where i = 0°, 45°, 90°
R'	Surface roughness
R'_{max}	Maximum surface roughness
α, p	Dimensionless, material-dependent constants in **Voce** (**1948**) and **Hockett & Sherby** (**1975**) hardening models
P	Parameter to determine sharpness of yield curve, as proposed by **Barlat** (**1987**)
θ	Angular parameter to determine sharpness of yield curves, as proposed by **Friedman & Pan** (**2000**)
d	Average grain diameter
f_0	Initial heterogeneity coefficient of M-K model
f	Heterogeneity coefficient of M-K model
m	Strain rate hardening exponent
n	Strain hardening exponent
$t_0^{a,b}$	Initial thickness in regions A and B of the M-K specimen
$t^{a,b}$	Thickness of regions A and B of the M-K specimen
φ	Angle of imperfection in the M-K specimen

Statistical Modelling

π_k	Mixture weight, where *k* = 1, 2
σ^2	Variance of a population
μ	Mean of a population
σ	Standard deviation of a population
ϑ	Vector of parameter defining a PDF
a, b, c, d, e	Coefficients fitted to logistic regression models
$\hat{a}, \hat{c}, \hat{d}$	Regression coefficients estimated using maximum likelihood
c	Experimentally derived constant relating surface roughness to grain size
g_k	GMM component denotation, where *k* = 1, 2
n	Number of observations (in statistical models)
y	Response variable in a linear regression model
z	Response variable in a logistic regression model
E	Model error
N	Gaussian distribution function
P_i	Probability of observing an outcome *i*
$\boldsymbol{X}$	Predictor variable structure in a linear regression model

1 INTRODUCTION

1.1 THE MOTOR INDUSTRY IN 2014

New car buyers in 2014 have high expectations surrounding the capability and flexibility of their prospective purchase. Whereas previous generations of vehicle enticed potential owners through safety and reliability accolades, these traits have now become expected characteristics in the modern vehicle. Manufacturers have gravitated towards offering vehicles styled at the forefront of the latest fashion, incorporating the latest technological and infotainment innovations, and providing the flexibility to specify an array of personalised options to attract customers.

The addition of personalised options such as air conditioning units, heated seats, and surround sound audio systems increases a vehicle's weight. Over the past decade the widening variety of available options, in conjunction with advances in occupant safety structures, has caused vehicles' weights to increase. Statistics compiled in a report by the **European Commission** (**2013**) demonstrate that the gross weight of the average passenger vehicle sold in Europe has increased from 1696kg in 2001 to 1864kg in 2012. To ensure that dynamic performance is not compromised, the same report demonstrates the power of the average passenger vehicle sold in Europe has risen from 74KW in 2001 to 89KW in 2012.

Modern vehicle design is influenced by factors over and above specifications defined by safety legislation and consumer trends. A developing influence in recent years has been the impact of vehicles on the environment. Greater awareness has resulted in vehicle manufacturers becoming increasingly accountable for the environmental impact of a vehicle over its life cycle. The Kyoto protocol (**1998**) is regarded as the catalyst for this change, where 191 countries signed an agreement to reduce their respective greenhouse gas emissions. As one of the primary causes of greenhouse gases, the constituents of tailpipes emissions have become subjected to increasingly stringent legislature.

The European Union (EU) regulates tailpipe emissions through a dedicated directive. In 1992, EURO I was introduced to govern the amount of gases including carbon dioxide, hydrocarbons, and nitrogen oxides which can be emitted by new passenger vehicles. The directive is now in its sixth iteration (EURO VI). The acceptable level of each gas has incrementally decreased in each directive to mirror the desire to continually reduce global greenhouse gas emissions. A further driver was introduced in 2012 in the form of a financial penalty system. Vehicle manufacturers whose European fleet average exceeds the EU carbon dioxide target are penalised for each vehicle sold. The fleet average target for 2007 was 158.7g/km. This target will reduce to 130g/km by 2015, and to 90g/km by 2021. Penalties are imposed on an incremental scale, depending on how far targets are exceeded. Currently, if the fleet average is 1g/km over target the manufacturer is penalised €5 per vehicle. For every subsequent g/km over target the severity of the penalty increases. In 2019 the penalty system will change such that manufacturers will incur a penalty of €95 for every g/km of above the threshold.

The ability to balance the demands and desires of consumers with ever-tightening environmental regulation is a challenge for vehicle manufacturers. The **Department for Business Innovation and Skills** (**2009)**, in conjunction with representatives from high and low volume vehicle manufacturers, commissioned a study to identify the technological and infrastructural developments required to meet these challenges. The results of this study included a product development roadmap, shown in Figure 1, which demonstrates the developments required for structural, powertrain, and design systems.

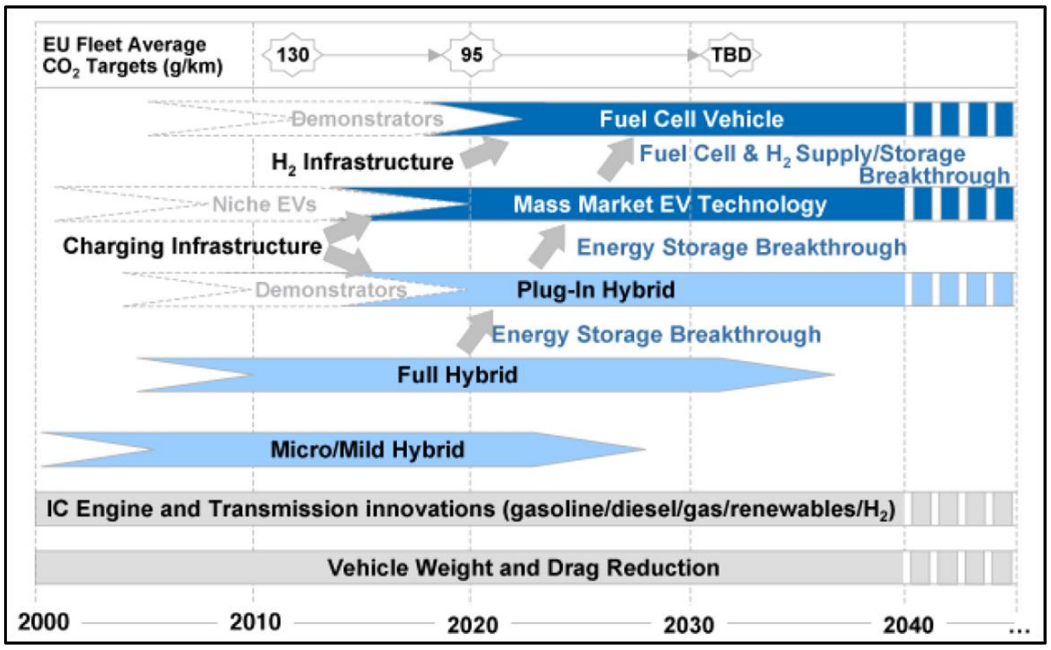

Figure 1: Roadmap for technology improvement proposed in 2009 by the Department for Business Innovation and Skills **(**2009**)**

The roadmap anticipates that weight reduction will consistently feature in vehicle technology development over the coming decades. Vehicle weight reduction through the application of lightweight materials and technologies has a positive effect on fuel saving. Fuel saving is achieved through the direct and indirect effects of weight reduction. The **European Aluminium Association** (**2013**) define the savings benefits as follows:

- Direct weight saving: Weight saving arising from replacing a heavier material with a lighter material in one or several components
- Indirect weight saving: Weight saving from downsizing components (e.g. engine, suspension) while retaining vehicle performance as a result of direct weight loss elsewhere on the vehicle
- Primary fuel saving: Fuel saved from the lower energy demand required to move a vehicle of reduced weight
- Secondary fuel saving: Additional fuel saving obtained by optimising a downsized powertrain system to deliver performance equal to that of the original vehicle

Not only does fuel saving benefit the customer by reducing running costs, it also minimises the vehicle's environmental impact. CO_2 emission benefits obtainable through weight and fuel saving have been calculated by the **European Aluminium Association** (**2013**) and are demonstrated in Table 1. These figures are based on simulations of a 2009 VW Golf 1.4 TSI being driven according to the New European Driving Cycle (NEDC) presented by **Koffler & Rohde-Brandenburger** (**2009**).

	Direct Weight Savings (100kg)	**Direct + Indirect Weight Savings (150kg)**
Primary Fuel Savings	3.6g/km	5.4g/km
Primary + Secondary Fuel Savings	8.4g/km	12.7g/km

Table 1: Achievable reductions in CO_2 emissions through direct and indirect weight saving, calculated by the European Aluminium Association **(**2013**)**

The scope of this research concerns the development and implementation of lightweight materials and technologies. Specifically, this project is focussed on direct weight saving opportunities that are exploitable in car bodies.

1.2 Material Selection in Car Bodies

The Body-in-White (BiW) represents around 20% of a car's total weight. It is an ideal candidate to implement and realise direct weight saving. The BiW is the skeletal structure of the car, consisting predominantly of sheet metal components. Components are broadly categorised as either structural or skin panels. Structural panels (e.g. pillars, door and roof inners) form the internal structure of the body, providing body integrity and contributing to occupant safety. Skin panels (e.g. doors, fenders) are the external parts which enable cabin access and provide the vehicle's major aesthetic features.

Appropriate material selection is critical to ensure each component (and, subsequently, the vehicle) meets design intent. Structural panels require a high strength material to be able to support the weight of other systems within the vehicle and provide ideal crash deformation characteristics. Skin panel materials require high levels of formability to meet complex styling features whilst also resisting environmental degradation. Coated mild steels satisfy these requirements, and have been used to manufacture both types of panel.

The environmental demands discussed in Section 1.1 have focussed automotive manufacturers on substituting mild steel with alternative, lightweight materials - in particular aluminium alloys and high strength steels. Aluminium alloys enable weight saving by offering strengths similar to those of mild steels, but at 1/3rd the density. High strength steels are capable of supporting higher design loads through smaller cross-sectional areas. In recognition of the direct weight saving opportunities offered by these materials, the past decade has seen the contribution of both aluminium alloys and high strength steels in BiW manufacture increase. Jaguar Land Rover has been particularly prominent in integrating new materials into the BiW structure. The 2013 model Range Rover has over 80% of the BiW made of aluminium and high strength steel contributing towards a vehicle weight saving of ≈400kg over the previous incarnation.

1.3 Sheet Metal Forming

BiW panels are predominantly manufactured through stamping operations. A stamping toolset comprises a unique punch and die combination, with a sheet metal blank positioned at the interface. Forcing the punch and blank into the die cavity stretches the centre of the blank over the punch face, and draws the neighbouring region along the die wall and into the cavity. When the blank has been sufficiently plastically deformed, the blank retains the geometrical features of the die.

1.3.1 Formability

A material's formability is defined as its ability to undergo plastic deformation - in either stretching or drawing - without exhibiting a defect. Defects which can materialise in a stamping operation include splits, tears, wrinkles, and scores. Splits and tears occur when materials are subjected to positive planar stresses (stretching) - often seen in material deformed over the centre of punches. Wrinkling occurs when at least one principal stress is negative (drawing or compression) - often seen in material drawn along die walls, or material compressed within a binder system. Splits and tears are the most prominent defects in stretching operations. Both defects are preceded by measurable damage mechanisms. Initial damage is visible as a roughening of the sheet's surface. Continued loading leads to the occurrence of a thin band of reduced thickness. Critical damage occurs when the sheet is further deformed and the band experiences a thinning rate much higher than the remainder

of the sheet. Significant localised thinning reduces the sheet's load bearing ability, thereby instigating a split or tear. This critical damage mechanism is referred to as localised necking. Within the automotive industry, the onset of localised necking is the practical limit of formability.

1.3.2 The Forming Limit Curve

The Forming Limit Curve (FLC), shown in Figure 2, marks the onset of localised necking in sheet material over a range of strain paths. Since its conceptualisation by **Keeler** (**1961**) and **Goodwin** (**1968**), the FLC has become an almost ubiquitous formability criterion for analysing stretching operations. It is used for material selection, stamping simulation feasibility studies, and for tooling buy-off.

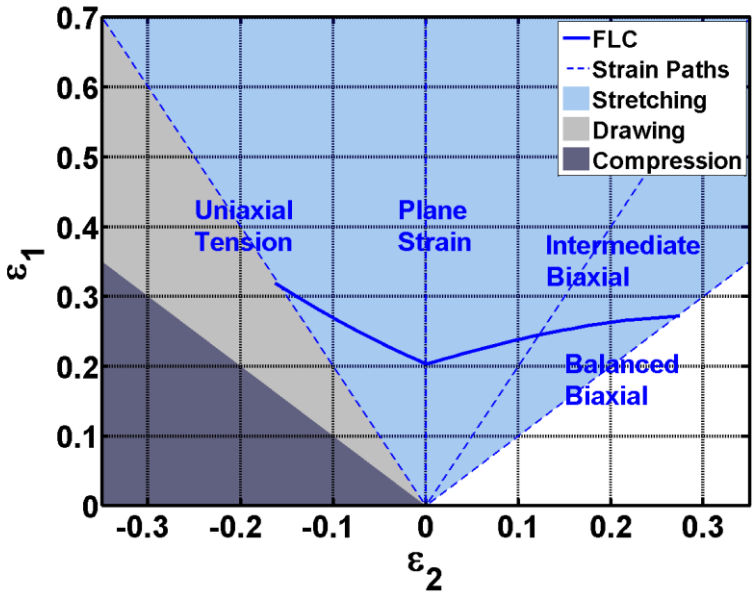

Figure 2: The Forming Limit Curve demonstrating relevant strain paths and forming modes

Each combination of material, thickness, and temper has a unique FLC. The height of the FLC provides a general indication of formability. Forming grade mild steels have high formability, reflected by their high FLCs. Lightweight materials such as aluminium alloys and high strength steels have low formability, as characterised by lower height FLCs.

1.3.3 Manufacturing Risk

At Jaguar Land Rover, the Stamping Engineering department are responsible for the design, development, and delivery of safe and robust stamping processes. Early risk identification and resolution during simulation feasibility studies reduces the likelihood of performing costly remedial work (e.g. design changes, tool re-cutting) on physical toolsets. Whilst FLCs aid design feasibility, there is uncertainty concerning their position and shape on the Forming Limit Diagram (FLD).

The formability of as-received materials is characterised through a series of controlled experiments. Material specimens are deformed along a range of strain paths, with strains measured at the onset of localised necking. When tested according to the standard ISO method, these measurements exhibit scatter which takes the form of a variation in the limit strain. Examples of typical experimental scatter are shown in Figure 3. This variation can be as much as 0.05 (true strain) in the direction of the strain path. The magnitude of this variation, which is significant compared to the mean forming limit in that direction, creates an ambiguity over the level and shape of the material's FLC.

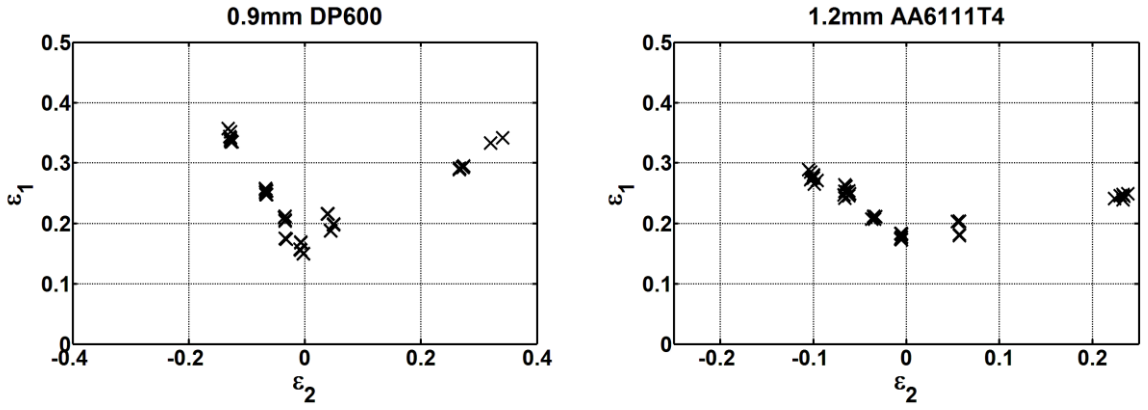

(a) (b)

Figure 3: FLDs showing the typical experimental scatter of limit strains of (a) 0.9mm DP600 and (b) 1.2mm AA6111T4

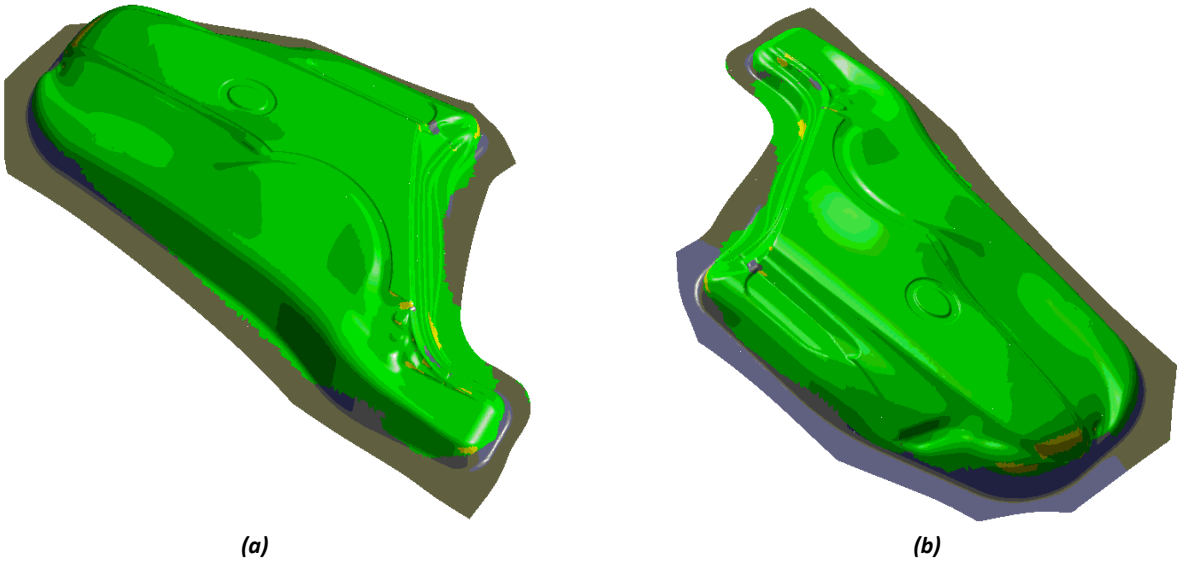

(a) (b)

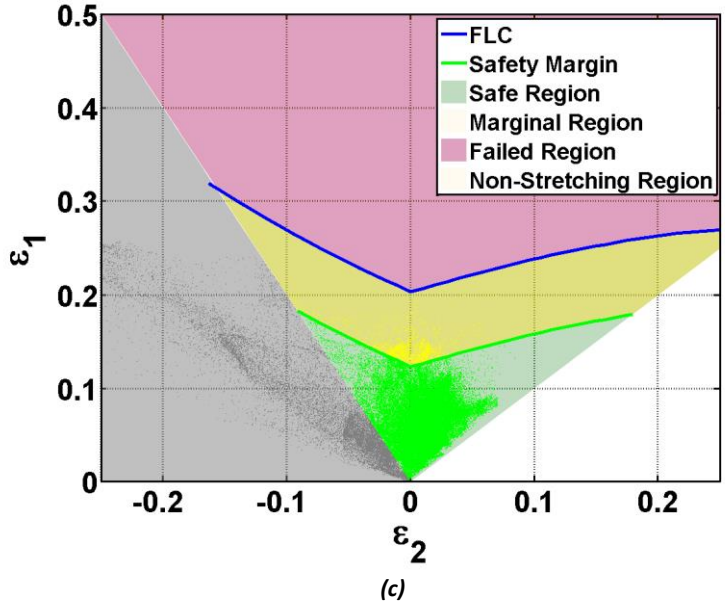

(c)

Figure 4: Example of a rear fender drawn shell viewed from (a) topside, (b) underside, and (c) comparison against the FLC

A further uncertainty forming engineers must contend with is the sensitivity of forming limits to both the mechanical property variation which naturally occurs in sheet metal production, and to the loading conditions imposed by the stamping die. Small changes to mechanical properties, and/or any non-proportional loading conditions that occur in the stamping operation, can substantially impact both the shape and level of the FLC. To overcome the uncertainties associated with defining the FLC and the sensitivity of the FLC to inherent production conditions, a measure of risk mitigation is necessary. A popular technique is to apply a safety margin to the FLC. The safety margin is a curve positioned at a fixed major strain below the FLC. The FLC and safety margin partition the FLD into three regions: 1) safe region – area beneath the safety margin; 2) marginal region – area between the safety margin and the FLC; 3) failed region – area above the FLC. Surface strains which reside in the safe region are considered robust to failure; strains in the marginal region are considered to have a risk of failure; and strains in the failed region are considered to almost certainly cause a defect. Figure 4 shows the FLC and safety margin, together with an overlay of surface strains simulated on a drawn shell.

1.4 MOTIVATION

Reduced formability of lightweight materials, as characterised by the FLC, constrains the level of styling freedom and design flexibility available to part stylists and tool designers. To minimise the restrictions of lightweight materials, it is desirable to maximise the amount of formability utilised without exposing the manufacturing process to unnecessary risk. This requires accurate characterisation of material formability and accurate compensation of risks to formability. The current practice of characterising formability with an FLC and minimising risk through a safety margin is a barrier to safely maximising formability.

The safety margin is intended to mitigate against three risks of forming failure: 1) the risk that the FLC is not reflective of a material's true formability; 2) the risk that intrinsic mechanical property between blanks cause formability variation between panels; and 3) the risk that conditions imposed by the stamping operation itself cause premature failure. The contribution of each risk towards the overall “formability risk” has not been quantified. Summarising these risks in a single safety margin prevents forming engineers from accurately quantifying the risk of failure. This restriction is particularly pertinent to situations where a forming simulation predicts a panel’s surface strains fall inside the marginal region.

If a forming simulation identifies that strains on a stamped panel fall within the marginal region, remedial actions must be agreed by both design and manufacturing engineers. Design engineers are responsible for styling aesthetically attractive panels to enhance vehicle appeal to a broad range of customers. Reducing styling freedom through the application of a safety margin leads to aesthetically less desirable vehicles (reduced market appeal), higher panel count (increased cost of manufacture and assembly) and thicker/heavier material selection (increased vehicle weight). To increase the likelihood of meeting a design brief, styling engineers are more ready to accept surface strains which fall into the marginal region. By contrast, manufacturing engineers are responsible for producing high quality panels using repeatable and reliable production processes. Repeatability and reliability is achieved by reducing the risk of manufacturing defective panels. Manufacturing engineers are therefore less ready to accept surface strains which fall into the marginal region. Conflicts of interest between engineers lead to disputes when determining remedial actions for stamping tools producing panels with surface strains in the marginal zone.

Jaguar Land Rover’s ability to fully and safely utilise the formability of less formable materials is limited until formability is more accurately described, and the risk of failure to a panel is more

precisely quantified. The scatter arising from experimental measurements, and the subsequent characterisation of limit strains by an FLC, are the primary barriers for accurately describing material formability. The sources of limit strain scatter must be identified and addressed. A more precise and objective method of characterising these limit strains must also be developed. Until formability is accurately measured and precisely characterised, the risks to formability arising from mechanical property variation or the stamping operation itself cannot be accurately quantified.

1.5 CONCLUSIONS

- The scatter arising from experimental tests implies there is uncertainty about the accuracy of formability measurement
- There is uncertainty about the precision of the FLC, due to the freedom available to interpret the shape and position of the curve within scattered limit strains
- Formability is known to be sensitive to natural variation in mechanical properties, and to the deformation conditions imposed by industrial stamping operations. The safety margin is a subjective simplification of the risks posed to formability

The aim of this Engineering Doctorate is to understand and characterise the uncertainty in scattered limit strains, and develop a more accurate and precise method for determining and representing formability.

1.6 RESEARCH METHODOLOGY AND INNOVATION REPORT STRUCTURE

1.6.1 Research Methodology

This innovation report is structured to follow the progress of the Engineering Doctorate and the portfolio submissions. The author's Engineering Doctorate portfolio comprises five submissions, in addition to this innovation report. These submissions were written chronologically, in the structure outlined in Figure 5, consistent with the research methodology that was followed.

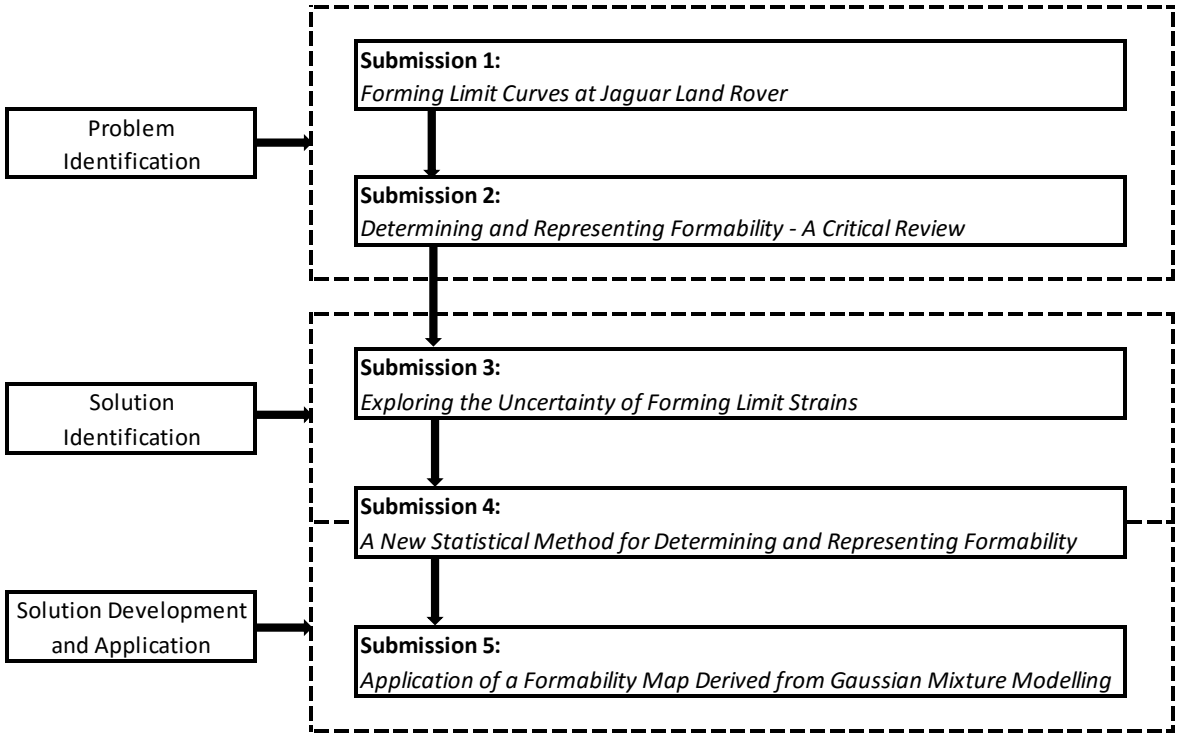

Figure 5: Engineering Doctorate portfolio structure

Firstly, there was a need to identify and understand the problems facing the industrial sponsor. This was completed in two separate reviews. The focus of the first review, documented in Submission 1, was to identify external factors which influence the construction of a modern passenger vehicle. This was completed using publicly available European Union directives; government-issued investigations; and drawing upon the knowledge and experiences of Jaguar Land Rover and Tier 1 material suppliers. The information captured was used to contextualise industrial concerns with current formability assessment techniques, and define the research aim.

The second review, documented in Submission 2, was conducted to examine the current state of the art with respect to sheet metal formability. This was completed using secondary information sources including peer reviewed journals, conference proceedings, books, and the internet. Knowledge gained from the literature was also supplemented by primary experimentation. The main focus of the review was to identify limitations with current measurement techniques that cause ambiguity in formability measurement. As such, the review covers the essential requirements for experimentally measuring and representing formability, and discusses the influence of both the material and the stamping process on forming limits.

Submission 3 documents three investigations that were carried out to verify the inferences made from the literature review, and identify a solution to fulfil the research aim. The aim of the first investigation was to establish the systematic error of a strain measurement instrument. This was achieved by making zero-strain measurements of different shaped specimens using a DIC-system, and analysing the results using an ANOVA. The aim of the second investigation was to confirm whether surface strain behaviour identified in the literature was visible during standardised formability tests. This was achieved by creating a MATLAB tool to visualise strains measured by the DIC instrument independently of the specimen's geometry. The aim of the third investigation was to verify that the scatter typifying measured limit strains is caused by the method used to identify and characterise a localised neck. This was achieved by performing a series of Marciniak tests for a broad range of automotive alloys. Measured strains were analysed with respect to the ISO-standard method as well as a selection of alternative methods identified from the literature.

The primary research of the Engineering Doctorate was carried out in Submission 4 where a solution was developed to fulfil the research aim. A new method for determining and representing formability was developed using a statistical modelling methodology. Exploratory data analysis was used to demonstrate the existence of statistical patterns and trends on the surface of a specimen undergoing a formability test. An innovative parametric model was constructed to quantify this behaviour, and relate statistical behaviours to the physical behaviour of materials. The model was subsequently used to perform the tasks necessary to objectively determine formability, and overcome the limitations of the current method. The utility of the new method was verified by measuring the formability of a broad range of automotive alloys, and benchmarking the results against standardised forming limits. Finally, a complimentary regression model was used to create an objectively positioned, probabilistic forming limit criterion to provide the more precise representation of formability required to fulfil the research aim.

The value of this research was demonstrated in Submission 5 where the new formability criterion was used in a design feasibility study. A forming simulation was assessed against two different limit criteria: the conventional FLC, and the new formability criterion. The conventional safe/marginal/fail assessment made against the FLC was compared to a more precise, probabilistic measure of failure using the new criterion. The results obtained from the two assessments were correlated to the actual panel, and to the defects that arise in production.

1.6.2 Innovation Report Structure

This innovation report has been structured in such a way as to guide the reader through the topic and highlight the most important aspects of measuring and interpreting formability. The report begins with a background section which covers the primary aspects of this field, and then describes the underlying principles of the research methodology and highlights of the research. The main focus of the research is the determination and representation of formability. This report documents the methodical and rigorous research undertaken which has led to the development of an innovative experimental methodology for deriving a forming limit criterion. It describes the key innovations in detail before demonstrating the utility of the new criterion in an industrial formability study. Subsequently, it describes a phenomenological model used to predict features of the new criterion from mechanical properties, and discusses the underlying material structures that must be considered to obtain an accurate prediction. Finally, it summarises the project and discusses area for future work.

Chapter 2 presents the background of the project, including a review of the FLC concept. A critical assessment of the current state-of-the-art techniques for measuring formability is performed. This is accompanied by a review of secondary literature to understand the effects of mechanical properties and stamping conditions on formability. A discussion on how these features impact the assessment of an industrial panel is also provided. This chapter concludes by recognising the key requirements for accurate and precise measurement of a localised neck, and identifies a methodology for developing a new method to overcome the restrictions of the ISO-standard and alternative methods which prohibit this measurement.

Chapter 3 documents the main innovations created in this research. The chronological development of a new holistic statistical methodology for determining and representing formability is described which overcomes the limitations identified with established methods. It starts with a fundamental statistical analysis of strains measured during the course of formability tests. This leads to the discovery of a series of statistical trends common to both aluminium alloys and steels. An appropriate model is selected to quantify these trends, and correlate these trends to the physical behaviour of deformed specimens. The utility of the statistical model is then extended to perform the key stages of formability measurement: the identification of a neck's location; the identification of the onset of localised necking from within a DIC-measured strain history; and the characterisation of the neck itself. The new method is used to measure the formability of a selection of automotive-grade sheet metals, with the results compared to limit strains obtained using the ISO-standard method. The remainder of the chapter describes the application of a regression model to translate experimental measurements into a practical, probabilistic representation of formability, which is benchmarked against the conventional FLC.

Chapter 4 describes the utility of performing a design feasibility assessment using the statistical formability criterion. An industrial panel is considered, selected by the industrial sponsor, which is assessed using two techniques: the conventional FLC technique; and the new criterion developed in this research. It is shown how the additional precision afforded by the new technique provides a more objective measure of the risk of failure for the panel, and in the case considered, cost avoidance for the industrial sponsor. The chapter then highlights the hurdles that need to be overcome in order to gain a complete and accurate measure of the risk of failure for an automotive panel.

Chapter 5 describes the application of a continuum plasticity model to predict the character of surface strains at the forming limits from core mechanical properties and surface characteristics. Predicted strains are compared to the new formability criterion and to the benchmark ISO-measured

limit strains. A discussion is included on the unique microstructures of the analysed materials that are responsible for the character of the DIC measurements, and that should be considered to improve the quality of the predictions.

Chapter 6 provides the final conclusions of the project and elucidates the innovations created and the contributions to knowledge that have been made. Recommendations are also provided for future research work.

2 RESEARCH BACKGROUND

In order to identify the origins of scattered limit strains, a review of the published literature is conducted. The review focusses on four areas:

- Methods of determining formability – Best practice methods for experimentally determining formability are evaluated to identify sources of uncertainty in formability measurement
- Influence of mechanical properties on formability – The impact of mechanical properties on formability is examined to understand likely formability variation between tested specimens
- Techniques for characterising formability – Alternatives to the FLC are sought to more precisely characterise strain behaviour at the forming limit
- Influence of strain path non-linearity on formability – A significant discrepancy between formability characterised in the laboratory and the formability achievable in the press shop arises because of the influence of non-proportional loading. Understanding the impact of strain path changes, caused by non-proportional loading, on formability is helpful to determine the effectiveness of the safety margin in mitigating the risk to formability caused by the stamping operation

2.1 DETERMINING FORMABILITY

Formability is determined through a set of controlled experiments. For consistency and repeatability, a standardised method for determining forming limits in the laboratory is prescribed by **ISO12004-2** (**2008**). Three principal aspects are considered in the standard: 1) the test method used to deform material specimens, 2) the measurement technique used to record deformation, and 3) the measurement of the localised neck. The techniques prescribed by the standard are discussed herein.

2.1.1 Tests for Determining Formability

ISO12004-2 describes two test methods: a method outlined by **Nakazima et al.** (**1971**) and a method outlined by **Marciniak** (**1967**). Figure 6 shows the tooling schematics of the two methods. Both apparatus deform waisted blanks over a 100mm diameter punch with an open cylindrical die. Adjusting the waists of the test specimens gives rise to different proportional loading conditions, resulting in different strain paths. The primary difference between the methods is the hemispherical punch face prescribed by the Nakazima method and the flat-bottomed punch face prescribed by the Marciniak method.

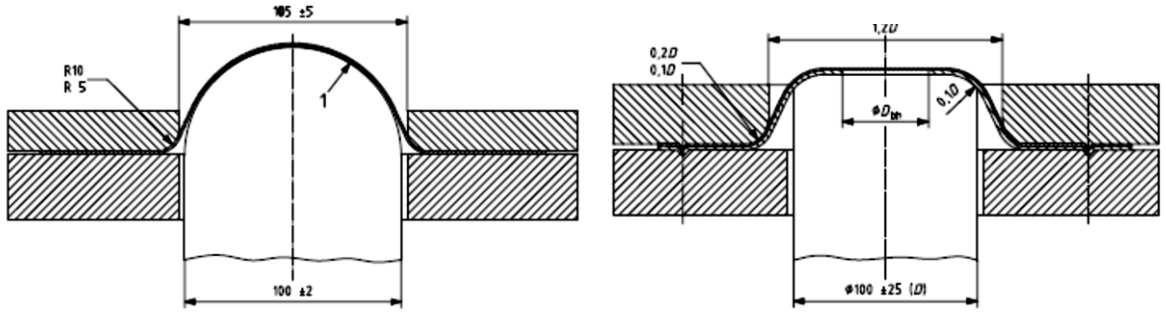

(a) *(b)*

Figure 6: Schematics of tools used in (a) the Nakazima method, and (b) the Marciniak method

During testing, the Nakazima punch contacts directly with the test specimen. To reduce the influence of friction between the punch and specimen, a tribological structure is placed at the

interface (labelled **1** in Figure 6a). Friction is negated between the Marciniak punch and the test specimen through the inclusion of a sacrificial carrier blank. Carrier blanks are sacrificial specimens manufactured to the same geometry as the test specimen, with the inclusion of a 32-34mm diameter hole machined at the centre. To avoid premature failure, carrier blanks are made from material more ductile than the test material. Unlike the Nakazima test where the tooling geometry causes out-of-plane straining, inclusion of the carrier blank in the Marciniak test promotes in-plane straining in the area of the specimen located above the hole.

Both punch-stretching tests described in ISO12004-2 use dedicated tooling and apparatus. Extensive availability of tensile test apparatus has motivated researchers to develop alternative test methods for determining formability. **Priadi et al.** (**1992**) designed five 300mm length rectangular specimens of variable widths and notch sizes capable of replicating strain paths between uniaxial tension and plane strain. Limit strains measured for a mild steel closely resembled those obtained by the conventional Nakazima method. Independently, **Holmberg et al.** (**2004**) designed notched specimens of different lengths, widths, and notch sizes. Limit strains obtained for a mild steel and a high strength steel were lower than those obtained by the Nakazima method.

The prevalence of hydraulic bulge testing equipment has led researchers to adapt existing apparatus to characterise formability. **Lazarescu et al.** (**2012**) manufactured a toolset where the bulging aperture is elliptical, rather than circular. Varying the ellipticity ratio of the aperture between 1 and 0.4 invoked strain paths ranging from equibiaxial tension to (close to) plane strain. **Banabic et al.** (**2013**) kept a regular circular aperture, instead designing a series of double-skinned test specimens. The outer test specimen has two off-centre holes, with the inner test specimen manufactured from material at least as ductile as the test piece. The position and ellipticity of the holes dictated the strain path achieved in the centre of the outer specimen. Limit strains of AA6111T4 measured using the method of **Banabic et al.** (**2013**) were consistently lower than those obtained by the standardised Nakazima test.

The inability of the identified tensile test adaptations to generate biaxial straining conditions limits their capability to conduct conclusive formability studies. By the same rationale, the inability of the method prescribed by **Lazarescu et al.** (**2012**) to generate uniaxial straining conditions also restricts its application. For the purpose of formability characterisation, the Nakazima and Marciniak methods offer the most favourable conditions.

According to **Abspoel et al.** (**2011**) the Nakazima method is the more widely adopted. However, practical experience and published research raises concerns that the Nakazima punch geometry causes deformation conditions which prohibit accurate formability characterisation.

The first concern surrounds the impact of friction. Frictional interaction between the Nakazima punch and test specimen impacts the distribution of strains on the test specimen, initiating off-apex failure or causing deviation from the designed-for strain path. Despite the inclusion of a tribological stack between the punch and the specimen, practical experience has shown that a completely frictionless situation is rarely achieved. Surface strain distributions of samples deformed with a Nakazima punch, such as those displayed in Figure 7, are regularly characterised by a double strain concentration around the apex of the punch. Occurrence of such a distribution during localised necking introduces an uncertainty when locating and measuring the localised neck.

The second concern surrounds the stress state invoked by the hemispherical punch. Under planar stress conditions, such as those induced in a simple tensile test, through-thickness strains in the material are uniform. Once a limiting criterion such as necking or fracture occurs, it is commonly

assumed that the failure occurs uniformly through the material thickness, enabling the failure mode to be characterised from both faces of the specimen. However, non-planar stress states – such as those caused by the Nakazima punch – cause out-of-plane straining. The resulting through-thickness strain gradient affects the manifestation of the localised neck. **Morales et al.** (**2009**) observed that initiation of a neck on the more-deformed outer face does not induce an overall instability. Morales concluded that as a result of out-of-plane straining, localised necking is suppressed by less-deformed material in the bulk of the sheet. **Tharrett & Stoughton** (**2003**) proposed that to characterise the formability of materials subjected to non-planar stress states, it is necessary to measure to onset of localised necking at the inner face. Consequently, formability characterisation is limited when strain measurements are constrained to the outer specimen face.

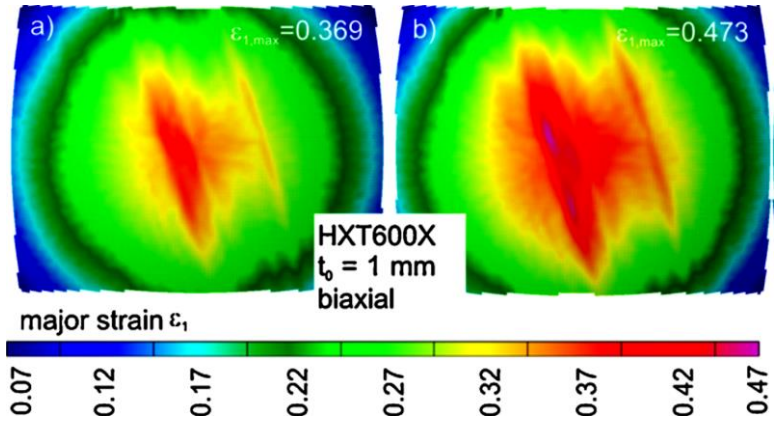

Figure 7: A "double peak" in the major strain distribution of a HXT600X specimen deformed by Merklein et al. **(**2010**)** ***using Nakazima tooling***

The final concern surrounds the ability of the Nakazima method to maintain proportional deformation. Initial contact between punch and test specimen (regardless of specimen geometry) results in biaxial straining. Only when punch and specimen are in full contact is the designed-for strain path realised. As a consequence of biaxial pre-straining, FLCs derived using Nakazima tests are characterised by a positive minor strain offset, as demonstrated in Figure 8.

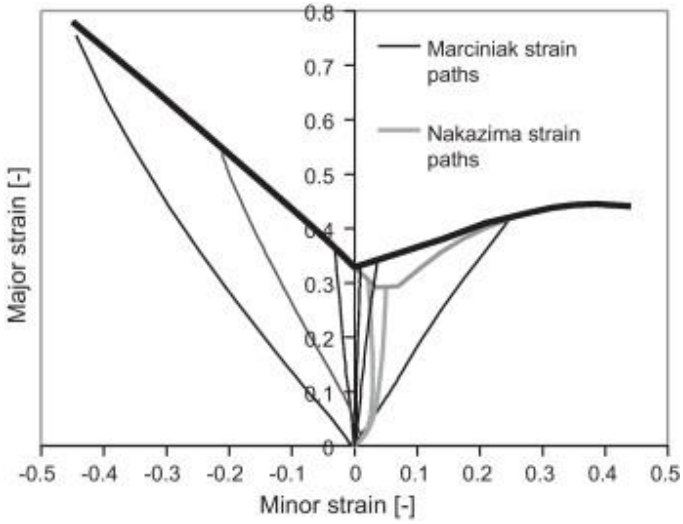

Figure 8: FLCs demonstrating the strain paths generated by Marciniak and Nakazima tooling (Abspoel et al. **(**2013**)***

Atzema et al. (**2002**) suggest that modelling the impact of biaxial pre-strain is necessary to "correct" FLCs obtained by Nakazima tests. **Leppin et al.** (**2008**) and **Abspoel et al.** (**2011**) tested samples of

aluminium and steel respectively, using Nakazima and Marciniak tooling. Comparing the strain paths measured during the two tests demonstrates that biaxial pre-strain not only shifts FLC_0 to the right, but also lowers the height of FLC_0. Results also demonstrate the magnitude of pre-strain is a function of specimen width. By contrast, **Abspoel et al.** (**2011**) and **Leppin et al.** (**2008**) demonstrated that proportional deformation is preserved throughout Marciniak tests. Consequently, FLC_0s of Marciniak FLCs are aligned to the y-axis and no "correction" is required.

In addition to preserving proportional deformation, the previous concerns with the Nakazima test do not affect specimens deformed by the Marciniak method. Firstly, inclusion of a carrier blank prohibits contact between the Marciniak punch and test specimens, entailing no frictional interaction between the two mediums and eliminating the non-uniform strain distribution that characterise the surfaces of Nakazima specimens. Secondly, the flat bottom of the Marciniak punch, combined with the carrier blank, ensures specimens are subject to planar stresses only. Specifically, planar stresses are realised in the area of the test specimen located above the carrier blank hole (known furthermore as the Zone of Evaluation). As a result, the impact of curvature or bending on forming limits measured by the Marciniak method is negligible.

2.1.2 Surface Strain Measurement

Surface strain measurement of sheet metals involves analysing a surface grid pattern and making a comparison between the pattern configuration before and after deformation. An assumption is made that each element in the grid deforms under planar conditions, with the third principal strain in the direction normal to the sheet surface. Assuming the material remains incompressible; an element's principal strains are calculated directly from the distortion of the pattern. The geometrical changes of individual grid elements illustrate the distribution of both the magnitude and direction of strains over the sheet.

Precise and accurate strain measurements are required to measure the localised neck at the forming limit. Within ISO12004-2 two strain measurement techniques are described - an offline technique and an online technique. Offline techniques make strain measurements on specimens *ex-situ*, thereby constraining strain analysis to failed specimens, or specimens retrieved from an interrupted forming operation. Online techniques are capable of measuring the surface strains of specimens *in-situ*, enabling the entire strain history of a specimen to be measured.

Early research into sheet metal formability, including the pioneering researches of **Keeler** (**1961**) and **Goodwin** (**1968**), used the offline technique to measure surface strains. Both researchers etched a ≈5mm diameter circular grid on un-deformed specimens, and measured the grid distortion using Mylar tape. This technique is limited by the use of large diameter grids which can overlook certain characteristics of a localised neck. For example, the neighbourhood of a localised neck is often characterised by a sharp strain gradient, which can be smoothed within the boundary of a large grid. This reduces the ability to locate, and subsequently measure, the localised neck. **Banabic** (**2010**) cites **Grumbach & Sanz** (**1972**) who studied the influence of the grid diameter on forming strains. Having analysed circle diameters between 0.5mm and 5mm, **Grumbach & Sanz** (**1972**) concluded the circle diameter has a strong influence on strains measured in the direction of the strain gradient.

Improved measurement resolution is achievable using smaller diameter circles. For example, **Tadros & Mellor** (**1978**) used 1.1mm diameter circles spaced 1.6mm apart in their investigation into in-plane formability. However, **Sowerby et al.** (**1982**) recognised a difficulty in visually distinguishing between the major and minor strains of small circles deformed below 5% engineering strain. To overcome this difficulty, **Sowerby et al.** (**1982**) proposed a quadrilateral grid pattern, where strains are calculated from the transformation of the spatial co-ordinates of the grid. Under proportional

deformation, Sowerby et al. demonstrated that adopting a quadrilateral grid pattern overcomes the resolution limitation of circular grids, and provides total coverage of test specimens. ISO12004-2 prescribes a maximum grid size of 2.5x material thickness to ensure the development of a neck is adequately captured, with grid sizes between 1mm and 2mm typically used for formability characterisation.

A critical limitation of offline grid analysis is that only the final strain state is measured. The route by which the final strain state was reached cannot be obtained. Plasticity theory dictates that strain increments can only be integrated under proportional loading conditions. The Nakazima test and the majority of stamping operations are known to induce non-proportional loading. Therefore, the examination of formability using offline measurements is limited.

Continuous recording provided by online measurement techniques generates high quantity, high resolution images. These images enable strain increments to be calculated over the course of the test. **Vacher et al.** (**1999**) used a single camera to track in-plane deformation of a Marciniak sample. The strain measurement history was interrogated to identify the localised neck, and construct an FLC. A further development in the research of **Vacher et al.** (**1999**) was the use of a stochastic surface pattern as opposed to a regular grid. Imaging software was used to discretise the stochastic pattern into a quadrilateral grid, with each grid element having unique grey-level values. Cross-correlation was used to track the motion and distortion of the grid by matching each element's grey-levels between successive images. Advantages of using a stochastic pattern over a regular grid include the simple method for generating and applying the pattern, and an achievable sub-1mm resolution.

Continuous recording using a single camera is only able to capture to distortion of specimens subject to in-plane deformation and no rigid-body motion. To overcome this limitation, **Geiger & Merklein** (**2003**) used two CCD cameras to simultaneously record deformation of a specimen stretched over a Nakazima punch. A stochastic pattern was applied to the specimen, and the method of **Vacher et al.** (**1999**) was used to discretise the pattern into a grid of 0.9mm x 0.9mm elements. An FLC of H360LA was subsequently drawn from the strain measurements.

In recent years, automated optical strain measurement has become almost ubiquitous in formability research. Commercial systems include ARAMIS by **GOM mbH** (**2012**), AutoGrid by **ViALUX GmbH** (**2012**), and Q400 by **Dantec** (**2014**). The ARAMIS system is available within WMG for use in this research project. A comprehensive measurement-error investigation of the instrument was conducted as part of this research, where the influence of both internal and external factors on measurement accuracy was calculated. Results showed that the measurement error of the ARAMIS system is negligible compared to the magnitude of likely forming limit strains, and not significantly influenced by the identified internal and external factors. For further information the reader is directed towards Submission 3 where this investigation is reported in full.

2.1.3 Determining Formability

Historical methods of determining formability have been based on a visual inspection of a fractured specimen. **Keeler & Backofen** (**1963**) and **Goodwin** (**1968**) manually classified the elements of a circular grid on a fractured specimen as "safe" or "failed" depending on the circles' proximity to fracture. When both sets of strain measurements were plotted on an FLD, the limit strain was interpreted as the boundary between the two states. **Hecker** (**1972**) extended this principle by adopting three classifications: "fractured", "visibly necked", and "neither fractured nor visibly necked". Like **Keeler & Backofen** (**1963**) and **Goodwin** (**1968**), **Hecker** (**1972**) interpreted the forming limit as the border between the circles when plotted on an FLD. Alternatively, **Veerman** (**1971**) drew

a locus on the specimen three circles in width adjacent to the fracture. The limit strain was interpreted as the average strain of circles within the locus. Each of these methods requires a manual interpretation of strain measurements. For a high-density grid pattern, manual assessment is both time consuming and subjective.

Later determination methods focus upon estimating strain behaviour at the onset of necking. **Bragard et al.** (**1972**) proposed a method whereby a cross-sectional profile is drawn through a fractured specimen, perpendicular to fracture. Strains on the profile are subjectively classified as being either inside or outside the failure area. To estimate the strain profile at the onset of localised necking, a parabolic regression curve is fitted to strains judged to be outside the failure area. The limit strain is taken as the maximum point on the regression curve.

The quality of the regression curve fit used by **Bragard et al.** (**1972**) is sensitive to both the resolution of the strain grid and the classification of strains along the profile. To overcome this sensitivity, an improved method was proposed by **D'Hayer & Bragard** (**1975**). Known as the "double-profile" method, a second strain profile is drawn on the specimens at the onset of fracture. Overlaying strain profiles obtained at the onset of, and at, fracture enables strain measurements common to both profiles to be identified. Performing regression on these common measurements removes the subjectivity with the manual strain classification required by the method of **Bragard et al.** (**1972**).

Strain profile analysis is advocated in ISO12004-2 for limit strain determination. A single strain profile is extracted from either a fractured sample (if only offline measurement is available) or at the onset of fracture (if online measurement is available). The strain profile is drawn manually, as per the methods of **Bragard et al.** (**1972**) and **D'Hayer & Bragard** (**1975**). The profile is then differentiated to magnify the strain gradient in the neighbourhood of the neck, enabling the neck to be more objectively located within the profile. The slope of the differentiated profile is used to identify a "forming window" - strains which are not used during subsequent regression. An inverse second-order polynomial is fitted to ten measurements either side of the forming window to estimate the strain profile at the onset of localised necking. The limit strain is taken from the peak of the polynomial curve. **Hotz & Timm** (**2008**) report that limit strains obtained by this method are repeatable between laboratories.

Despite enabling limit strains to be repeatedly calculated, the standardised "position-dependent" method of limit strain determination has limitations. Firstly, it is assumed that the strain profile at the onset of localised necking conforms to a second-order polynomial, as shown in Figure 9a. Several scenarios may occur where this assumption is invalid. For example, **Zhang & Wang** (**2012**) observed multiple competing necks during the deformation of DP600. This phenomenon was also observed during biaxial deformation of a DP600 specimen (Figure 8 in Submission 2). In these examples, neither the strain profile at fracture nor at the onset of fracture conforms to a second-order polynomial. Likewise, the strain distribution of a Nakazima specimen is regularly characterised by a double strain concentration (Figure 7), as described in Section 2.1.1. The strain profile of such a specimen is also characterised by a twin-peaked strain profile (shown in Figure 9b) signifying non-conformance to the assumptions made in ISO12004-2.

Secondly, limit strains are estimated from measurements made on a failed (either post-localised necking or post-fractured) specimen. Strains characterising the onset of localised necking cannot be directly measured if analysis is constrained to a failed specimen. To overcome this limitation, several "time-dependent" methods have been proposed. These methods utilise strains measured by digital image correlation (DIC) to determine the onset of localised necking from the deformation history of a specimen.

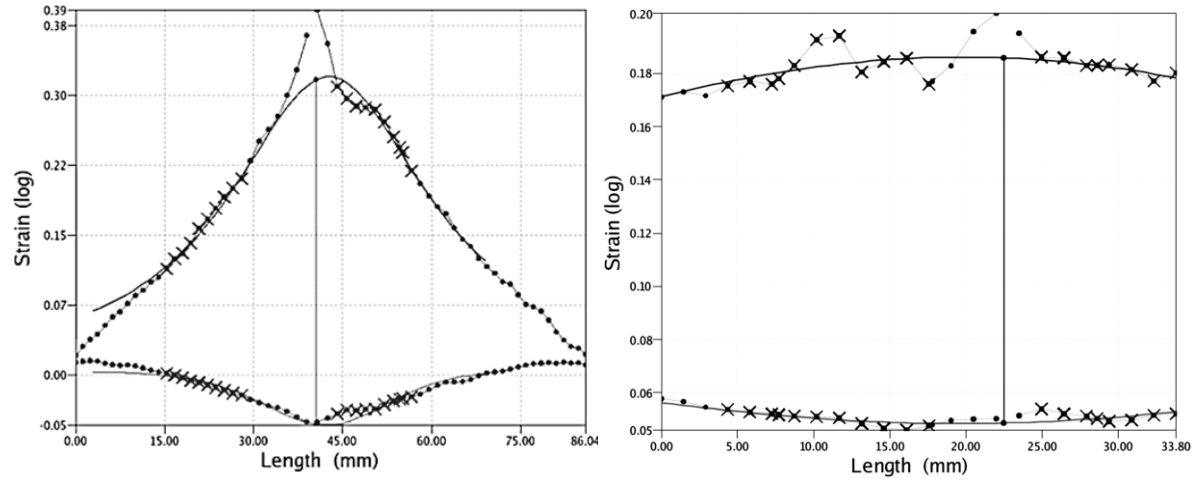

(a) *(b)*

Figure 9: Major strain profiles (upper outline in (a) and (b)) and minor strain profiles (lower outline in (a) and (b)) drawn across two Nakazima specimens, where (a) demonstrates a specimen conforming closely to a second-order polynomial, and (b) a specimen poorly conforming to a second-order polynomial

Vacher et al. (**1999**) observed that localised necking in mild steel is a gradual process, and that the onset of localised necking may occur early in a formability test. Through visual inspection of successive DIC measurements, Vacher et al. observed the temporal and spatial characteristics of the measured strain and strain rate fields. According to Vacher et al., the onset of necking occurs when the strain rate becomes concentrated in a small area of the strain field, and the strain rate of the remaining material tends to zero. The limit strain is then obtained from the preceding DIC measurement.

The approach of **Vacher et al.** (**1999**) was extended by **Volk** (**2006**) who introduced a more objective method of determining the onset of localised necking. **Volk** (**2006**) deformed a Nakazima specimen and measured deformation using a DIC system. Each DIC measurement was then assessed against two criteria. Firstly, elements within the measurement grid were categorised as those experiencing increasing or decreasing strain rate. Secondly, the magnitude of the strain rate changes were analysed over the course of the test. The onset of localised necking was determined from a sudden increase in the number of elements experiencing severe increases in strain rate (inside the neck) and a corresponding number of elements experiencing a reduction in strain rate (outside the neck). **Eberle et al.** (**2008**) extended this principle by including an empirical frequency diagram to track the development of the distribution of strain rates, and more accurately determine the onset of localised necking.

More recently proposed "time-dependent" methods use time series analysis to determine the onset of localised necking. These methods track strains (or strain rates) in a small area of the localised neck, and use the evolving characteristics of the area to detect the onset of localised necking. **Merklein et al.** (**2010**) constrained their analysis to a 2mm diameter circle in the centre of the localised neck. The mean major strain acceleration ($\ddot{\varepsilon}_1$) within the circle was recorded and plotted for each DIC measurement. **Volk & Hora** (**2010**) constrained their analysis to elements of the measurement grid that fall within 50% of the maximum measured thinning rate at the onset of fracture. The mean major thinning rate ($\dot{\varepsilon}_3$) within the area was recorded and plotted for each DIC measurement. Figure 10 demonstrates that both methods result in a time series displaying a sharp inflection point at the onset of localised necking. The inflection point is visually identifiable, and can be objectively located using linear regression. **Merklein et al.** (**2010**) demonstrated that limit strains

calculated using their method are comparable to those obtained using the standardised "position-dependent" method for HX260 and AA6016.

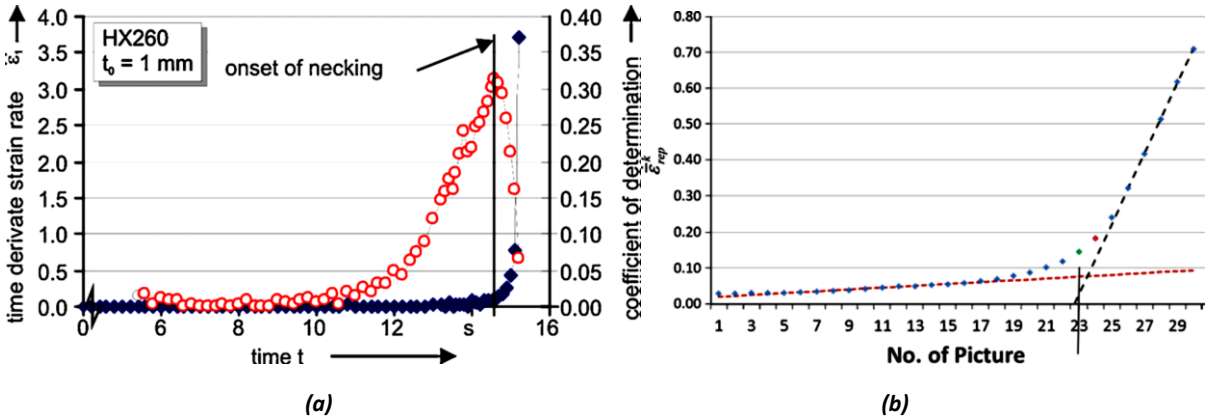

(a) *(b)*

Figure 10: Time series as calculated using the methods of (a) Merklein et al. **(**2010**)*, and (b)*** Volk & Hora **(**2010**)**

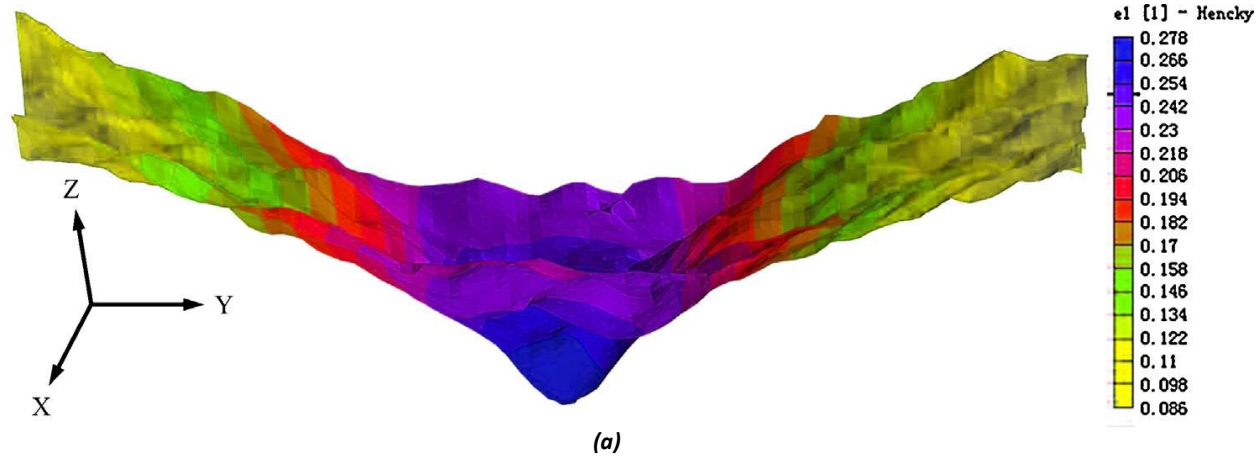

(a)

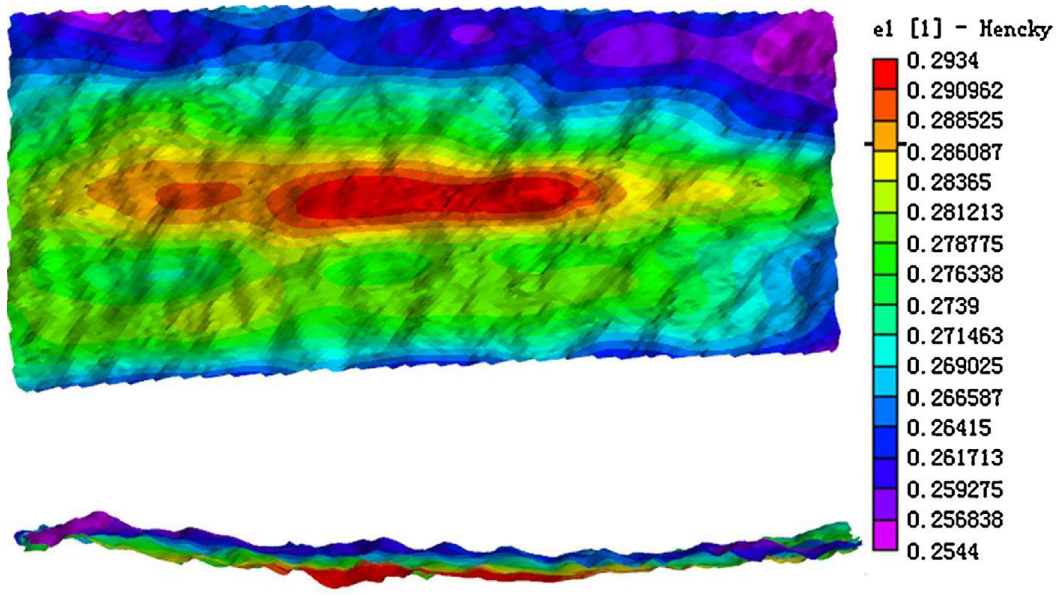

(b)

Figure 11: Strain topographies of an AA5XXX alloy measured by Wang et al. **(**2014**) *using Digital Image Correlation, where (a) demonstrates the major strain topology of a tensile sample at the onset of fracture, and (b) a Marciniak specimen at the onset of localised necking***

An alternative "time-dependent" method was proposed by **Wang et al.** (**2014**) who determined the onset of localised necking from changes to the material's thickness. Wang used DIC to indirectly measure strains in the thickness direction, and then construct a visualisation showing the strain topography independently of the specimen's geometry. Examples of these topographical visualisations obtained are shown in Figure 11 for a tensile specimen and a Marciniak specimen. Wang et al. characterised the topographies of successive DIC measurements by changes to the differences in surface heights. The onset of localized necking is identified by the limit of stable flow of the surface height difference.

"Time-dependent" methods demonstrate that the onset of localised necking is identifiable from DIC-measured strains. This enables strains at the forming limit to be directly measured, rather than estimated via the standardised "position-dependent" method. However, the identified methods do not include provision for objectively defining the size and location of the neck itself. The "time-dependent" methods constrain measurement to a small region of the DIC measurement, such as a 2mm circle (as used by **Merklein et al.** (**2010**)) or strains on a cross section (as used by **Wang et al.** (**2014**)). Without an accurate definition of the neck's size and location, it cannot be measured or characterised. It is likely that this limitation contributes towards the uncertainty in formability measurement.

A further complication is identified when closely examining the strain topographies constructed by **Wang et al.** (**2014**). Figure 11 shows that by viewing strain topography independently of the specimen's geometry, spatial strain characteristics are exposed. A curious feature of Figure 11 is that strains do not vary smoothly, as is generally expected. Instead, a "high frequency" spatial variation in strain is seen to be overlaid above the strain variation associated with the development of the neck. **Wang et al.** (**2014**) did not explore this characteristic but in this work, the high frequency variation is shown to be significant compared to the measurement error (calculated in Submission 3). Therefore, macroscopic strain heterogeneity might be considered an inherent outcome of plastic deformation. Heterogeneous behaviour causes additional complexity in defining and describing the localised neck, and its effect on forming limit uncertainty is explored more closely in this work.

2.2 Influence of Mechanical Properties on Formability

Whilst the experimental technique used to characterise formability contributes towards scattered forming limits, variation in mechanical properties between test specimens is also a contributing factor. A review of the published literature suggests that anisotropy, strain hardening, and strain rate hardening are properties which significantly impact formability. Each of these properties is discussed herein. Following the examination of the DIC-measured strain topographies in the previous section, underlying material properties which might contribute towards surface strain heterogeneity are also evaluated.

2.2.1 Anisotropy

Cold rolling used to manufacture sheet metals forces grains to develop a preferred orientation, visually demonstrated as a surface texture. Directionality (anisotropy) resulting from sheet manufacture and crystallographic structure causes differences in mechanical properties with respect to sheet orientation. Anisotropy is often characterized by tensile tests performed on specimens machined at different sheet orientations (usually 0°, 45°, and 90°). Sheet anisotropy can be characterized in terms of planar anisotropy (ΔR) and normal anisotropy ($\overline{R}$):

$$\Delta R = \frac{R_0 + R_{90} - 2R_{45}}{2} \qquad \textit{Eq. 1}$$

$$\overline{R} = \frac{R_0 + R_{90} + 2R_{45}}{4} \qquad \textit{Eq. 2}$$

If $\Delta R > 1$ the orientation of the sheet becomes significant to drawing processes. In a cupping test, where blank edges are not fully constrained, earing is seen along the blank edge once a cup is fully drawn. The depth of earing is proportional to ΔR. High values of $\overline{R}$ show that under tensile loading the width strain is greater than the thinning strain - implying the material has an inherent ability to suppress thinning. An ability to withstand thinning is desirable to delay the initiation of a diffuse neck. In drawing operations, high $\overline{R}$ indicates an ability to be drawn to greater depths, as characterised by the Limiting Draw Ratio (LDR). **Marciniak et al.** (**2002**) noted that for shallow drawn panels, high $\overline{R}$ values reduce the development of wrinkling. Whilst the impact of $\overline{R}$ on deep drawing is established, a relationship between $\overline{R}$ and formability is less clearly defined. For example, **Raghavan** (**1995**) performed Marciniak tests on a mild steel and an interstitial-free steel. Both materials have similar strain hardening behaviours (similar strain hardening exponents), but different $\overline{R}$ values. FLCs measured by **Raghavan** (**1995**) for both materials are closely aligned. Consequently, Raghavan concluded that $\overline{R}$ has negligible impact on forming limits.

Experimentally determining the impact of a single mechanical property on formability is difficult, since there are almost impassable barriers to modifying a single property in isolation. Furthermore, **Ghosh** (**1977**) has shown that anisotropy values vary during plastic straining. Consequently, direct experimental relationships between anisotropy values and formability are elusive. The impact of anisotropy on formability is better demonstrated through numerical methods. Numerical simulations of metal forming use continuum plasticity models to describe material flow under various loading conditions. Models include those governing the stress states at yield (yield curve), models governing the interaction between applied stress states and plastic strain increments (flow rule), and a hardening rule governing the evolution of the yield locus with plastic strain. Yield curve profiles are directly controlled by anisotropy values. Therefore, the influence of anisotropy on formability can be analysed from changes to the yield curve.

Marciniak & Kuczyński (**1967**) recognised that to induce a localised neck in a stretching operation, an initial biaxial strain path must change to plane strain. A material's ability to transition between the two strain paths is dictated by the shape of the yield curve. **Barlat** (**1987**) observed that decreasing the sharpness of the yield locus in the equibiaxial region promotes higher limit strains. To quantify the sharpness of the yield curve, the parameter *P* (shown in Figure 12a) was introduced as the ratio of major yield stress in plane strain to the yield stress in equibiaxial strain ($P = \sigma_p/\sigma_b$). Both Barlat and **Lian et al.** (**1989**) demonstrated that formability in biaxial tension increases with increasing *P*. A similar parameter was proposed by **Friedman & Pan** (**2000**). Instead of describing the ratio of equibiaxial tension and plane strain yield stresses, Friedman and Pan describe the angle between any initial strain path and plane strain. The angular parameter θ (shown in Figure 12b) is unique to the initial strain path, and describes the change in deformation the material must undergo before reaching plane strain. Like the parameter *P*, increasing values of θ suggest an increase in formability.

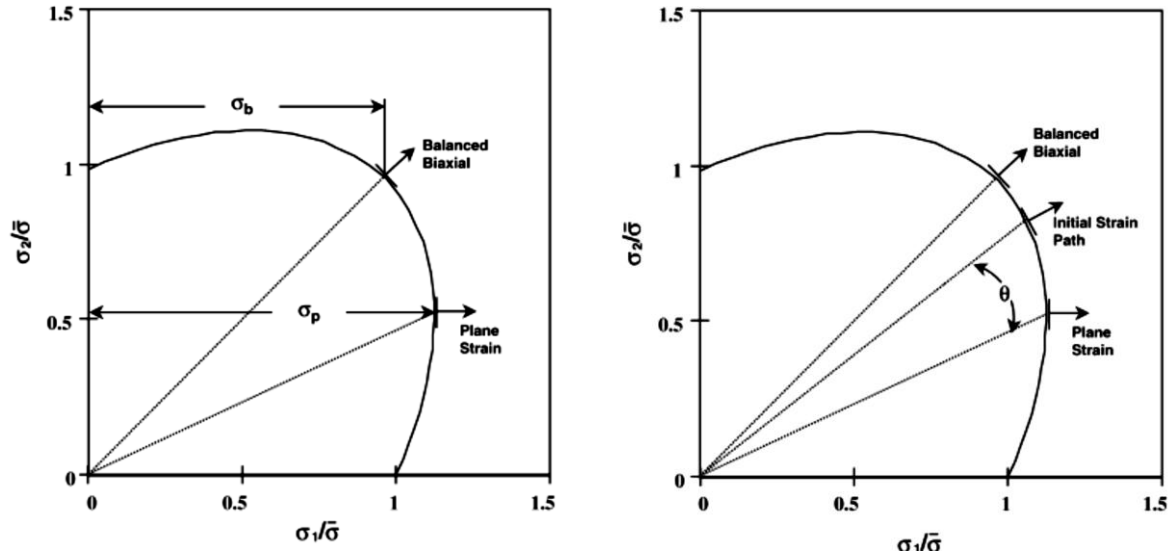

Figure 12: Graphical representations of (a) Barlat's parameter* P *(σ_p/σ_b) and (b) Friedman's parameter* θ *(angular difference between the initial strain path and plane strain) taken from Barlat **(**1987**) *and*** Friedman & Pan **(**2000**)**

The impact of alterations to constitutive models on formability is directly demonstrable through a numerical model. The widely adopted rigid-plastic model of **Marciniak & Kuczyński** (**1967**), herein referred to as the M-K model, is based on observations that a localised neck initiates from an existing structural or geometrical defect. A hypothetical specimen is proposed in the M-K model, where a band of reduced cross-section spanning the width of the specimen represents the inherent imperfection. Applied stresses result in heterogeneous deformation. Geometrical constraints cause the imperfection to deform at a higher rate than the bulk, with the width constraint altering the imperfection's strain path with increasing deformation. Instability occurs when the ratio of strains inside and outside the imperfection crosses a threshold value. Strains at the critical state correspond to the onset of instability, identifiable as forming limit strains. Predicting instabilities arising from different stress states enables an FLC to be calculated. The accuracy of the predicted FLC is sensitive to both the constitutive models and the severity of the initial imperfection. Sensitivity of formability to anisotropy can therefore be predicted through modifications to the yield curve.

In **Marciniak & Kuczyński's** (**1967**) original proposal, **Hill's** (**1948**) criterion was used with normal anisotropy ($\overline{R}$). **Painter & Pearce** (**1974**) demonstrated that the predicted FLCs underestimate formability in plane strain and overestimate formability in biaxial tension. Painter & Pearce also demonstrated that the predicted biaxial forming limits were highly sensitive to normal anisotropy, with increasing $\overline{R}$ reducing the height of the FLC. **Sowerby & Duncan** (**1971**) claim that biaxial forming limit sensitivity is due to the impact of $\overline{R}$ on the first quadrant of Hill's 1948 yield curve. Figure 13a demonstrates that increasing $\overline{R}$ causes the yield locus to elongate in the equibiaxial stress direction. This causes the curvature of the yield locus to sharpen in the equibiaxial region, thereby decreasing Barlat's *P* parameter and Friedman's θ parameter. A revised model by **Marciniak et al.** (**1973**) used Hill's 1948 criterion with orthotropic anisotropy. FLCs predicted for of steel, copper, and brass correlated more closely to experimental measurements, although predicted FLCs of aluminium were less accurate. Biaxial limit strains were still shown to be sensitive to anisotropy, since the curvature of the yield locus sharpens with increasing R_{90}, as shown in Figure 13b.

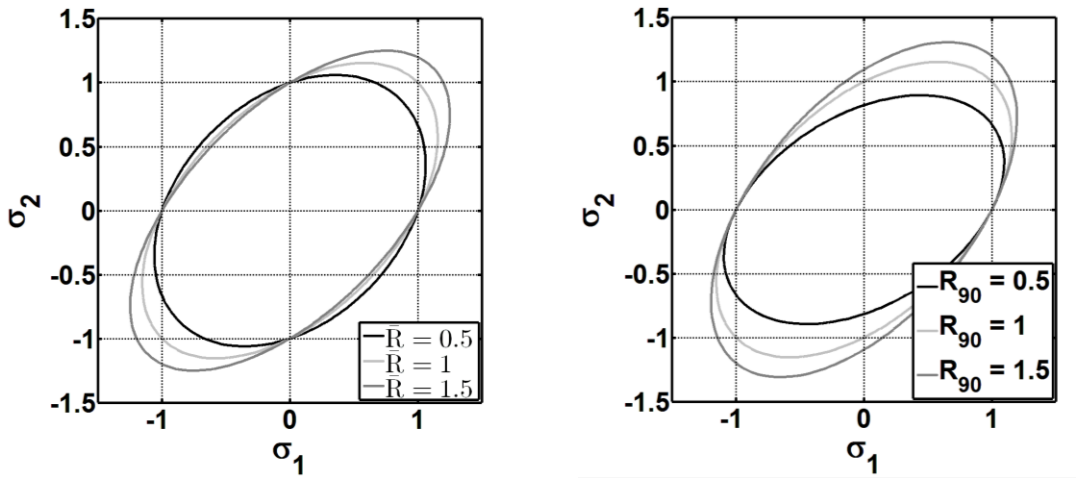

(a) *(b)*

Figure 13: Demonstrating the effect of anisotropy on Hill's 1948 yield curve. (a) Variable $\overline{R}$ assuming normal anisotropy, (b) Variable R_{90} assuming planar anisotropy

Anisotropic characteristics of materials exhibiting $R < 1$ (such as aluminium) are poorly reflected by Hill's 1948 criterion. **Pearce** (**1970**) and **Woodthorpe & Pearce** (**1970**) noticed that when using Hill's 1948 formulation to describe these materials, the yield curve lies within the isotropic Von Mises yield curve. Experimental evidence in these researches demonstrates that despite $R < 1$, biaxial yield stresses lie outside the Von Mises curve. Described (perhaps unsuitably) as "anomalous" behaviour by **Woodthorpe & Pearce** (**1970**), much effort has been expended on developing appropriate yield curves for different materials.

Hill (**1979**) developed an alternative yield curve to describe aluminium alloys. This formulation was integrated into the M-K model by **Parmar & Mellor** (**1978**) who observed less biaxial forming limit discrepancy for materials with $R < 1$. Independently, **Hosford** (**1979**) developed a yield criterion (essentially a mathematical derivative of **Hill's (1979)** criterion) applicable to a range of materials. The distinguishing feature of Hosford's criterion is consideration of crystalline structure. Yield curve accuracy is improved by varying the function's exponents depending on whether a body centre cubic (BCC) (exponent $M = 6$) or face centre cubic (FCC) material (exponent $M = 8$) is modelled. **Graf & Hosford** (**1990**) integrated Hosford's criterion into the M-K model and observed that formability was over-estimated in biaxial tension, but to a lesser extent than forming limits predicted using Hill's 1948 criterion.

The FLC is based on the assumption that formability is isotropic within the plane of the sheet. Consequently, the use of principal strains to describe formability is widespread. For computational convenience, a common attitude in M-K modelling is to align principal stress axis with the orthotropic axis. However, the existence of anisotropic formability is appreciated by several authors. **Barata da Rocha et al.** (**1985**) used an M-K model to compare limit strains predicted when the major strain direction is aligned to the longitudinal and transverse directions respectively. Discrepancies between the forming limits of the two orientations demonstrated the uncertainty caused by using principal strains alone to describe formability. Instead of using a single FLC in principal strain space, **Barata da Rocha et al.** (**1985**) characterised formability by two conjoined FLCs in orthotropic strain space. **Stoughton & Yoon** (**2005**) also considered anisotropic formability, and predicted FLCs for a hypothetical material with the major strain direction aligned to sheet orientations between 0° and

90° at 15° increments. Their results showed that FLCs are unique to the orientation of deformation, with FLC_0 varying up to 0.05 (true major strain) between orientations.

2.2.2 Strain and Strain Rate Hardening

Plastic deformation is the consequence of ductile materials adapting their microstructure to applied stresses. Applied stresses (above the yield stress) result in dislocation movement, where movement is dictated by dislocation density, crystalline structure, grain size and orientation. When dislocation movement is curtailed by e.g. a grain boundary or dislocation entanglement; further dislocation within the containing grain in only achievable at increased stress. At the macroscopic level, increased strength enables materials to retain structural integrity in spite of reduced cross-sectional area. Structural integrity is preserved provided the increased strength obtained through strain hardening is greater than the weakening caused by reduced cross-sectional area. Stressing beyond the limit of strain hardening results in a non-uniform strain field, where deformation becomes concentrated in an increasingly small area - referred to in this work as a diffuse neck. Therefore, materials' strain hardening capability is directly related to formability.

Strain hardening of forming grade mild steels is well approximated by **Holloman's** (**1945**) power law (Eq. 3). The strain hardening exponent *n* offers a single parameter with which to quantify the influence of the rate of strain hardening ($\delta\bar{\sigma}/\delta\bar{\varepsilon}$) on the development of a diffuse neck. Steels with high *n*-values exhibit an increased rate of hardening, thereby delaying the onset of diffuse necking. However, Holloman's equation does not characterise all materials. **Kleemola & Nieminen** (**1974**) used regression analysis to demonstrate that the formulation of **Voce** (**1948**) (Eq. 4) - subsequently extended by **Hockett & Sherby** (**1975**) (Eq. 5) - are more accurate descriptions of the behaviour of aluminium alloys, which exhibit stress saturation.

$$\bar{\sigma} = K\bar{\varepsilon}^{n} \qquad \textit{Eq. 3}$$

$$\bar{\sigma} = \bar{\sigma}_{Sat} - (\bar{\sigma}_{Sat} - \bar{\sigma}_{o})e^{(-\alpha\bar{\varepsilon})} \qquad \textit{Eq. 4}$$

$$\bar{\sigma} = \bar{\sigma}_{Sat} - (\bar{\sigma}_{Sat} - \bar{\sigma}_{o})e^{(-\alpha\bar{\varepsilon}^{p})} \qquad \textit{Eq. 5}$$

In the above equations *K* denotes the strength coefficient; $\bar{\sigma}_{o}$ the initial yield stress; $\bar{\sigma}_{Sat}$ the stress where the hardening curve begins to saturate; and α and *p* are dimensionless, material-dependent constants.

The sensitivity of formability to the strain hardening exponent is demonstrated by the models of **Swift** (**1952**) and **Hill** (**1952**). Swift used **Considère's** (**1885**) condition to predict that under proportional loading, the onset of instability occurs at maximum load. For a given strain path ρ ($\varepsilon_2/\varepsilon_1$), the major limit strain of a material characterised by Hill's 1948 yield criterion and Holloman's strain hardening relationship is predicted by Eq. 6. **Banabic & Dannenmann** (**2001**) extended Swift's model by incorporating Hill's 1979 and Hill's 1990 yield curves. Given that the instability described by both Considère and Swift is a diffuse neck, forming limits predicted by Swift's method are inherently conservative.

$$\varepsilon_1{}^{*} = \frac{2n(1+\rho+\rho^2)}{(\rho+1)(2\rho^2-\rho+2)} \qquad \textit{Eq. 6}$$

Hill (**1952**) derived a condition to predict the onset of localised necking (Eq. 7), and the inclination of the neck relative to the strain path (Eq. 8). Hill's condition infers that a neck is sensitive to anisotropy and that a neck can only develop under negative strain paths. For a material obeying Hill's 1948 yield

condition and Holloman's strain hardening relationship, the major limit strain is predicted by Eq. 9. Forming limits predicted by Swift's method are lower than those predicted using Hill's method, which is expected since the two criteria predict diffuse and localised necking respectively. A notable characteristic of both methods is that the predicted FLC_0 matches the value of *n*. Therefore, FLC heights for materials obeying Holloman's hardening relationship can be approximated by *n*.

$$\frac{\delta\sigma}{\delta\varepsilon} = \frac{\sigma}{1+R} \qquad \textit{Eq. 7}$$

$$\theta = \arctan(-\rho)^{1/2} \qquad \textit{Eq. 8}$$

$$\varepsilon_1{}^* = \frac{n}{1+\rho} \qquad \textit{Eq. 9}$$

Where strain hardening enables a material to delay the onset of diffuse necking, strain rate hardening suppresses the onset of localised necking. Strain rate hardening provides materials with an intrinsic resistance to strain localisation, which suppresses the development of the localised neck. A mathematical extension of Holloman's hardening rule is often used to account for strain rate sensitivity ($\delta\bar{\sigma}/\delta\dot{\bar{\varepsilon}}$) where the strain rate hardening exponent *m* is analogous to the strain hardening exponent *n* (Eq. 10). **Ghosh** (**1977**) performed tensile tests on different strain rate sensitive materials to demonstrate the positive impact of *m* on post-uniform elongation.

$$\bar{\sigma} = K\bar{\varepsilon}^n\dot{\bar{\varepsilon}}^m \qquad \textit{Eq. 10}$$

Marciniak et al. (**1973**) included provision for strain rate hardening within the M-K model by incorporating Eq. 10. They concluded that strain rate hardening increases biaxial limit strains even for low *m*-values, and changes the curvature of the FLC. A similar conclusion was drawn by **Hutchinson & Neale** (**1977**) who used non-linear analysis to demonstrate the sensitivity of small changes in *m* on retarding neck localisation. **Neale & Chater** (**1980**) examined the impact of anisotropy, strain hardening, and strain rate hardening on formability using the extended M-K model developed by **Hutchinson & Neale** (**1978**). Neale & Chater concluded that strain rate hardening increases formability in plane strain, and reduces the gradient of the FLC in biaxial tension.

According to **Marciniak et al.** (**2002**) the strain rate sensitivity of most automotive-grade materials is small at room temperature; for steel it is slightly positive and for aluminium alloys zero or slightly negative. However, at elevated temperatures, the influence of strain rate becomes more significant. The impact of temperature on formability was investigated and discussed by **Chu** (**2013**). **Chu** (**2013**) developed an apparatus to conduct temperature-controlled Marciniak formability tests of AA5086 at 20, 150, and 200°C at punch speeds of 0.1, 1, and 10mm/s. The results showed that each combination of temperature and strain rate produced a different FLC. At 150°C, reducing the forming speed from 10mm/s to 1mm/s increased the height of the FLC by 35%. At 200°C, reducing the forming speed from 10mm/s to 1mm/s increased the height of the FLC by 55%. **Chu** (**2013**) concluded that formability increases with increasing temperature and decreasing forming speed, and that the positive effect of temperature on formability can be compensated by an increase in forming speed.

2.2.3 Surface Strain Heterogeneity

Yoshida (**2014**) states that in many formability investigations, sheet metals are treated as homogeneous entities. Visual inspection of the strain topographies in Figure 11 suggests that DIC-measured strains exhibit complex spatial fluctuations at magnitudes above the expected

measurement error. Therefore, treating a localised neck as a homogeneous entity at the macro-scale may not be appropriate. This observation raises a question regarding the source of this behaviour, and how it should be characterised. One possible basis for this behaviour is micro-scale heterogeneity which does not homogenise at the macro-scale.

At the micro-scale, plastic deformation occurs through the slip of crystallographic planes, which is the discrete movement of adjacent planes in a grain that are preferentially aligned to the direction of the applied stress. In grains whose orientations favour slip, deformation occurs primarily within the grain. The amount of deformation that occurs within each grain depends upon the grain's orientation, the local Taylor factor, and any physical restriction imposed by neighbouring grains. In grains whose orientations do not favour slip, deformation occurs primarily at the grain boundaries due to the shear displacements required to rotate the grain to preserve grain-to-grain compatibility. Plastic deformation is accompanied by surface roughening which develops from different origins and materialises at different length scales. Surface defects at the atomic scale, such as slip steps, arise from dislocations which penetrate the material surface. Surface defects at the macro-scale, which are more likely to influence the strain topographies measured by **Wang et al.** (**2014**), have been linked to microstructural inhomogeneity, crystallographic texture effects, and the rotation of surface grains.

One example of a macro-scale defect is the "orange peel" surface condition. "Orange peel" is the result of each surface grain having a difference orientation to that of its neighbour. Under an applied load each grain will deform to a different extent and, due to the additional freedom available to surface grains, may also be subject to a rotation. The strain incompatibility between surface grains causes a non-uniform normal displacement field which roughly maps the granular structure of the material. Another second example is the "banded" surface profile which appears on certain alloys. **Wittridge & Knutsen** (**1999**) note that bands running parallel to the tensile direction emerge on the surfaces of stainless steel, and that bands running perpendicular to the tensile direction emerge on the surfaces of aluminium alloys. "Banding" occurs when colonies of similarly-oriented grains collectively deform, creating an out-of-plane displacement which is visible on the sheet surface, at a magnitude above that of the "orange peel" condition. According to **Li** (**2012**), the characteristics of macro-scale surface roughening mechanisms are dictated by a material's crystalline structure; grain size; the textures present; and the existence of multiple phases. Each of these is discussed herein.

Osakada & Oyane (**1971**) postulated that the amplitude of a material's free-surface roughness is directly related to its crystalline structure - specifically the number of available slip systems. Their rationale was that the number of available slip systems within a crystalline structure governs the ability of individual grains to consistently adapt to the macroscopic deformation. Osakada & Oyane performed compression tests on a multitude of materials and showed that HCP metals (3 moveable slip systems) exhibit the strongest roughening tendency; BCC metals (48 systems) exhibit the weakest tendency; and FCC metals (12 systems) in between the two.

$$R'_{BCC} < R'_{FCC} < R'_{HCP} \qquad \textit{Eq. 11}$$
(R': Surface roughness)

Following a visual inspection of AA5XXX alloys subject to compression tests, **Kienzle & Mietzner** (**1967**) suggested that surface roughness is also a function of grain size. **Osakada & Oyane** (**1971**) elaborated upon this suggestion by deriving a proportional, linear relationship (Eq. 12) between surface roughness and average grain size for AA5XXX alloys. **Stoudt & Ricker** (**2002**) analysed AA5052 under tensile conditions and confirmed that a linear relationship exists between surface roughness and grain size. Stoudt & Ricker independently derived a linear relationship between the

rate of surface roughening and grain size. These conclusions corroborate industrial observations that roughening at the scale of the grain size, such as the "orange peel" condition, increases with increasing grain size.

$$R' = cd\bar{\varepsilon} \qquad \textit{Eq. 12}$$

(R': Surface roughness, c: experimentally derived constant, d: average grain diameter)

Collective deformation of large colonies of similarly-textured grains results in an undulating surface, where the undulations' magnitudes are higher than the individual grain size. Surface conditions that have been observed include ridging, roping, and irregular grooving, with the bands varying in depth between 10µm and 50µm. Banding has been observed by **Graf & Hosford** (**1994**) and **Baczynski et al.** (**2000**) when deforming aluminium; by **Tadros & Mellor** (**1978**) when deforming steel; and by **Wilson et al.** (**1981**) when deforming copper. Published research has shown that banding is particularly prominent when a significant mis-orientation exists between groups of textures. **Baczynski et al.** (**2000**) used electron backscatter diffraction (EBSD) to measure crystallographic orientations in deformed specimens of AA6111T4. Measured EBSD maps demonstrated that the locations of bands on the surfaces of AA6111T4 were accompanied by colonies of Goss-oriented grains. **Raabe et al.** (**2003**) performed a comprehensive analysis of AA6022 using photogrammetry, confocal microscopy, metallography, and EBSD. Raabe et al. concluded that the joint presence of Cube and Goss colonies stimulates strong surface strain heterogeneity.

Micro-strain heterogeneity is known to occur in dual phase steels where strong strain partitioning exists between martensitic particles and the ferrite matrix. **Tasan et al.** (**2014**) examined microscopic plastic behaviour of DP600 and DP800 using a miniaturised Marciniak setup, and showed that the dimensions and dispersion of the two phases have significant influence on micro-scale strain heterogeneity. For dual phase steels with large ferrite grains and small martensite particles, strain heterogeneity is strongly influenced by the ferrite grain size. Experimental measurements showed that in this type of microstructure, intra-granular straining manifests as narrow bands which eventually spread throughout the material. Conversely, for dual phase steels which have smaller ferrite grains and higher martensite content, strain behaviour is dictated by the distribution of the martensite. When fine particles of martensite are homogeneously distributed throughout the ferrite matrix, plastic deformation manifests as a series of thin strain bands spread over the microstructure. This ensures that strains are homogeneously-dispersed throughout the ferrite matrix. However, when the microstructure contains predominantly bulky particles of martensite, the martensite is able to accommodate higher levels of stress. This causes straining to be concentrated in a small sample of ferritic grains that are preferentially orientated to the loading direction, resulting in a more heterogeneous strain distribution.

The appearance of heterogeneity at the macroscopic level is significant - not only for the purpose of characterising the "high-frequency" strain topographies that were identified, but also for formability itself. According to **Marciniak et al.** (**2002b**) the magnitude of a macroscopic imperfection affects the initiation of unstable plastic flow, and large imperfections initiate the onset of instability at lower levels of strain. This was confirmed by **Tadros & Mellor** (**1978**) who used the M-K model to predict FLCs for steel, aluminium, and brass sheets. In each case the size of the initial imperfection was varied. It was shown that the predicted limit strain of the steel sheet decreased by 23% for only a 1.2% change in the initial defect. Tadros & Mellor hypothesised that this sensitivity helps explain the scatter in experimental limit strains, since any inherent geometrical defect will subtly vary between specimens. Tadros & Mellor also recognised that the impact of strain topography on the character of the forming limit should be investigated.

2.3 CHARACTERISING FORMABILITY

To precisely characterise formability, it is necessary to overcome the ambiguity that comes with subjectively positioning the FLC within scattered limit strains. **Strano & Colosimo** (**2006**) assert that statistical methods are necessary to address the inherent randomness of failure.

One of the earliest approaches to statistically characterise limit strain scatter was made by **van Minh et al.** (**1974**). In this work forming limits of around 500 steel specimens were measured and recorded. Following an analysis of the errors in the experiments, van Minh et al. concluded that the standard deviation of the forming limits is greater than can be explained by the strain measurement error, so the scatter itself must be a manifestation of some material property. Specifically,

> *"…the failure process in sheet is in itself a probabilistic phenomenon."*

To characterise the scatter, van Minh et al. calculated the confidence interval of measured strains about the mean projected strain path. Formability was then represented as a three dimensional diagram, shown in Figure 14a. The horizontal plane represents the principal strains which are measured on the specimen, and the vertical ordinate indicates the probability of failure, i.e. the proportion of specimens which are expected to fail if they are all strained by this amount.

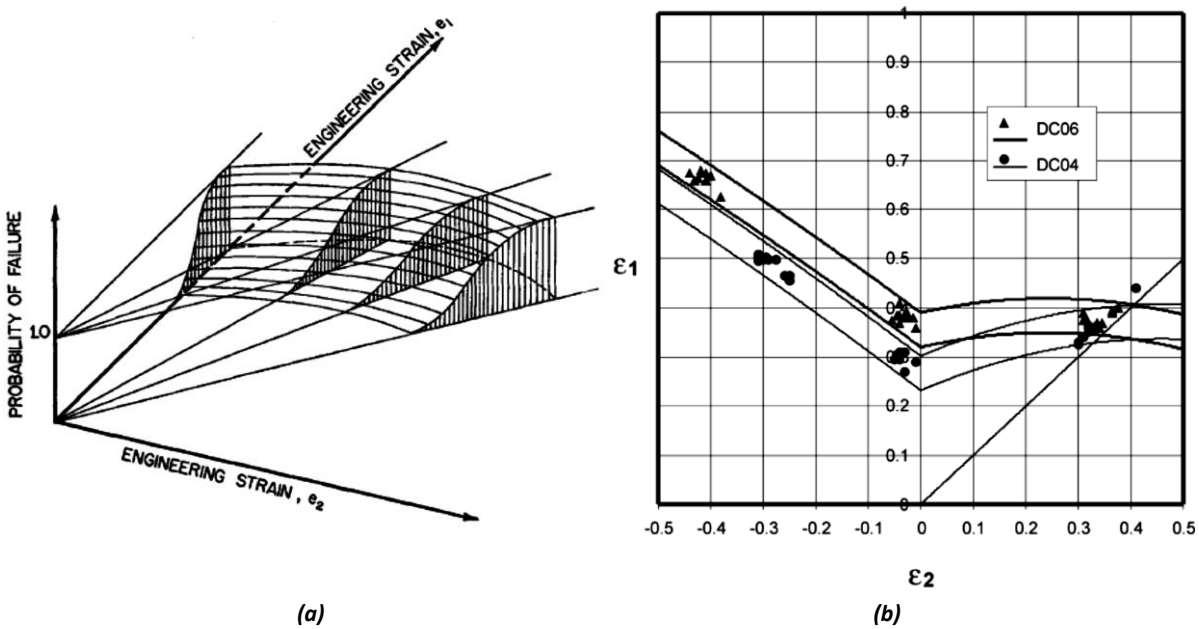

Figure 14: (a) A probabilistic forming limit diagram proposed by** van Minh et al. **(**1974**), (b) A FLB proposed by** Janssens et al. **(**2001**)

Janssens et al. (**2001**) proposed an alternative statistical method to precisely position the FLC, and characterise the scatter around the curve. Firstly, a reference FLC is drawn through the mean limit strain measured at each strain path. The scatter is then characterised by the perpendicular distance of each limit strain from the reference FLC. The standard deviation of the scatter is used to calculate confidence intervals about the FLC, which are subsequently plotted on the FLD (Figure 14b). This locus has become more generally known as the Forming Limit Band (FLB). The width of the band calculated for two mild steels is of the order of 0.9 (true major strain). Like **van Minh et al.** (**1974**), Janssens et al. attributed limit strain scatter to material behaviour rather than the measurement procedure. Janssens et al. also proposed that the FLB should substitute the FLC/safety margin combination, since the uncertainty caused by formability variation is accounted for during FLB calculation.

Strano & Colosimo (**2006**) describe two regression models for characterising formability. The first model is a linear regression (Eq. 13) fitted to limit strain data. The response variable *y* is the major strain, and the predictor variable ***X*** the minor strain. The fitted model predicts, for a given value of minor strain, the expected value of major strain at the forming limit. Strano & Colosimo used a second order polynomial function to ensure the contour of the FLC is well matched. A linear regression model also enables the construction of an FLB, which can be calculated from the 100(1-α)% prediction intervals (Eq. 14) of the regression function.

$$y = a + \beta \boldsymbol{X} + E \qquad \textit{Eq. 13}$$

$$y \pm t_{\frac{\alpha}{2},n=2} \sqrt{\sigma^2 \left(1 + \frac{1}{n} + \frac{(x - \bar{x})^2}{\sum_{i=1}^{n}(x_i - \bar{x})^2}\right)} \qquad \textit{Eq. 14}$$

n is the number of failed observations, $t_{\frac{\alpha}{2},n=2}$is the upper α/2 % of a t-distribution with *n*-2 degrees of freedom, and σ^2 is the error variance.

The second regression model proposed by **Strano & Colosimo** (**2006**) is motivated by their observation regarding the effectiveness of the FLB is describing the risk of failure. They noted that to deliver robust stamping processes, forming engineers are inclined to design panels with strains as far away from the lower FLB as possible. This technique represents a rough approach to risk minimisation as the FLB only provides a confidence interval for the position of the FLC – not a precise measure of the risk of failure. Strano & Colosimo recognised that to quantify the risk of failure, a description of the transition from a safe strain state to a failed strain state is required. They proposed that logistic regression is a more effective method for quantifying the probability of failure.

Logistic regression, like linear regression, is based on a functional relationship between predictor variables and a response variable. However, in a logistic regression, one is interested in predicting the probability of the response variable obtaining a certain value/state, rather than predicting the value itself. In this scenario, Strano and Colosimo were concerned with predicting the probability of a strain value being “safe” or “failed”.

In logistic regression the response variable *z* is introduced. *z* assumes a value of 0 with probability (P_0) if the strain value is safe, or a value of 1 with probability (P_1) if the strain value has failed. Consequently, the odds of observing failure are P_1/P_0, or $P_1/(1-P_1)$. The logistic regression function uses a logarithmic transformation of the odds ratio (referred to as the logit function) as the dependent variable in a generalised linear model:

$$ln\left(\frac{P_1}{1 - P_1}\right) = \alpha + \boldsymbol{\beta X} \qquad \textit{Eq. 15}$$

According to Strano & Colosimo the model’s prediction variable structure $\boldsymbol{\beta X}$ is a polynomial comprising combinations of principal strains:

$$ln\left(\frac{P_1}{1 - P_1}\right) = \hat{\alpha} + \sum_{i=1}^{q} \hat{c}_i {\varepsilon_1}^i + \sum_{j=1}^{r} \hat{d}_j {\varepsilon_2}^j \qquad \textit{Eq. 16}$$

where $\hat{\alpha}$, $\hat{c}_i$ (i = 1:q), and $\hat{d}_j$ (j = 1:r) are the regression coefficients calculated by maximum likelihood estimation. Once the prediction variable coefficients have been estimated, the probability of failure (P_1) is directly calculated from the principal strains:

$$P_1 = \frac{\exp\left(\hat{\alpha} + \sum_{i=1}^{q} \hat{c}_i {\varepsilon_1}^i + \sum_{j=1}^{r} \hat{d}_j {\varepsilon_2}^j\right)}{1 + \exp\left(\hat{\alpha} + \sum_{i=1}^{q} \hat{c}_i {\varepsilon_1}^i + \sum_{j=1}^{r} \hat{d}_j {\varepsilon_2}^j\right)} \qquad \textit{Eq. 17}$$

When the model has been fully defined, values of P_1 are calculated for a range of principal strain combinations. The resulting regression function is presented as a contour map on the FLD (the Formability Map, or FM, displayed in Figure 15) showing the probability of failure for different principal strain pairs.

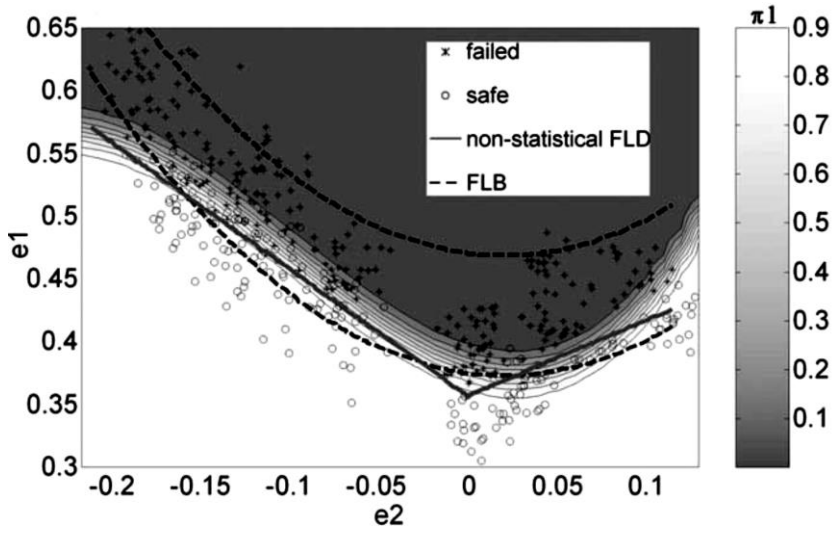

Figure 15: Formability Map calculated using logistic regression by *Strano & Colosimo* ***(****2006****)***

The FM provides an ideal measure of the risk of failure for materials deformed under proportional loading conditions. However, the accuracy of the logistic regression is dependent upon the availability of “safe” and “failed” strain measurements. **Strano & Colosimo** (**2006**) used strain measurements originally made by **The AutoSteel Partnership** (**2003**). Strains measured over fractured specimens of mild steel were classified as either "safe" or "failed" depending on their proximity to failure. Previous analysis of experimental methods in Section 2.1.3 has shown that an objective method for defining the size and location of a localised neck remains elusive. Therefore, classifying strains as “safe” or “failed” is currently a subjective process. The accuracy of the FM cannot be certain until an objective method for identifying a localised neck on a specimen is realised.

2.4 Influence of Strain Path Non-Linearity on Formability

Material specimens stretched during formability tests are deformed under strictly controlled conditions. Industrial stamping operations, meanwhile, invoke deformation conditions outside those the laboratory test. An almost universal feature of stamping operations is that areas of stamped panels are subject to non-proportional loading conditions. Examples include material flowing from a binder system into a die wall, or material forced into a styling feature by successive operations. Deviation from initial loading conditions affects the proportionality of material deformation, with perfectly linear, unbroken strain paths rarely observed in automotive panels.

Graf & Hosford (**1993**) published exhaustive research into the impact of strain path non-linearity on the formability of AA2008T4. Specimens were pre-strained in uniaxial tension, plane strain, and

biaxial tension along the rolling and transverse directions. Subsequent formability characterisation of the pre-strained specimens showed that uniaxial pre-strain raises the RHS of the FLC; plane strain pre-strain raises the FLC extremities away from $FLC_{0;}$ and biaxial pre-strain lowers the entire FLC. This research was mirrored by **Graf & Hosford** (**1994**) in a similarly exhaustive analysis of AA6111T4. Like their previous research into AA2008T4, results showed that biaxial pre-strain lowers the entire FLC, whilst uniaxial pre-strain raises the RHS of the FLC. Graf and Hosford concluded that careful tooling design can induce loading conditions which raise the level of formability above the proportionally-loaded FLC.

Laukonis & Ghosh (**1978**) performed Marciniak-type testing on specimens of aluminium-killed steel and AA2036T4. The impact of strain path non-linearity on formability was examined by pre-straining specimens in biaxial tension to different strain levels, before measuring the specimens' formability. When subject to uniaxial straining, the strain distribution of the pre-strained steel specimens suffered a rapid loss of uniformity. The strain distribution of the aluminium specimens did not suffer as rapid a loss of uniformity. Rapid deviation from a uniform strain distribution signifies a tendency towards earlier instability initiation. Consequently, FLC heights of steels were shown to decrease with biaxial pre-strain at a much higher rate than aluminium.

Kohara (**2005**) investigated the impact of bilinear strain paths on formability by deforming specimens of AA1050O in three combinations: uniaxial tension followed by uniaxial tension in the perpendicular direction; equibiaxial tension followed by uniaxial tension; and uniaxial tension followed by equibiaxial tension. Uniaxial tensile straining followed by orthogonal uniaxial tensile straining resulted in a decrease in formability. Equibiaxial tensile straining followed by uniaxial tensile straining increases increased formability in plane-strain. Uniaxial tensile straining followed by equibiaxial tensile straining increased formability in biaxial tension in certain cases.

Stoughton & Yoon (**2012**) resolved that due to the inevitable non-proportional loading that occurs in an industrial stamping operation, strain path non-linearity is an unavoidable outcome. The sensitivity of the FLC to even small amounts (<5%) of pre-strain demonstrates that even strains that follow quasi-linear strain paths cannot be assessed against the initial-strain FLC. Consequently, **Stoughton & Yoon** (**2012**) concluded that a static FLC is incapable of reflecting the risk of failure of a manufacturing process, and that formability (as characterised by the FLC) should be treated as an inherently dynamic characteristic. The authors concluded:

> *"...few measures are more limited in application than the initial-strain FLC for materials in the as-received condition."*

To overcome the dependency on initial-strain FLCs, **Volk et al.** (**2012**) proposed a metamodel which accounts for strain-path non-linearity. A conclusive analysis of HC300X was performed by deforming specimens along bilinear strain paths and varying both the pre-strain direction and pre-strain magnitude. A response surface was constructed from the results to quantify the change in formability for a given bilinear strain path. This model has since been integrated into the AutoForm finite element software to manipulate FLCs for unique strain paths.

Strain path sensitivity has served as motivation for several authors to research less-sensitive formability criteria. **Arrieux et al.** (**1985**) postulated that transforming the FLC into orthotropic stress space results in a formability criterion (the limit stress curve, or FLSC) which is independent of deformation history. **Zhao et al.** (**1996**) used the M-K model to predict FLCs and FLSCs under linear, bilinear, and trilinear strain paths. Whilst the predicted FLCs exhibited the typical strain path sensitivity, the shapes and locations of the equivalent FLSCs were almost identical. However,

experimental evidence does not fully support claims of FLSC strain path insensitivity. For example, **Yoshida, Kuwabara, et al**. **2007**) performed tube expansion experiments such that stresses could be directly measured. Results showed that the FLSC is sensitive to strain path non-linearity if the path change isn't accompanied by unloading.

The sensitivity of the FLC to strain path non-linearity has far-reaching consequences for established stamping processes. Circle Grid Analysis (CGA) is commonplace during new tool commissioning to measure the final strain field of the stamped panel. However, strains determined solely from the distortion of the final grid shape shouldn't be considered a state measurement, since the final grid shape could be achieved from an infinite number of paths. Comparing CGA measurements to an initial-strain FLC cannot be used to assess the formability of a stamped part. Likewise, the sensitivity of the shape, location, and height of the FLC cannot be mitigated by a simple safety margin applied to the initial-strain FLC.

2.5 DISCUSSION

This review has identified sources of uncertainty in the process of measuring formability. These uncertainties contribute towards the scatter typifying experimental results, causing ambiguity when positioning the FLC. This review has also identified alternative statistical techniques to more precisely characterise formability. Following this review it is appreciated that there are critical limitations in the application of conventional formability criteria to assess industrial panels. These aspects are discussed below.

2.5.1 Characterising Formability

The two test methods advocated in ISO12004-2 – the Nakazima and Marciniak tests – are able to replicate the range of strain paths required to fully characterise formability. Of these tests, the proportional, in-plane deformation conditions invoked by the Marciniak test enable intrinsic material formability to be measured in isolation of any extrinsic process conditions. The conditions of the standardised Marciniak test are unlikely to significantly contribute towards scattered limit strains.

By contrast, the "position-dependent" method advocated by ISO12004-2 for determining formability is likely to contribute towards scattered limit strains. Uncertainty is generated by estimating strain behaviour at the onset of localised necking, rather than identifying the onset of localised necking itself. This limitation has been partially addressed in the literature by advanced “time-dependent” methods. These proposals have shown that continually recording specimen deformation at the ISO12004-2 prescribed frame rate of 10Hz is adequate to capture the onset of localised necking.

Whilst “time-dependent” methods enable strain measurements at the forming limit to be exploited, there is significant uncertainty surrounding which measurements to use, and how to characterise them. Current methods pre-constrain strain analysis to a small area of the test specimen. Pre-constraining analysis to a small area restricts the ability to fully and accurately describe the strain characteristics of the localised neck. A method for objectively defining the geometry of a localised neck is necessary to avoid ambiguity in interpreting strain measurements at the forming limit.

A new observation made in this review is that DIC-measured strains exhibit heterogeneous behaviour at the macro-scale, at levels higher than the expected measurement error. The strain topographies identified in Figure 11 expose complex spatial and temporal strain fluctuations. A correlation between this topographic character and plastic deformation has not been identified in the literature, although it is postulated that micro-scale heterogeneity which fails to homogenise at

the macro-scale might be a contributing factor. Certainly, inherently variable strain behaviour has yet to be appreciated in the characterisation of the forming limit. Heterogeneous behaviour at the macro-scale is likely to contribute towards scattered limit strains.

The review of the literature identified that statistical methods are a logical solution for overcoming the subjectivity in positioning the FLC. The FM proposed by **Strano & Colosimo** (**2006**) usefully characterises formability as a “risk of failure” from strains measured over an entire specimen. However, the logistic regression used to construct the FM requires "safe" and "failed" strains on a specimen to be identified. Since current methods cannot objectively locate and characterise a localised neck, “safe” and “failed” strains cannot be objectively identified. This limitation further emphasises the need to more accurately characterise strain behaviour at the forming limit.

2.5.2 Assessing the Formability of Industrial Panels

Formability is more than a simple, static material property. It is a dynamic function of both intrinsic material properties and extrinsic process conditions. Whilst the material itself contributes towards formability, evidence in the literature demonstrates that the stamping process has similar (if not more) influence. This review of the literature shows that complex interactions between anisotropy, strain hardening, strain rate hardening, structural heterogeneity, and the strain path followed affect the initiation of, and suppression of, instability in sheet metal. These interactions raise concerns regarding the use of conventional, static FLCs to assess the formability of industrial panels. Particular concern arises from the sensitivity of forming limits to strain path non-linearity. A realistic assumption is that infinite strain path permutations exist in an industrially stamped panel.

To describe each strain path permutation, accurate formability assessment requires a theoretically infinite number of FLCs, each with a unique height, shape, and location. Two methods of addressing this problem appear in the literature – this first is to adapt the "datum" FLC to account for this dynamism through a multidimensional model; the second involves identifying an alternative domain to represent formability. By measuring the formability of selected strain path combinations, **Volk et al.** (**2012**) built a representative multidimensional model of bilinear strain paths for HC300X. Advantages of this approach include its experimental verifiability and ease of incorporation into forming simulations. Disadvantages include the significant experimental effort required to fit the model, and the restriction on only describing strain paths undergoing a single path change. Whilst strain path sensitivity provides compelling evidence to pursue alternative formability criteria, the sensitivity of alternative criteria to other factors such as anisotropy, non-planar stress states or temperature is unknown. Further developments of formability criteria must accept that formability is a complex function of multiple interacting variables.

2.5.3 Methodology and Contribution of this Work

The difficulty in accounting for infinite strain path combinations has resulted in the static FLC remaining the dominant method for assessing formability. However, regardless of whether single or multiple strain paths arise in the manufacturing operation, formability remains characterised by the level and shape of an FLC following the desired path(s). To precisely determine the level and shape of the FLC, the onset of necking has to be accurately and precisely measured.

It is typically assumed (e.g. **Banabic & Vos** (**2007**)) that scatter originates from variation in specimen-to-specimen bulk material properties. However, **Wang et al.'s** (**2014**) data and exploratory DIC measurements made in the course of this work also show the presence of a high-frequency or 'noisy' distribution of strains overlaid on the expected strain field. In this work, the 'noisy' strain distribution was found to be significant compared to measurement uncertainty. A major contribution of this

work was to understand the effect of this factor on the uncertainty of individual forming limit measurements. To accomplish this:

1) The measurement uncertainty of the DIC system was established
2) Full-field strains were measured in Marciniak tests using DIC
3) Strains from the beginning of deformation up to the onset of necking were characterised using statistical models
4) A novel 'time-dependent' technique using the statistical characterisation was developed to identify the onset of necking, and describe the neck itself
5) Following the technique of **Strano & Colosimo** (**2006**), strains at the onset of necking were described using logistic regression to create a Formability Map. However, whereas **Strano & Colosimo** (**2006**) quantified the uncertainty of forming limits for a large number of experiments, in this work, the forming limits of individual measurements was quantified

2.6 CONCLUSIONS

- The scatter arising from formability tests is due to ambiguity in measuring the formation of a localised neck
- The "position-dependent" method of determining formability is constrained to estimating the true forming limit, since the onset of localised necking is not directly measured, nor is the locus of the neck defined
- "Time-dependent" methods demonstrate that the onset of necking is reliably determined from the deformation history of specimens
- No objective technique of identifying or describing a neck within a specimen was identified in the literature
- Heterogeneous strain behaviour is observed during plastic deformation and at the onset of localised necking. This is a new observation, which was not addressed by the authors, and is not currently considered during the formability measurement
- A suggested cause of heterogeneity is surface roughening. Surface roughening is a complex, dynamic characteristic existing at several measurement scales, with a material's crystallographic structure, grain size, textures, and effective plastic strain contributing towards its evolution
- The Formability Map, constructed using logistic regression, characterises formability as a risk of failure, thus making decision making in industry less fraught
- Monotonic loading conditions are rarely realised in industrially stamped panels. Any strain determined solely from the initial and final shape of an element cannot be used for formability assessment
- Formability must be considered a dynamic function of intrinsic material properties and extrinsic processing conditions

Strano & Colosimo (**2006**) asserted that statistical methods are necessary to address the inherent randomness of failure. Whilst statistical methods have been applied to characterise forming limits, they have not been used to characterise raw topographic strain data. To address the research gaps identified in the literature, the application of statistical methods will be extended to objectively characterise the topography of, and identify the localised neck within, DIC measurements.

The objective of this Engineering Doctorate is to statistically characterise heterogeneous strain behaviour during plastic deformation and at the onset of localised necking.

3 A NEW STATISTICAL METHOD FOR DETERMINING AND REPRESENTING FORMABILITY

In this chapter, the development of a new statistical method for determining and representing formability is described. The statistical method was developed using the following methodology:

Data collection → EDA → Model Construction → Model Verification → Interpretation of Results

The structure of this chapter follows the methodology outlined above. In Section 3.1 benchmark limit strains are calculated for a range of industrially-relevant alloys deformed in a Marciniak test. Using the DIC measurements made in Section 3.1, Section 3.2 describes the application of exploratory data analysis (EDA) techniques to quantify the evolution of strain heterogeneity in the specimens. Section 3.3 introduces statistical clustering as an innovative technique to decipher the inferences of EDA and translate full-field measurements into a quantitative model. A Gaussian Mixture Model is selected to model plastic deformation within the Zone of Evaluation of a Marciniak specimen. An extension to the Gaussian Mixture Model is described in Section 3.4, which demonstrates how the model's parameters are used to objectively identify the localised neck within the strain distribution. Section 3.5 describes how the principles of "time-dependent" methods are extended to the Gaussian Mixture Model to identify onset of localised necking. Section 3.6 collates the developments of previous sections to demonstrate how the risk of failure (risk of a localised neck) is measured in a specimen. These results are used to construct a Formability Map using logistic regression.

3.1 DATA COLLECTION AND FORMABILITY BENCHMARKING

In order to characterise strain behaviour during plastic deformation and at the forming limit, DIC measurements of a sufficiently large sample size of materials must be taken. The BiW of modern vehicles comprises a variety of steel and aluminium alloys. Of those used in Jaguar Land Rover vehicles, the four most prevalent metal groups are AA5XXX and AA6XXX alloys, mild steels, and dual phase steels. An alloy from each metal group is selected for analysis: NG5754O (1.5mm), AA6111T4 (0.93mm and 1.2mm), MS3 (0.9mm) and DP600 (0.9mm and 1.6mm).

Material specimens of each alloy are deformed according to the Marciniak methodology outlined in ISO12004-2. A minimum of five different specimen geometries are manufactured for each material to replicate a range of strain paths between uniaxial and equibiaxial tension. As per the standard, carrier blanks are manufactured from ductile mild steel and mirror the specimen geometries with the inclusion of a central 33mm diameter hole. A monochromatic speckle pattern is applied to the gauge length using an airbrush, as per the method described in Submission 3. Deformation is recorded using the ARAMIS DIC system at a rate of 10Hz, and strains calculated based on un-deformed facet geometries of 0.9x0.9mm. Benchmark limit strains are calculated using the "position-dependent" technique described in ISO12004-2, and two of the latest advanced "time-dependent" methods: the method of **Merklein et al.** (**2010**) and the method of **Volk & Hora** (**2010**).

Limit strains of each specimen, calculated by the three methods, are plotted in principal strain space in Figure 16. Following convention, the mean limit strain of each geometry is plotted in Figure 17. Reference FLCs are drawn by interpolating between mean limit strains.

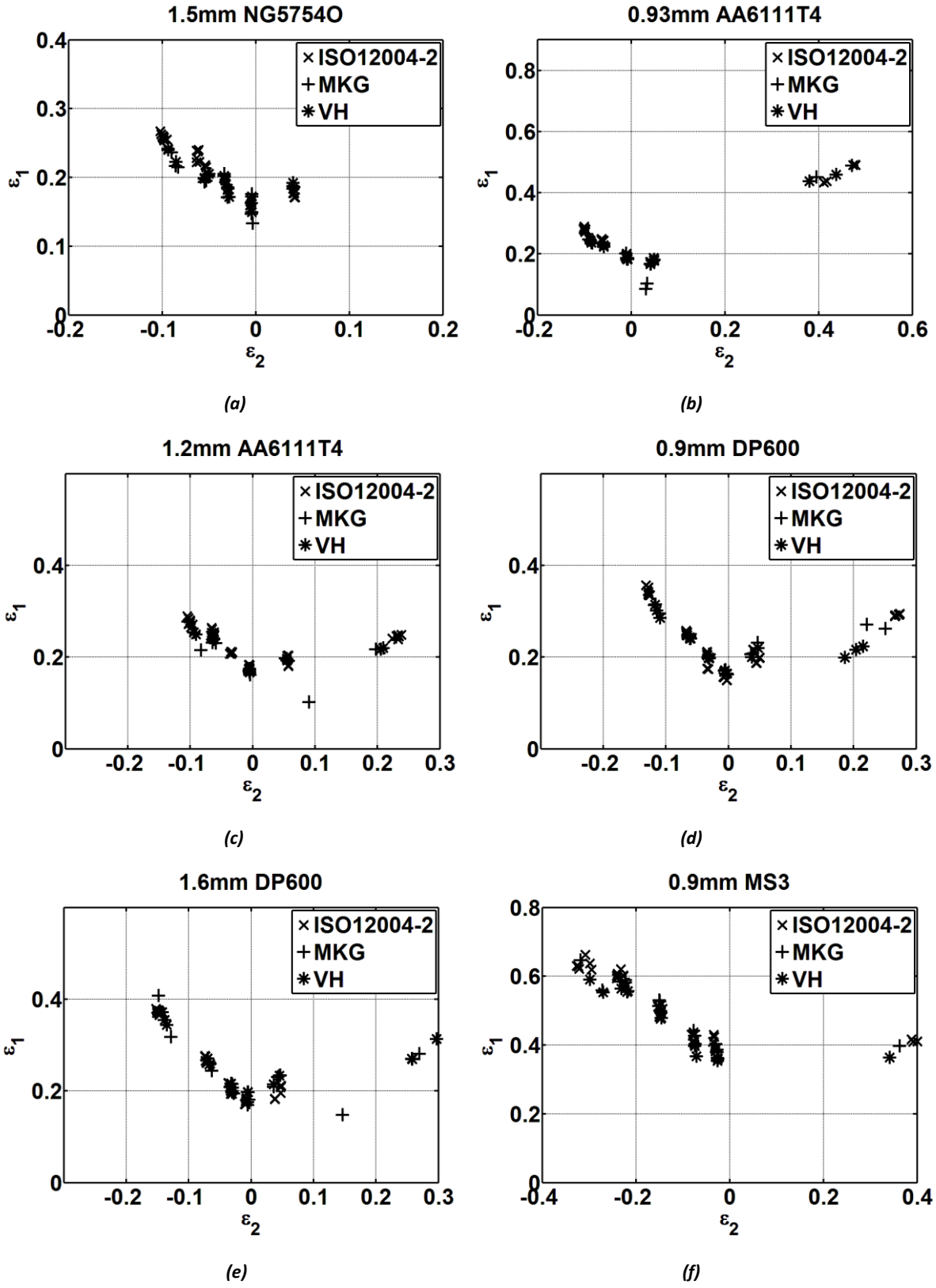

Figure 16: Limit strains measured for six selected materials using the standardised method (denoted ISO12004-2), the method of Merklein et al. **(**2010**)** ***(denoted MKG) and the method of*** Volk & Hora **(**2010**)** ***(denoted VH)***

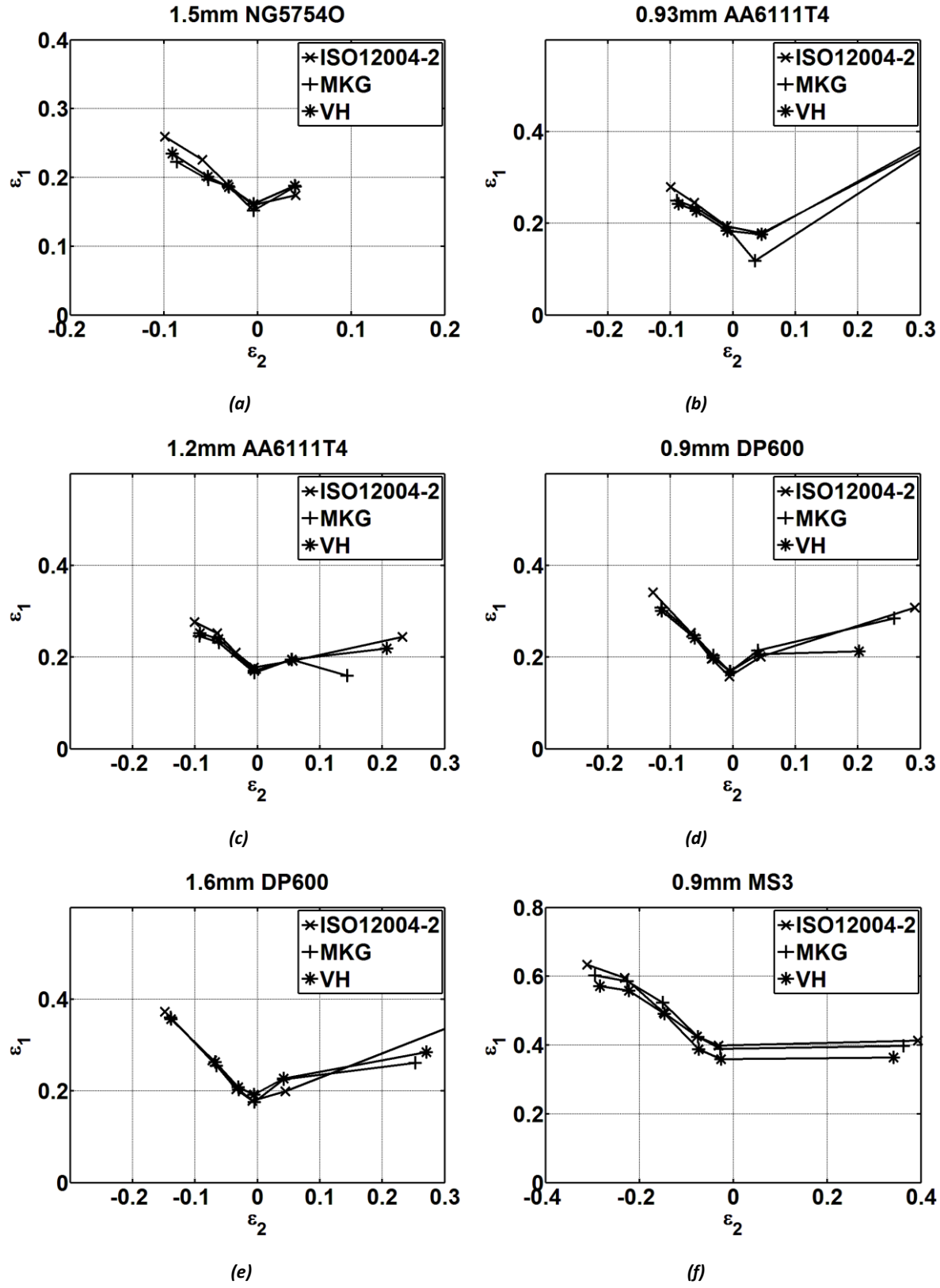

Figure 17: Mean interpolated FLCs measured for six selected materials using the standardised method (denoted ISO12004-2), the method of Merklein et al. **(**2010**) *(denoted MKG) and the method of*** Volk & Hora **(**2010**) *(denoted VH)***

Limit strains calculated using all three methods are scattered. The range of limit strains in plane strain is greatest in 0.9mm MS3, at ≈0.1 true major strain. The range of limit strains in uniaxial tension is greater than 0.1 true major strain for most materials. Limit strain dispersion along the equibiaxial strain path is greater than 0.07 true major strain for all materials.

Mean FLCs of aluminium alloys calculated using the "position-dependent" method are consistently higher than FLCs calculated via "time-dependent" methods. All FLCs of AA6111T4 are closely located between uniaxial tension and plane strain, but diverge in biaxial tension. Plane strain limit strains of 1.2mm AA6111T4 calculated using the method of **Merklein et al.** (**2010**) appear lower than the expected locus. Against convention, limit strains of 0.93mm AA6111T4 in biaxial tension are higher than those for 1.2mm AA6111T4. All FLCs of DP600 are closely located between uniaxial tension and plane strain, but diverge with increasing biaxial tension. The FLC of MS3 calculated using the method of **Volk & Hora** (**2010**) is slightly lower than the other two curves.

The difference between limit strains calculated using the "position-dependent" method and "time-dependent" methods is attributable to the sensitivity of "time-dependent" methods in determining the onset of failure. "Time-dependent" methods determine the onset of failure from an increase in strain rate within a small area of the specimen. The strain rate histories of a specimen of 1.2mm AA6111T4 subject to plane strain are shown in Figure 18. Figure 18a shows the chronology of the mean strain rate derivate inside a 2mm locus as defined by **Merklein et al.** (**2010**). Figure 18b shows the chronology of the mean thinning rate inside the failure area as defined by **Volk & Hora** (**2010**). In both cases broken stick regression is used to objectively locate the onset of localised necking. In this particular specimen, the onset of localised necking calculated using the first method occurs at t = 30.7s, whereas the onset of localised calculated using the second method occurs at the t = 30.9s. With a real time difference of 0.2s, it is concluded that both "time-dependent" methods are sensitive to the onset of localised necking.

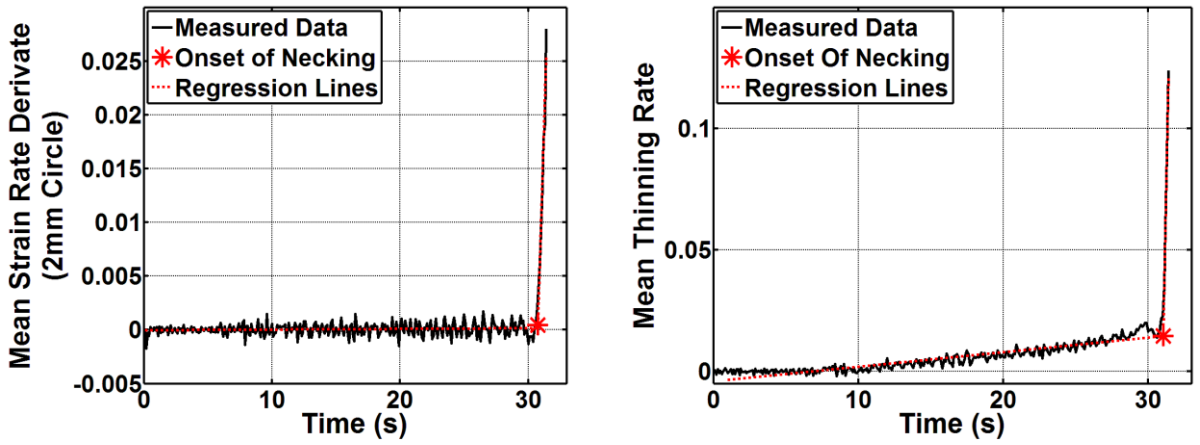

(a) *(b)*

Figure 18: Time series generated for a specimen of 1.2mm AA6111T4 undergoing plane strain deformation using the methods of (a) Merklein et al. **(**2010**)** ***and (b)*** Volk & Hora **(**2010**)**

Whilst sensitivity to the onset of localised necking is a differentiator between the "position-dependent" and "time-dependent" methods, limit strain differences between the two "time-dependent" methods arise from their respective definitions of the localised neck. In Figure 19, two ε_3 strain topographies of the aforementioned Marciniak specimen are shown, independently of the specimen's geometry. Figure 19a shows the strain distribution in the Zone of Evaluation at the onset of localised necking calculated using the method of **Merklein et al.** (**2010**). Figure 19b shows the strain distribution in the Zone of Evaluation obtained using the method of **Volk & Hora** (**2010**).

Below each strain field is an outline of the localised neck defined by each method. Each method locates the localised neck in different areas of the specimen. Both topographies exhibit spatial strain fluctuations, similar to those identified in the literature (Figure 11). Using the method of **Merklein et al.** (**2010**) the neck is believed to contain 9 DIC elements, with major strains varying from 0.1667 to 0.1739 and minor strains from -0.0062 to -0.0034. Using the method of **Volk & Hora** (**2010**) the neck is believed to contain 51 elements, with major strains varying from 0.2008 to 0.2213 and minor strains from -0.0095 to -0.0029. As a result of the discrepancies between the definitions of the localised neck, discrepancies between limit strains are observed.

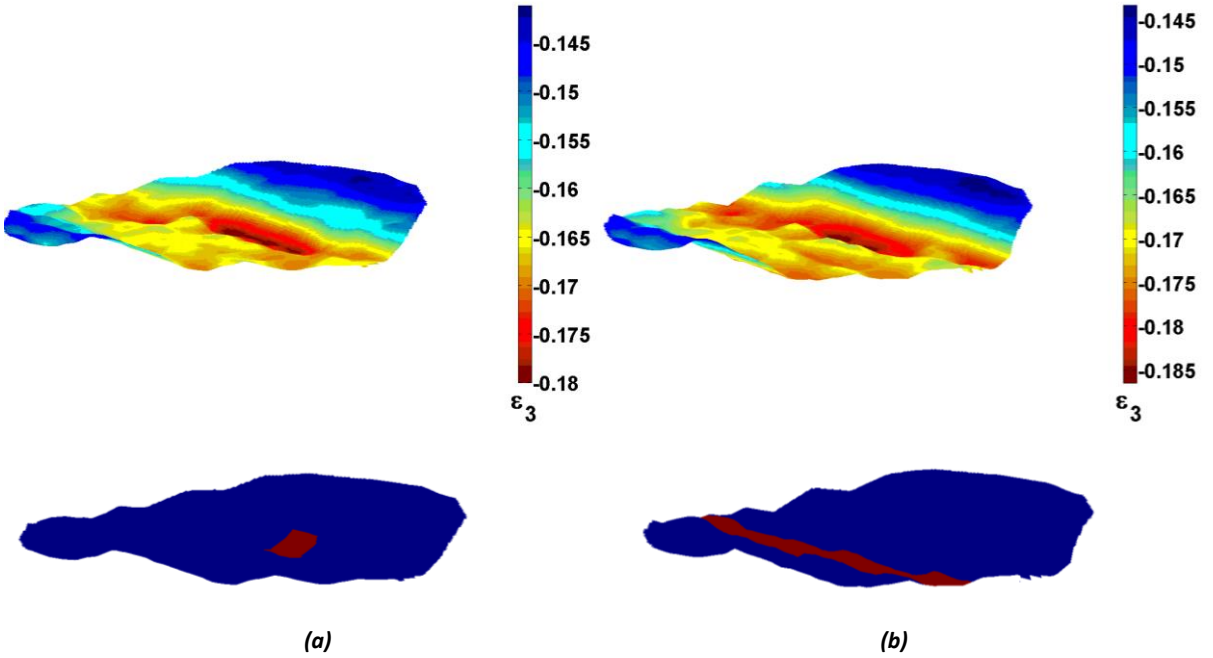

Figure 19: Strain topographies of a specimen of 1.2mm AA6111T4 deformed in plane strain where (a) corresponds to the onset of necking determined using the method of Merklein et al. **(**2010**) *and (b) the onset of localised necking determined using the method of*** Volk & Hora **(**2010**)**

3.2 Exploratory Data Analysis

The topographies of the two DIC measurements selected in Figure 19 illustrate the complexity of the strain distribution that is typically present at the onset of necking. To accurately characterise this behaviour, it is necessary to uncover and describe the underlying structure of the measurements, and identify the localised neck. A practical method of characterising the topography is to describe the statistical character of the strain measurements.

The statistical character of a measurement distribution is described by its central tendency, dispersion, and shape. Exploratory data analysis (EDA) is a well-established statistical tradition for summarising the primary features of distributions, as well as for identifying patterns and trends. Applying EDA techniques to DIC measurements will summarise the statistical behaviour of strains within the Zone of Evaluation, recognise any statistically significant changes which occur during plastic deformation, and help ascertain how strains should be modelled.

3.2.1 Central Tendency and Dispersion

The central tendency and dispersion of a distribution are well described by descriptive statistics such as the median, upper and lower quartiles, and extreme values. Boxplots are a visual EDA technique for combining several descriptive statistics into a single diagram. In a traditional boxplot the length

of the box reflects the interquartile range (the upper hinge is the 75th percentile and the lower hinge the 25th percentile) with the middle line showing the median. Whiskers protruding from each hinge show the extreme measurements. The central tendency and dispersion of a DIC measurement can therefore be easily interpreted from the geometry of a boxplot.

Features of a boxplot also reveal information about the distribution's shape. Symmetrical boxplots are characteristic of Gaussian-shaped distribution. Non-symmetrical features imply the presence of skewness, meaning the distribution cannot be accurately modelled by a Gaussian function. For example, non-symmetrical whiskers imply the distribution is skewed in favour of the longest whisker. Non-central median lines within the box also imply the distribution is skewed.

Boxplots calculated from successive DIC measurements offer the ability to objectively study trends and patterns in the distribution of strains in a Marciniak specimen. Since AA6XXX alloys exhibit distinctive necking behaviour, boxplots are constructed for DIC measurements of 1.2mm AA6111T4 specimens deformed during the benchmarking exercise described in Section 3.1. Three specimens are selected to cover a range of strain paths: 60mm, 140mm, and 220mm width specimens reflect the uniaxial tension, plane strain, and equibiaxial tension strain paths respectively. The measurement history of each specimen contains 306, 316, and 380 DIC measurements. Each measurement grid contains a minimum of 550 elements - sufficient to calculate descriptive statistics. Boxplot analysis is performed by importing each DIC measurement into MATLAB, where descriptive statistics of the thickness strain (ε_3) measurements are calculated to construct the boxplots. To enable the statistical history of each experiment to be contained in a single diagram, box plots are constructed at increments of 10 DIC measurements. Boxplots calculated for each of the three specimens are shown in Figure 20.

All boxplots in Figure 20 show that the locations of the thickness strain (ε_3) of the three specimens follow a common declining trend. Increased deformation leads to a non-linear reduction in the specimens' thicknesses. The boxplots show the presence of strain dispersion throughout the deformation of the Marciniak specimens. This dispersion increases with increasing deformation. Comparing this dispersion to the measurement uncertainty of the DIC system shows that it is significant even at the early stages of plastic deformation. Thus, contrary to the common assumption that the strain distribution in a plastically deforming sample is homogeneous and smoothly varying, this data shows that a spread of strains exists throughout the duration of the tests. A significant increase in strain dispersion is seen during latter stages of deformation, especially between the penultimate and final boxplots. The interquartile range increases from 0.012 to 0.021 between the final two boxplots of the uniaxially deformed specimen described in Figure 20a. In the plane strain specimen described in Figure 20b an increase from 0.010 to 0.021 is seen. In the equibiaxial specimen described in Figure 20c an increase from 0.013 to 0.020 is seen.

Further interrogation of Figure 20 reveals that the strain distribution in Marciniak specimens is not consistently symmetrical. Figure 20 shows that boxplots are initially symmetrical, remaining so until the penultimate DIC measurement. The final boxplots of the uniaxial and plane strain specimens, however, are non-symmetrical. Mild skewness is seen in the final boxplot in Figure 20a where the length of the lower whisker is greater than the upper whisker. More significant skewness is seen in the final boxplot in Figure 20b where the median line shifts towards the lower hinge. The specimen deformed in equibiaxial tension remains closely symmetrical throughout deformation.

Deviation from symmetry, combined with a sudden increase in strain dispersion, implies that a statistically-significant state change occurs within Marciniak specimens prior to fracture. To verify this inference, a more detailed analysis of the of the distributions' shapes is required.

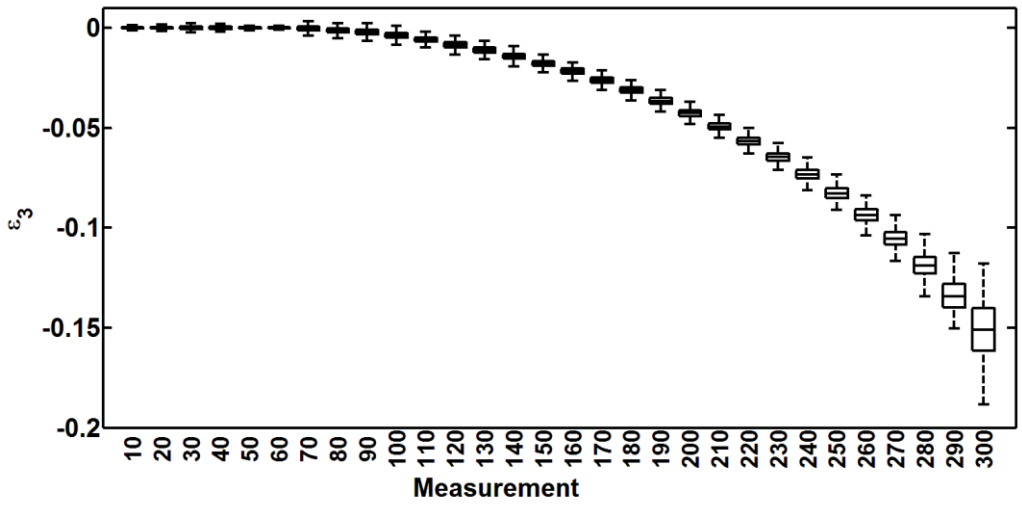

(a)

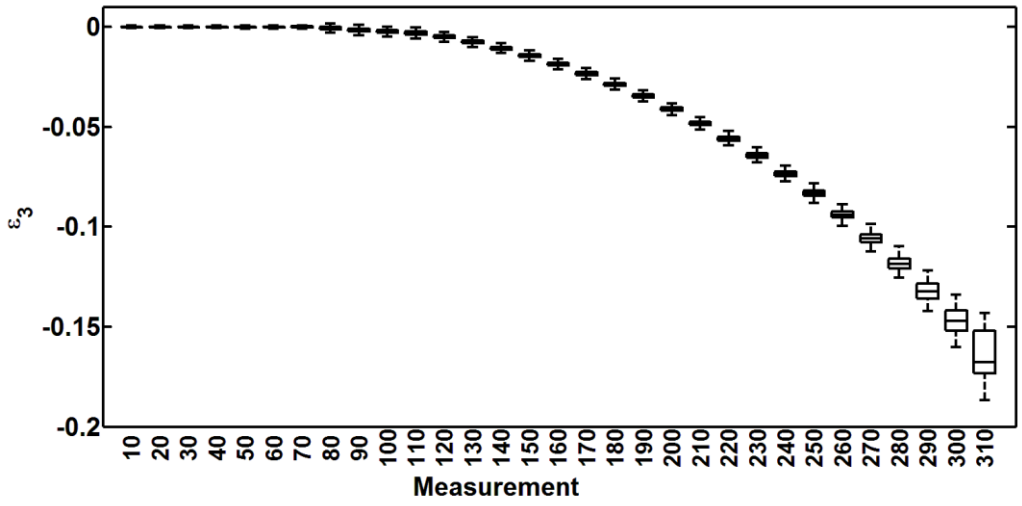

(b)

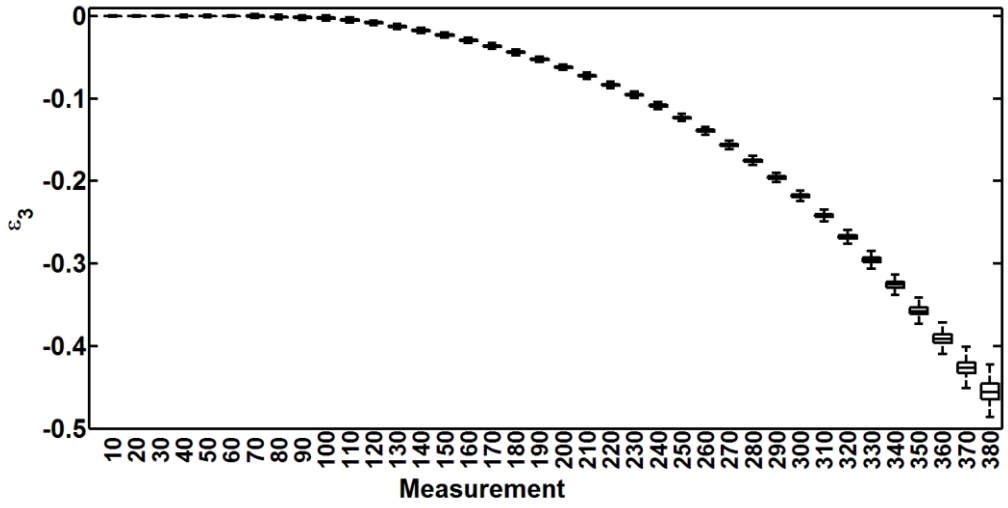

(c)

Figure 20: Boxplots showing the change in distribution of ε_3 in the Zone of Evaluation of Marciniak specimens stretched in (a) uniaxial tension, (b) plane strain, and (c) equibiaxial tension

3.2.2 Distribution Shape

A distribution's shape is modelled by its probability density function (PDF). Histograms and kernel density estimates are both popular non-parametric methods for estimating the PDFs of datasets. Histograms are a discrete representation of a continuous dataset, constructed by dividing datasets into a finite number of "bins". Plotting the frequency of each "bin" as a bar chart provides a discrete estimate of the dataset's PDF, as shown in Figure 21a. Despite their simplicity histograms are limited by their lack of continuity, and shape sensitivity to the "bin" size. Alternative kernel density estimates (KDE) are a continuous representation of a dataset. KDEs are constructed by overlaying a kernel function (commonly a standard Gaussian function) at the location of each measurement, as shown in Figure 21b. Summing the kernels for the entire population produces a continuous estimate of the PDF. Estimated PDFs constructed using KDE are smoother than those constructed using histograms, resulting in a better reflection of the distribution shape of the underlying dataset

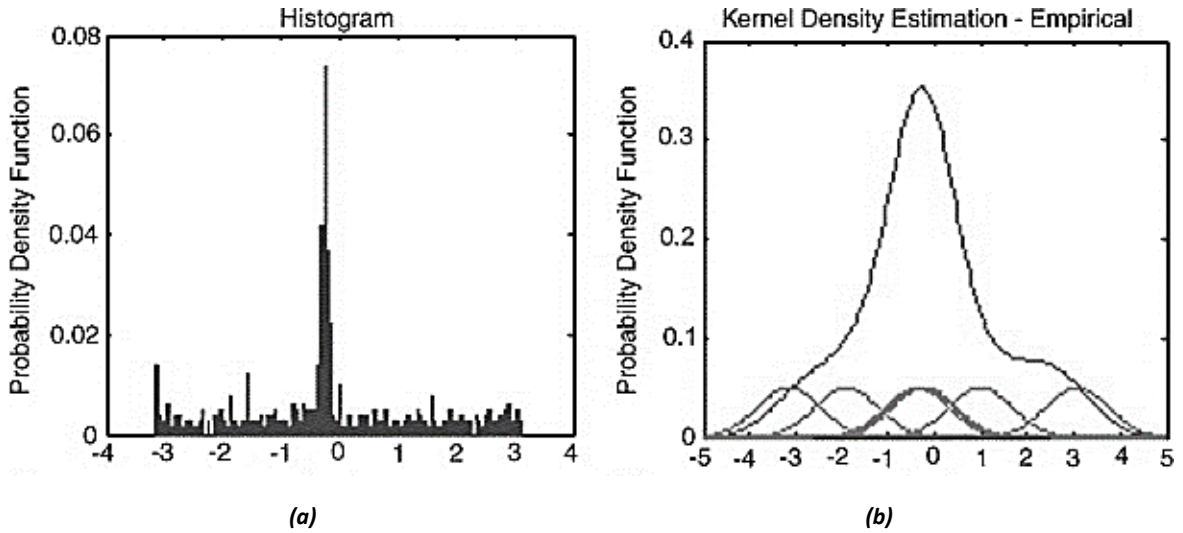

(a) *(b)*

Figure 21: Examples of (a) a histogram, and (b) kernel density estimate used to estimate distribution shape

To better understand the emergence of skewed strains in Marciniak specimens, kernel density estimation is used to estimate the PDFs of the DIC measurements previously analysed using boxplots. A sample of six DIC measurements is taken from each of the three specimens. PDFs are calculated by importing each DIC measurement into MATLAB, and using the statistical toolbox to fit a kernel density estimate using a standard Gaussian kernel. Results are shown in Figure 22, where each plot displays the evolution of the ε_3 distribution.

Figure 22 illustrates more clearly how the shape of the strain distribution evolves with deformation. Firstly, the estimated PDFs confirm that strain distributions of all specimens are closely symmetrical during early plastic deformation. In the case of the equibiaxial sample, symmetry remains throughout deformation. Secondly, it is observed that increased dispersion leads to reduced PDF heights. This is attributable to statistical fundamentals, as $\int(\mathrm{PDF}) = 1$.

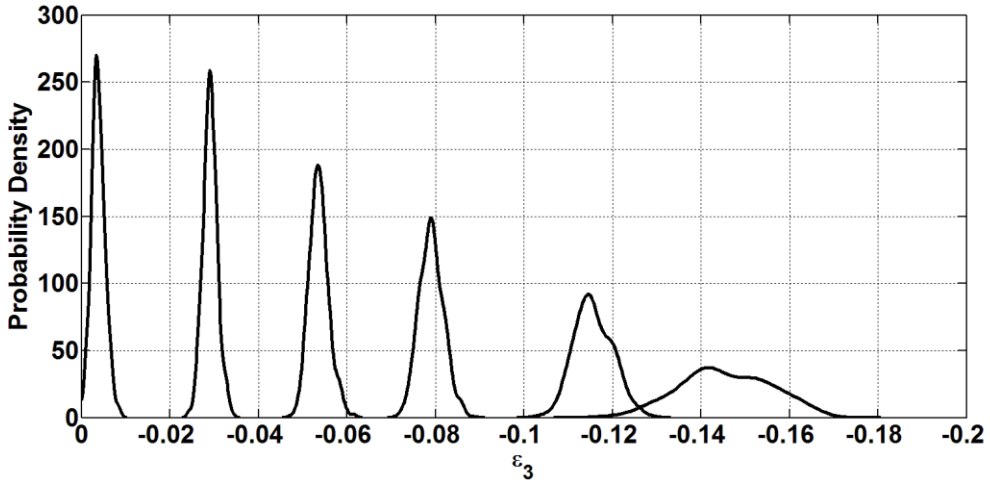

(a)

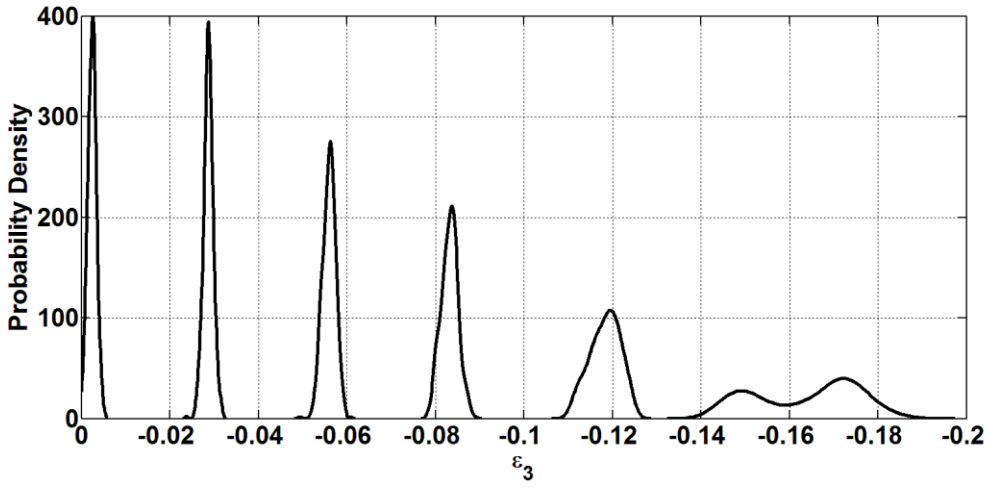

(b)

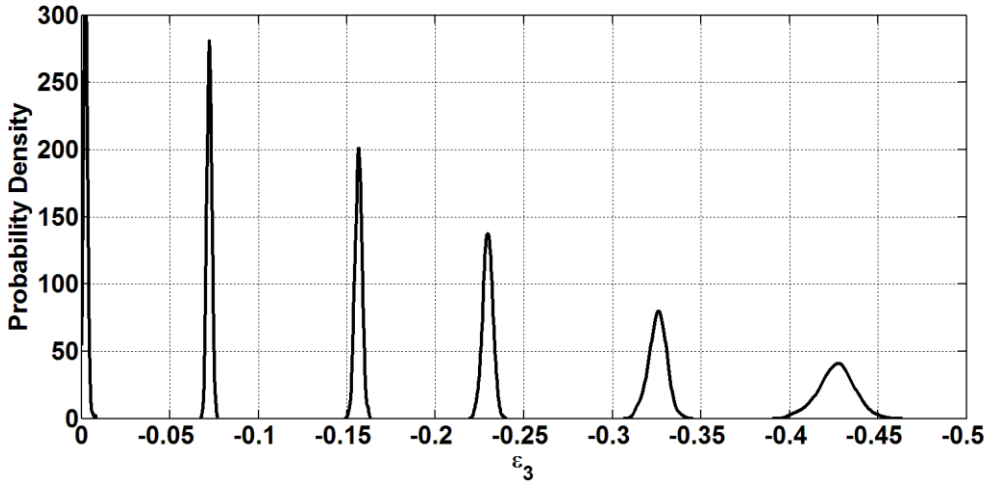

(c)

Figure 22: PDFs showing the evolution of the distribution of strains in a Marciniak specimen deformed in (a) uniaxial tension, (b) plane strain, and (c) equibiaxial tension

Of significant interest is the shape change in the PDFs of the uniaxial (Figure 22a) and plane strain (Figure 22b) specimens in the final selected measurement. Previous analysis in Section 3.2.1 highlighted the emergence of skewness in these measurements. Both Figure 22a and Figure 22b show that rather than a skewed distribution, PDFs exhibit bimodal characteristics. Emergence of bimodality is evident in the penultimate PDF of the uniaxial specimen, as well as the final PDF. Interpreting the plots by visual inspection, modes in the penultimate PDF of the uniaxial specimen are located at $\varepsilon_3 \approx -0.115$ and $\varepsilon_3 \approx -0.118$. In the final PDF modes have relocated to $\varepsilon_3 \approx -0.141$ and $\varepsilon_3 \approx -0.15$. Bimodal behaviour is most pronounced in the final PDF of the plane strain specimen where the modes are located at $\varepsilon_3 \approx -0.148$ and $\varepsilon_3 \approx -0.172$.

Bimodal distributions are characteristic of datasets containing (at least) two statistically distinguishable features. The transition from unimodality to bimodality in the DIC measurements shows that a statistically significant physical state change occurs within Marciniak specimens, just before fracture. Previous analysis of the strain rate history of the plane strain specimen using "time-dependent" methods (Figure 18) has shown that the onset of localised necking also occurs just before fracture. Development of bimodality at a similar time suggests that localised necking is accompanied by a change in statistical character.

EDA has shown that strain topographies are describable using elementary statistics. Furthermore, EDA has shown that the statistical characteristics of the topography change with increased deformation. A parametric model is required to quantify strain behaviour and help identify the underlying physical states causing statistical change. The intricacies observed during EDA demonstrate a necessity to look beyond the conventional Gaussian function to model plastic strain behaviour in a Marciniak specimen.

3.3 A Statistical Model of Plastic Deformation

The patterns observed in EDA reveal that in order to statistically model heterogeneous strain behaviour, the model must be able to describe both unimodal and bimodal distribution shapes, and be able to separate strains within the neck from those in the remaining material. Clustering is a branch of statistical modelling used to identify divisions within a measurement population. Clustering models therefore provide an opportunity to identify strains responsible for PDF bimodality, and to characterise them. Several clustering techniques exist which are applicable to this problem, including connectivity based, centroid based, and distribution based techniques.

3.3.1 Model Selection

3.3.1.1 Connectivity Based Clustering

Connectivity based clustering is based on the hypothesis that measurements which are closely located have more in common than measurements which are far apart. Connections within a population are often illustrated through the use of a dendrogram. A dendrogram is a hierarchical tree showing the similarity of relationships between elements of a population. The tree contains claves (the nodes) and leaves (the end of each clave). The height of each clave demonstrates how similar or dissimilar the underlying claves or leaves are to each other, with higher claves revealing greater dissimilarity between the underlying elements. Each measurement begins in its own cluster, with a computational algorithm then identifying the "closest" data point within the population. The two data points are then merged to form a cluster. Successive clusters are merged until the population is divisible into just two clusters.

Figure 23 shows a dendrogram fitted to the final DIC measurement of the plane strain specimen (responsible for the bimodal PDF in Figure 22b). The connections are calculated using a standard clustering algorithm within MATLAB, with the algorithm computing the ε_3 distance between each cluster. For ease of illustration, Figure 23 is curtailed to show the differences between the 30 most significant clusters.

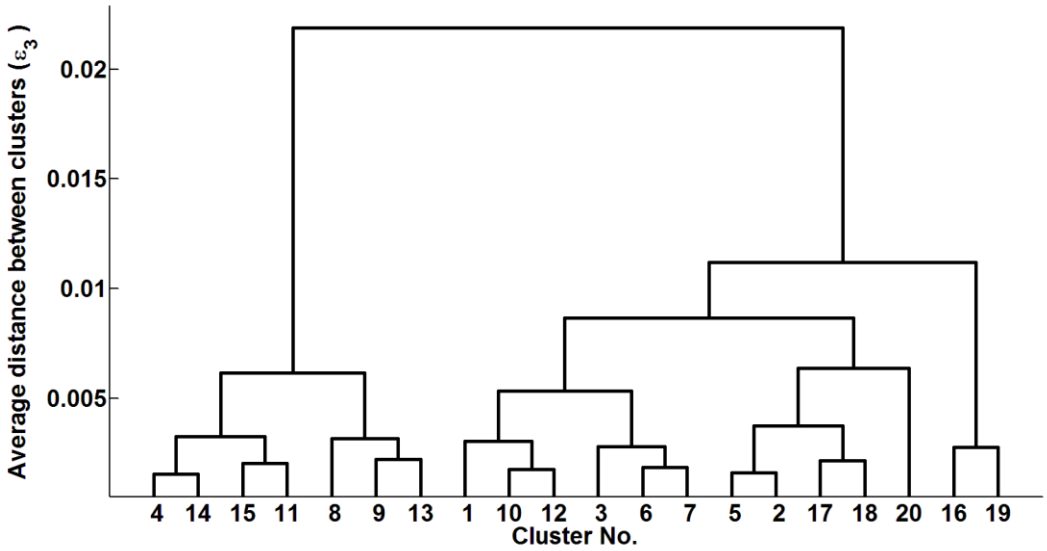

Figure 23: Dendrogram fitted to the final DIC measurement of a 1.2mm AA6111T4 specimen deformed in plane strain

The dendrogram shows that the difference between the two largest clusters is greater than the difference between any of the underlying clusters. This indicates that the population is divisible into two main clusters. Summarising the population as two main clusters supports the observation of PDF bimodality, which also implies the existence of two primary states. The dendrogram shows that the average ε_3 difference between the two primary clusters is approximately 0.021. Visual inspection of the estimated PDF in Figure 22b showed that the difference between the two modal points is approximately 0.024. It is reasonably deduced, based on this similarity, that the two most prominent clusters identified using connectivity based clustering are responsible for PDF bimodality.

3.3.1.2 Centroid Based Clustering

Centroid based algorithms are also used for data clustering. Unlike hierarchical clustering, centroid based clustering also provides quantitative information regarding the underlying population. Centroid based clustering represents a population by a pre-defined number of clusters. Each centroid represents the mean of a cluster. The K-means algorithm is a method for identifying the location of each centroid, and allocating each measurement to a cluster. For a pre-defined number of clusters (two, in this case), the K-means algorithm uses an optimisation procedure to group data into each cluster:

1. Randomly choose initial cluster centroids (the seeds)
2. Calculate the squared Euclidean distance from each data point to each seed
3. Form clusters by assigning each data point to the seed in closest proximity
4. Once all data points are clustered, calculate the centroid of each cluster
5. Calculate the squared Euclidean distance from each data point to each centroid
6. Assign each data point to the centroid in closest proximity

The algorithm iterates until it converges upon the minimum within-cluster sum of squares. Due to the sensitivity of the algorithm to the values of the initial seeds, K-means is often run multiple times with different seeds to identify an optimal outcome. An example of centroid based clustering is shown in Figure 24. The population of 566 ε_3 values from the 310th DIC measurement of the plane strain specimen (responsible for the bimodal PDF in Figure 22b) is shown in Figure 24a. Assuming that two clusters are present within the data, the K-means algorithm available in MATLAB is used to cluster the ε_3 values. The algorithm is run 10 times using different randomly located seeds, with the final clusters and centroids in Figure 24b showing the optimised outcome.

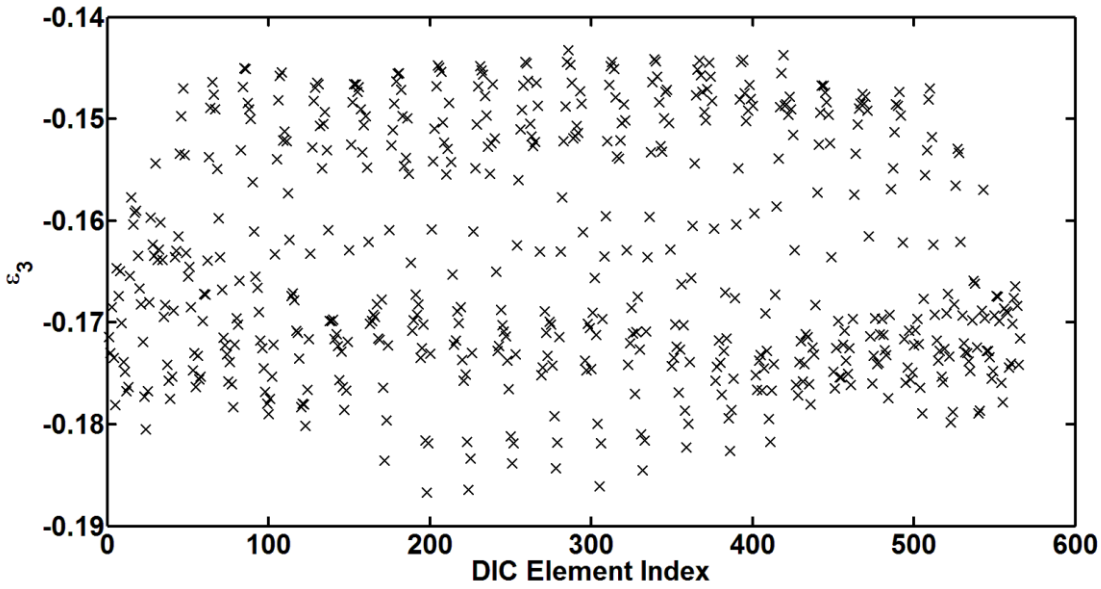

(a)

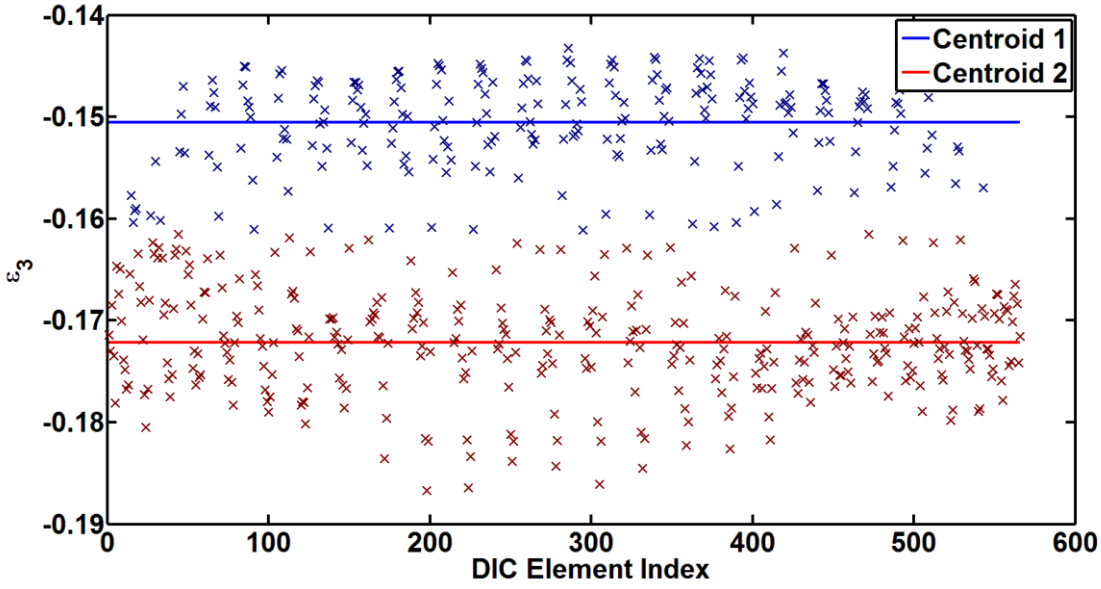

(b)

Figure 24: (a) Raw strain data from a DIC measurement, subsequently clustered using the K-means algorithm in (b) showing the clustered data and centroid positions

Figure 24b shows that the two centroids are located at ε_3 = -0.1506 and ε_3 = -0.1722. These values correspond closely to the modal locations identified in Figure 22b. The difference between the two centroids is 0.0216 – similar to the distance between the two primary clusters calculated using connectivity based clustering. The centroid locations can therefore describe both the separation and the central tendency of each cluster. However, central tendency alone does not fully describe the statistical character of each cluster (nor the population as a whole). Both the dispersion of strains, and the profile of the strain distribution in each cluster must be quantified in order to describe the strain topography within the Zone of Evaluation.

3.3.1.3 Distribution Based Clustering

PDFs have previously been projected using kernel density estimation. If the shape of the PDF is known, it can be quantitatively modelled rather than estimated. The probability density *y* of a measurement population *x* is expressed by:

$$y(x) = f(x|\theta) \quad \textit{Eq. 18}$$

where *f* is the PDF, and θ is a vector of parameters applicable to the function. The PDF of a Gaussian shaped distribution described by a mean (μ) and standard deviation (σ) is expressed by:

$$y(x) = f(x|\theta) = N(x|\mu,\sigma) = \frac{1}{\sigma\sqrt{2\pi}} e^{\frac{-(x-\mu)^2}{2\sigma^2}} \quad \textit{Eq. 19}$$

Distribution based clustering is based on the principle that a population's distribution is the sum of multiple underlying functions. Mixture models are used to describe the PDFs of populations comprising at least one function. A Gaussian Mixture Model (GMM) describes the PDF of a population from the weighted sum of a finite number of underlying Gaussian functions:

$$y(x) = \sum_{k=1}^{K} \pi_k N(x|\mu_k,\sigma_k) \quad \textit{Eq. 20}$$

where *K* is the number of underlying Gaussian functions (components) and π_k is the mixture weight of each component ($\sum_{k=1}^{K} \pi_k = 1$).

Distribution based clustering is performed by calculating the responsibility each component takes for the generation of a particular measurement. Component responsibility is calculated from the relative density of each component at the location of the data point x_A (Eq. 21 and Eq. 22). For a univariate dataset described by two components g_1 and g_2, the crossover point ($P(g_1|x_A) = P(g_2|x_A) = 0.5$) serves as a clustering boundary: measurements below the crossover point have a greater probability of being the responsibility of the first component, measurements above the crossover point have a greater probability of being the responsibility of the second component.

$$P(g_1|x_A) = \frac{g_1(x_A)}{g_1(x_A) + g_2(x_A)} \quad \textit{Eq. 21}$$

$$P(g_2|x_A) = \frac{g_2(x_A)}{g_1(x_A) + g_2(x_A)} \quad \textit{Eq. 22}$$

Direct calculation of GMM component parameters is not possible. To construct a GMM, the model must be fitted to the population using an estimation algorithm. The Expectation-Maximization (EM) algorithm is widely used for GMM fitting. EM is an iterative technique used to maximise the likelihood of the GMM parameters for the fitted dataset. Expectation maximization is a three step iterative method:

1. Initialisation: Make initial estimates for the mixture model parameters ($\pi_{1,2}$, $\mu_{1,2}$, $\sigma_{1,2}$)
2. Expectation: Calculate the responsibilities for each measurement x_N (where N is the population size)
3. Maximization: Re-estimate the mean, variance, and mixture weight for the GMM components using maximum likelihood estimates:

$$\hat{\mu}_1 = \frac{\sum_{i=1}^{N}(P(g_1|x_i)x_i)}{\sum_{i=1}^{N}(P(g_1|x_i))} \qquad \hat{\mu}_2 = \frac{\sum_{i=1}^{N}(P(g_2|x_i)x_i)}{\sum_{i=1}^{N}(P(g_2|x_i))} \qquad \textit{Eq. 23, Eq. 24}$$

$$\hat{\sigma}_1{}^2 = \frac{\sum_{i=1}^{N}(P(g_1|x_i)(x_i-\hat{\mu}_1)^2)}{\sum_{i=1}^{N}(P(g_1|x_i))} \qquad \hat{\sigma}_2{}^2 = \frac{\sum_{i=1}^{N}(P(g_2|x_i)(x_i-\hat{\mu}_2)^2)}{\sum_{i=1}^{N}(P(g_2|x_i))} \qquad \textit{Eq. 25, Eq. 26}$$

$$\hat{\pi}_1 = \frac{\sum_{i=1}^{N}(P(g_1|x_i))}{N} \qquad \hat{\pi}_2 = \frac{\sum_{i=1}^{N}(P(g_2|x_i))}{N} \qquad \textit{Eq. 27, Eq. 28}$$

The expectation and maximisation steps are iterated until the difference between the estimated and re-estimated parameters falls below a pre-defined threshold. Once this threshold has been reached the algorithm has converged, resulting in an optimally fitted GMM.

Based on the results of EDA, and the application of other clustering methods, it is speculated that 2-component GMMs can quantitatively model the bimodal PDF character seen in the distribution of ε_3 strains:

$$y(\varepsilon_3) = \pi_1 N(\varepsilon_3|\mu_1,\sigma_1) + \pi_2 N(\varepsilon_3|\mu_2,\sigma_2) \qquad \textit{Eq. 29}$$

To demonstrate the application of GMM, a 2-component model is fitted to the 310th DIC measurement of the plane strain specimen (responsible for the bimodal PDF in Figure 22b). Raw DIC data is imported into MATLAB, where expectation maximisation is performed on the ε_3 measurements until the convergence criterion is satisfied. The resulting GMM PDF is shown in Figure 25. The PDFs of each component and the PDF previously estimated using KDE are included for comparison.

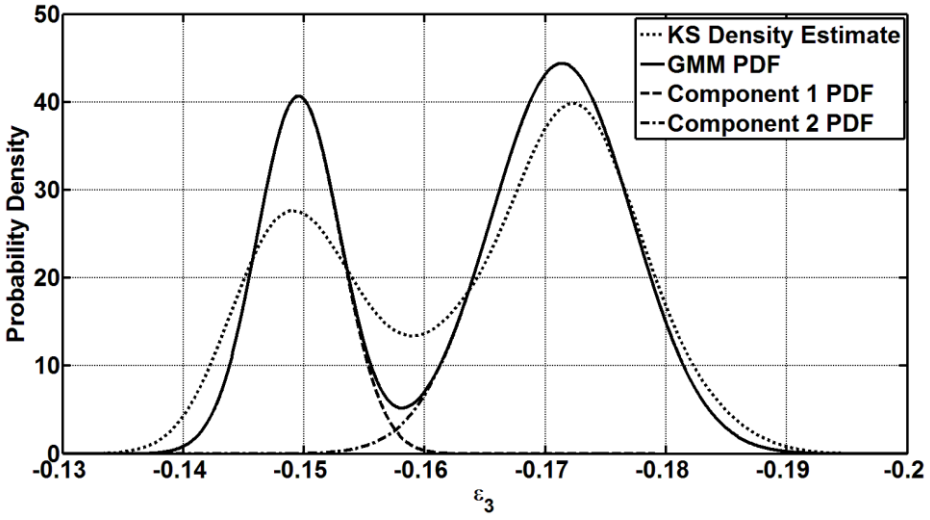

Figure 25: PDF calculated using a 2-component GMM

The fitted GMM model is $y(\varepsilon_3)$ = 0.350N(ε_3 | -0.149, 0.0034) + 0.650N(ε_3 | -0.171, 0.0058).

Figure 25 shows that the GMM PDF reflects the main features of the estimated PDF. Firstly, the locations (means) of the two components are aligned to the modes estimated by the KDE – albeit at higher densities. The locations also mirror the centroids previously calculated using the K-means algorithm. This replication demonstrates that the GMM is capable of capturing the bimodality within the DIC measurement. Secondly, the PDF "trough" is located in approximately the same location as the KDE – albeit at a lower density. The trough's position is aligned to the cross-over point of the two underlying components. The cross-over point is indicative of the location of the clustering boundary. Thirdly, the dispersion of the GMM PDF accurately reflects that of the KDE. Visual inspection shows that modelling the DIC measurement using GMM ensures that the central tendency, dispersion, and shape of the distribution of elements within the DIC measurement are retained by the model.

Used in isolation, the parameters of the GMM are able to characterise the distribution of strains within each component: the mixture weight depicts the relative size of the component, the mean depicts the location, and the standard deviation depicts the dispersion. Used in conjunction with the GMM, these parameters characterise the strain heterogeneity within the Marciniak specimen. The ability to characterise this behaviour, as well as identify the data responsible for the statistical shape change, make the 2-component GMM an ideal tool to model strains in a Marciniak specimen.

3.3.2 Applying Gaussian Mixture Modelling to DIC Measurements

An important observation in the exploratory analysis is the transition from unimodal to bimodal behaviour in the ε_3 distribution. To test the hypothesis that this transition is caused by the onset of localised necking, the DIC measurement when bimodality becomes significant must be identifiable, as must the DIC elements responsible for its emergence. It is therefore critical that 2-component GMMs are able to model the unimodal, transitionary, and bimodal phases of the statistical evolution.

Gaussian mixture modelling is extended to the three specimens of 1.2mm AA6111T4 previously used to analyse the shape change in the ε_3 distribution. Like the investigation in Section 3.2.2, the statistical evolution of each specimen is abridged to six DIC measurements. The ε_3 values of each measurement are imported into the MATLAB environment, where the statistical toolbox is used to fit a 2-component GMM. Table 2 lists the optimised GMM parameters fitted to each measurement. Figure 26 shows the GMM PDFs calculated for each measurement overlain on the PDFs previously estimated using KDE.

Figure 26 confirms that the profiles of the GMM PDFs correctly trace the profiles of PDFs estimated using KDE during each phase of deformation. In the uniaxial specimen, the PDFs retain unimodality in the first four measurements, with the modal locations aligned to the KDE PDFs. The beginnings of the "breakaway" component are visible in the fifth measurement, which is captured by the right-skewness of the GMM PDF. The saddle point in the distribution shape of the sixth measurement is also replicated. In the plane strain specimen, the PDFs retain unimodality in the first four measurements, with the modal locations mirroring those of the KDE PDFs. Like the uniaxial specimen, the beginnings of the "breakaway" component are visible in the fifth distribution. However, unlike the uniaxial specimen, the PDF of the plane strain specimen at this stage of deformation is left-skewed. GMM PDFs of the equibiaxial specimen remain unimodal throughout deformation.

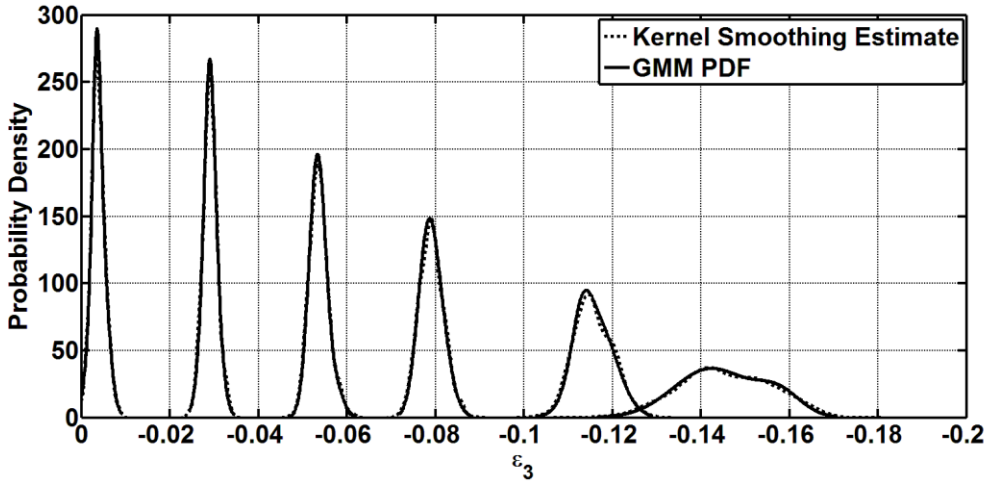

(a)

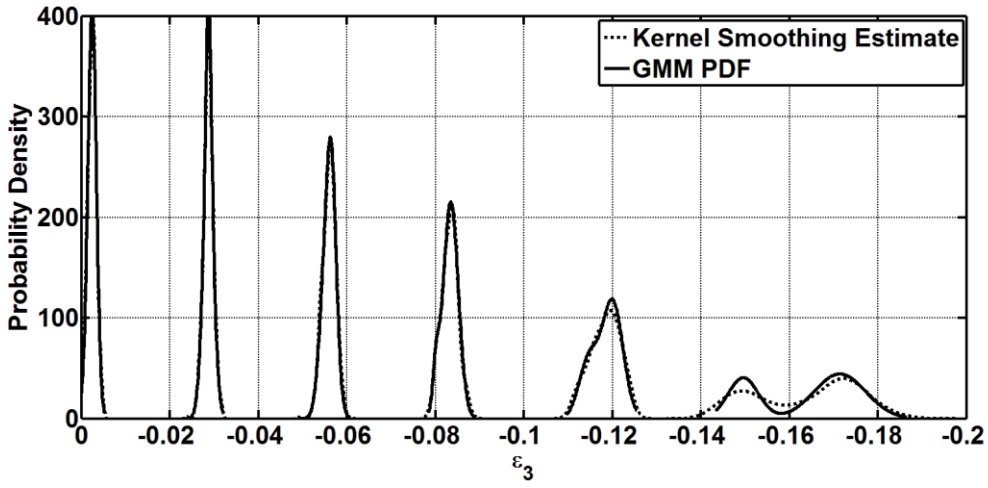

(b)

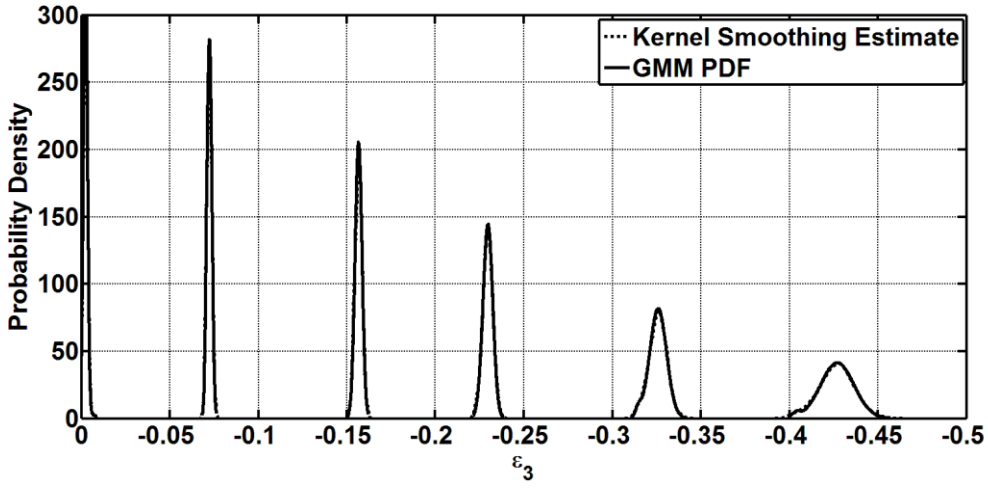

(c)

Figure 26: GMM PDFs showing the evolution of the distribution of strains in a Marciniak specimen deformed in (a) uniaxial tension, (b) plane strain, and (c) equibiaxial tension

The ability of the 2-component GMM to preserve unimodality is explained by the locations of the two components. In the first four measurements of the uniaxial tension and plane strain specimens, and all measurements of the equibiaxial specimen, Table 2 shows the components are very closely located. Superimposing the PDFs of two closely located components yields a unimodal population PDF. GMMs fitted to the bimodal PDFs show that the component locations have diverged. A logical conclusion, therefore, is that the transition from unimodality to bimodality is quantifiable from changes to the component locations.

Geometry	Measurement No.	π_1	π_2	μ_1	μ_2	σ_1	σ_2
60mm	1	0.299	0.701	-0.00350	-0.00390	0.000845	0.00180
	2	0.356	0.644	-0.0290	-0.0292	0.00110	0.00190
	3	0.925	0.0750	-0.0534	-0.0578	0.00190	0.00170
	4	0.620	0.380	-0.0781	-0.0807	0.00230	0.00274
	5	0.202	0.798	-0.113	-0.116	0.00220	0.00450
	6	0.774	0.226	-0.142	-0.157	0.00850	0.00510
140mm	1	0.0456	0.954	-0.00100	-0.00240	0.00140	0.000949
	2	0.771	0.229	-0.0287	-0.0287	0.00120	0.000554
	3	0.830	0.170	-0.0567	-0.0558	0.00150	0.000808
	4	0.0765	0.923	-0.0801	-0.0825	0.000703	0.00170
	5	0.320	0.680	-0.115	-0.120	0.00220	0.00230
	6	0.350	0.650	-0.149	-0.171	0.00340	0.00580
220mm	1	0.992	0.008	-0.00230	-0.00630	0.00110	0.00110
	2	0.242	0.758	-0.0711	-0.0726	0.000995	0.00120
	3	0.235	0.765	-0.155	-0.157	0.00180	0.00190
	4	0.683	0.317	-0.0229	-0.230	0.00290	0.00240
	5	0.0286	0.971	-0.315	-0.326	0.00170	0.00470
	6	0.836	0.164	-0.426	-0.429	0.0105	0.00550

Table 2: GMM model parameters fitted to selected DIC measurements of 1.2mm AA6111T4

Analysis performed in this section has demonstrated that statistical modelling is able to fulfill the objectives of this research. 2-component Gaussian Mixture Models have been applied to characterise strain heterogeneity in Marciniak specimens, and capture the changing statistical state with increased plastic deformation. Furthermore, the ability to utilise GMMs to perform statistical clustering enables the DIC elements responsible for the state change to be identified.

3.4 Describing the Localised Neck using Statistical Clustering

Hypothesis: Emergence of bimodality in the distribution of ε_3 is due to localised necking

Hypothesis: The localised neck is statistically identifiable within the measurement population

To test the hypothesis that diverging statistical states are attributable to the onset of localised necking, the DIC elements responsible for the two states must be located on a necked specimen. The location of these elements within the Zone of Evaluation will determine whether elements drawn

from the second component are inside the localised neck. The location of the strains attributable to each component can be found by performing statistical clustering.

Statistical clustering using a 2-component GMM is performed by calculating the responsibility each component takes for observations within the measurement population. GMMs fitted in Section 3.3.2 show that the two components g_1 and g_2 are not mutually exclusive. Therefore, a probability exists that an observation *A* could be drawn from either of the two components. From Section 3.3.1, the responsibility taken by each component for an observation *A* is calculated from the relative density of each component at the location of the observation:

$$P(g_1(\varepsilon_3)|A) = \frac{g_1(\varepsilon_3)}{g_1(\varepsilon_3) + g_2(\varepsilon_3)}\Bigg|_A \quad \textit{Eq. 30}$$

$$P(g_2(\varepsilon_3)|A) = \frac{g_2(\varepsilon_3)}{g_1(\varepsilon_3) + g_2(\varepsilon_3)}\Bigg|_A \quad \textit{Eq. 31}$$

$g_1(\varepsilon_3)$ and $g_2(\varepsilon_3)$ are the weighted Gaussian PDFs describing the strain distribution of the first and second GMM components respectively. The interest of this research lies in identifying DIC elements which are most likely to be inside the neck. To test the hypothesis that the second GMM component diverges as the result of a localised neck, DIC elements which satisfy the following condition must be identified:

$$P(g_1(\varepsilon_3)|A) < P(g_2(\varepsilon_3)|A) \quad \textit{Eq. 32}$$

Or alternatively, since $P(g_1(\varepsilon_3)|A) + P(g_2(\varepsilon_3)|A) = 1$:

$$P(g_2(\varepsilon_3)|A) > 0.5 \quad \textit{Eq. 33}$$

Two DIC measurements of 1.2mm AA6111T4 undergoing plane strain deformation are analysed. Previous application of "time-dependent" methods in Section 3.1 has shown that the onset of localised necking in this specimen occurs between measurements 307 and 309. A GMM has previously been fitted to the 310th DIC measurement of the specimen which, based on these prior observations, is assumed to be representative of strain behaviour at the formation of the localised neck. The second GMM is fitted to the 315th DIC measurement - the last measurement made before fracture. It is assumed that by this measurement, the localised neck has fully matured, and is visibly distinguishable within the measured strain field. Comparison between the statistical models fitted to both measurements will determine the GMM's ability to characterise the evolution of a localised neck.

The component responsibilities for the 566 elements in the two DIC measurements are calculated in MATLAB using Eq. 31. Each strain in the Zone of Evaluation is subsequently clustered using the condition specified in Eq. 33. "Cluster 1" refers to the elements which have a greater probability of being the responsibility of the first GMM component (component with lower mean), and "Cluster 2" refers to the elements which have a greater probability of being the responsibility of the second GMM component (component with higher mean). It is therefore hypothesised that Cluster 1 contains strain measurements made outside the localised neck, and Cluster 2 contains strain measurements made inside the localised neck.

Figure 27a and Figure 28a show the distribution of ε_3 strains within the Zone of Evaluation at the onset of localised necking and the onset of fracture respectively. Figure 27a shows that high straining occurs within a wide band spanning approximately 2/3rds the length of the Zone of Evaluation. Strains are relatively evenly spatially distributed within this band, although small areas of higher straining are visible. A wide band of increased straining is characteristic of a diffuse neck. Localised regions of higher straining within the band are characteristic of an emerging localised neck - however these regions have yet to nucleate into a band spanning the width of the Zone of Evaluation. Figure 28a shows that at the onset of fracture, the contour of the diffuse neck remains visible in the strain field. However, the magnitude of strains within the locus of the diffuse neck is no longer evenly spatially distributed. Straining is concentrated in a narrow band, at a slight inclination, running across the width of the Zone of Evaluation. The geometry of the band, in combination with the high level of relative straining, is characteristic of a fully formed localised neck.

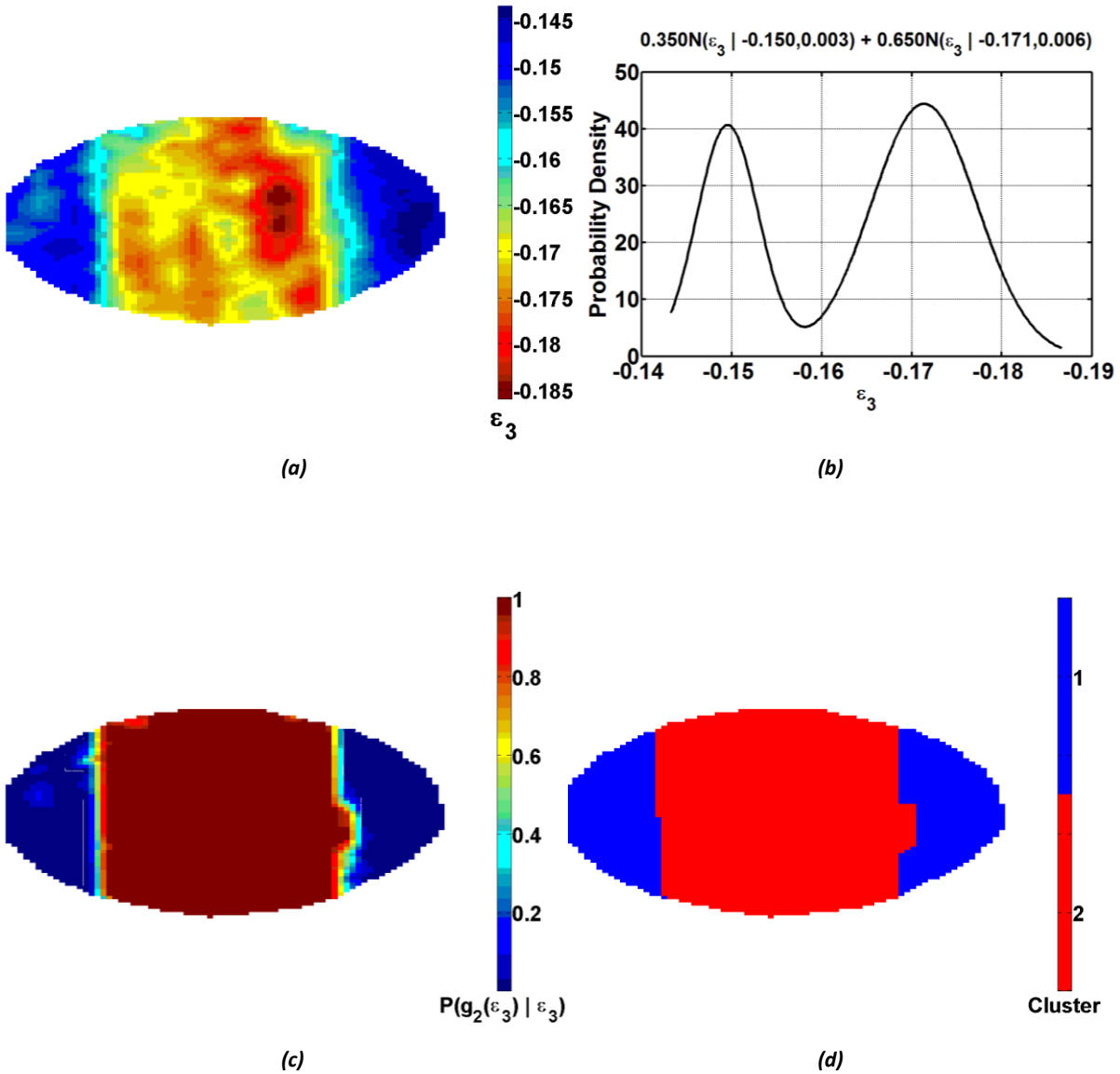

Figure 27: Results of DIC measurement no. 310/316 where (a) is a MATLAB visualisation of the DIC measurement, (b) is the PDF calculated from the fitted mixture model, (c) is the DIC measurement reconstructed to show the probability of each element being drawn from the second component, and (d) shows the position of the clusters on the specimen

Figure 27b shows the PDF calculated from fitting a 2-component GMM to the 310th DIC measurement. Figure 27c shows the probability of individual DIC elements belonging to the second component located in the Zone of Evaluation. Figure 27d simplifies the result into two clusters defined by the condition in Eq. 33. It is observed that the locus of elements with the greatest probability of being the responsibility of the second component follow the outline of strains anticipated to being the diffuse neck. It is also observed that the small areas of high straining are statistically indistinguishable using a 2-component GMM. Visual inspection of the strain field suggests that the diffuse neck comprises approximately 2/3rds of the measurement population. The model described in Figure 27b shows that 65% of the measurement population is attributable to the second component. These observations show that the second component at the onset of localised necking is attributable to the diffuse neck, with the diffuse neck containing 65% of strains within the Zone of Evaluation. At this stage of deformation, the GMM does not distinguish between the diffuse and the emerging localised neck.

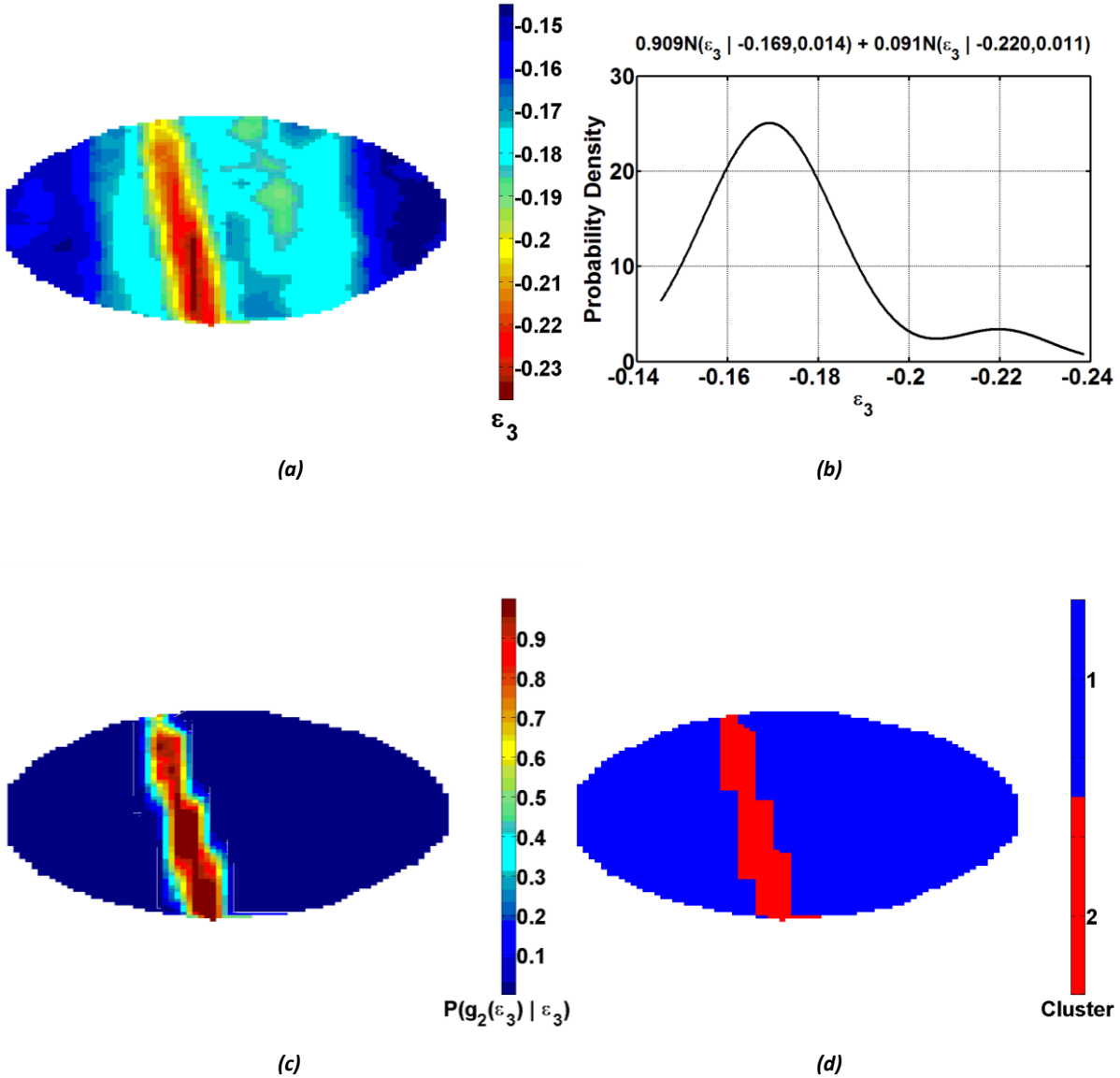

Figure 28: Results of DIC measurement no. 315/316, where (a) is a MATLAB visualisation of the DIC measurement, (b) is the PDF calculated from the fitted mixture model, (c) is the DIC measurement reconstructed to show the probability of each element being drawn from the second component, and (d) shows the position of the clusters on the specimen

Figure 28b shows the PDF calculated from fitting a 2-component GMM to the 315th DIC measurement. The results of statistical clustering are shown in Figure 28c and Figure 28d. Figure 28c shows the probability of individual DIC elements belonging to the second component. Figure 28d simplifies the result into two clusters defined by the condition in Eq. 33. Despite the outline of the diffuse neck still being visible, the GMM demonstrates that the localised neck evolves into a more statistically significant state. Figure 28c and Figure 28d show that strains with a higher probability of being the responsibility of the second component lie within a narrow band spanning the width of the Zone of Evaluation. The dimensions of the band correspond to the band of high straining seen in Figure 28a. The parameters of the fitted GMM reflect the specimen's change in physical state. The difference between GMM component locations increases from 0.021 in the 310th measurement to 0.051 in the 315th measurement. The weighting of the second component reduces from 0.65 to 0.091. Therefore, once the localised neck has fully emerged, it is statistically identifiable by the second GMM component.

Existence of PDF bimodality prior to the full formation of a localised neck shows that bimodality is not uniquely attributable to a localised neck. Figure 27 and Figure 28 show that bimodality is attributable to both pre- and post-localised necking behaviour. However, the GMM is sensitive to the development of a localised neck. Increasing statistical significance of the localised neck causes the second component to transition from representing the diffuse neck to representing the localised neck.

The ability to capture these changing features is the result of avoiding pre-emptive decisions regarding the size or location of the neck. Statistical clustering enables a localised neck to be objectively located on the specimen, as demonstrated in Figure 28c and Figure 28d. This proves the hypothesis that a localised neck is statistically identifiable within the measurement population. A useful advantage of the statistical method is that strain measurements clustered using GMM gain additional information – each element has a calculated probability of being inside the localised neck $\left(P(g_2(\varepsilon_3)|\varepsilon_3)\right)$. This enables the research engineer to accurately quantify the probability that an element of material will neck, thereby overcoming one of the major uncertainties of formability measurement.

3.5 Identifying the Onset of Localised Necking using Gaussian Mixture Modelling

Hypothesis: GMM parameters can be used to identify the onset of localised necking

From the results obtained in Section 3.4, it is recognised that localised necking causes GMM component locations to diverge, and unbalances the components' weights. To identify the onset of localised necking, the DIC measurement before these characteristics become pervasive must be identified.

To test the hypothesis, the entire DIC measurement history of a specimen of 1.2mm AA6111T4 is modelled using 2-component GMMs. A total of 316 unique models are calculated to characterize the strain distribution during deformation. The emergence of, and subsequent evolution of, PDF bimodality has previously been attributed to the location change of the GMM components. A logical first step is to examine the development of μ_1 and μ_2 over the course of the test. Time series of μ_1 and μ_2 are created by deconstructing each GMM fitted to the measurement history. A time series of $|\mu_2 - \mu_1|$ is also created.

Figure 29a and Figure 29b show that until the ≈220th measurement, GMM components are co-located. Between measurements 220 and 305 the two components diverge at an increasing rate,

with the parabolas of Figure 29a suggesting that component locations evolve in a power-type relationship. Between the 305th and 312th measurement, Figure 29a shows that the position of the second component continues to follow its prior trajectory, while the trajectory of the first component begins to saturate. Consequently, Figure 29b shows a marked increase in component separation. The final measurements before fracture show a step increase in both component locations, with the second component exhibiting an extreme change from ≈-0.175 to ≈-0.228 in less than a handful of measurements. A lesser, but nonetheless positive, step change in the first component causes the components to separate further, as shown in the final stages of Figure 29b.

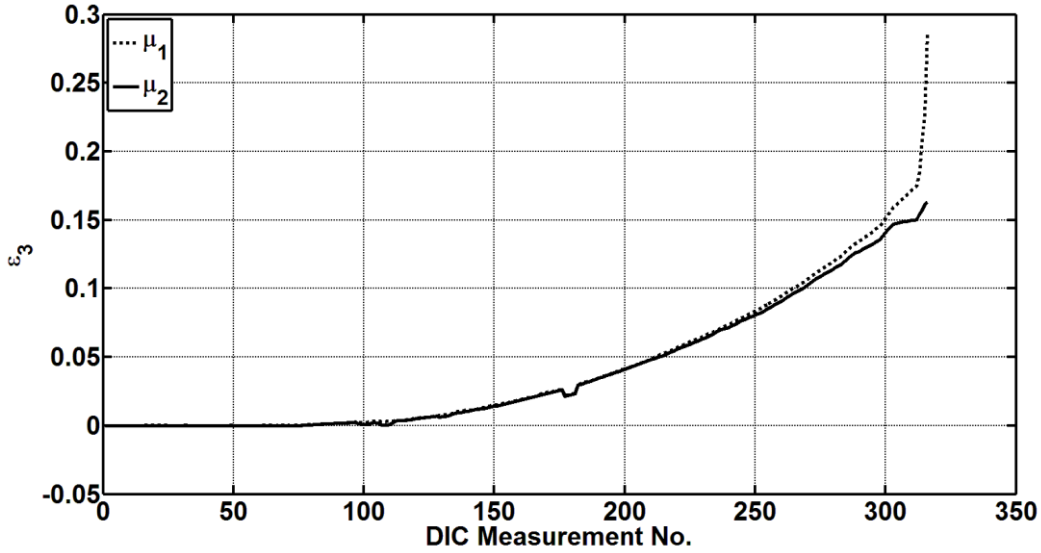

(a)

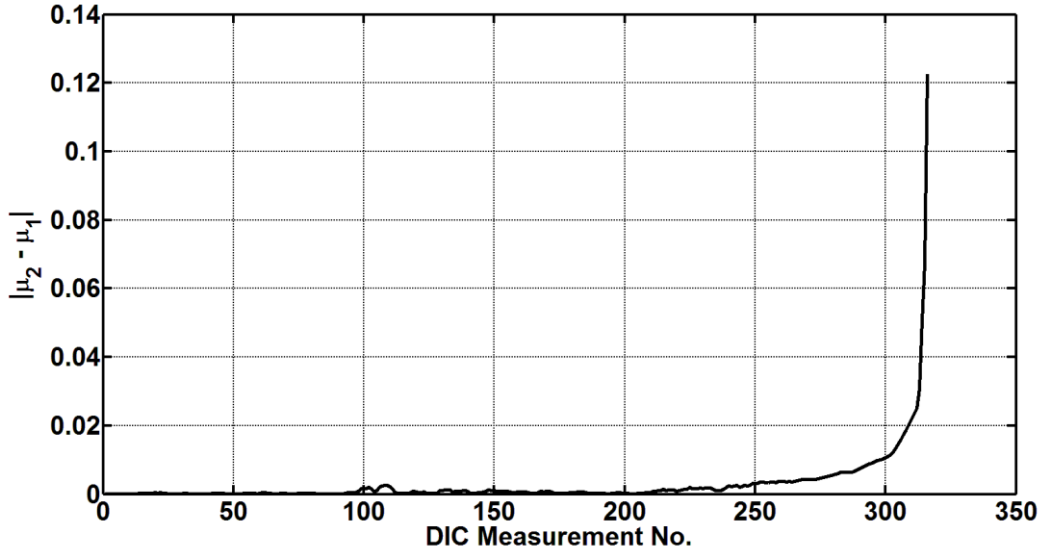

(b)

Figure 29: (a) History of $\mu_{1,2}$ of 2-component GMMs fitted to the DIC measurement history of a specimen of 1.2mm AA6111T4 undergoing plane strain deformation, and (b) the corresponding $|\mu_2 - \mu_1|$

The statistical trends observed above correlate to known strain behaviours. Firstly, the gradual separation of components from measurement 220 onwards indicates a slow tendency from evenly distributed surface strains towards two distinct strain states - characteristic of the development of a diffuse neck. Secondly, the saturation of the first component between measurements 305 and 312 is

characteristic of strain relaxation outside the neck – where the mean strain outside the neck (μ_1) increases at a slower rate than the mean strain inside the neck (μ_2). The final step change is attributable to the localised neck becoming statistically significant. As discovered in Section 3.4, a fully developed localised neck causes the second component to transition from describing both the diffuse and localised neck, to describing the localised neck alone. "Transferring" strains describing the diffuse neck between components raises the location of the first component through the inclusion of (relatively) higher strained elements, as well as raising the location of the second component. This results in increased component separation.

Previous application of the methods proposed by **Merklein et al.** (**2010**) and **Volk & Hora** (**2010**) to this plane strain specimen resulted in the time series shown in Figure 18. The time series in Figure 29b and Figure 18 exhibit similar shapes. Each is characterised by a sharp inflection point near the end of the test. The inflection point – reflecting the onset of localised necking – was previously found using a broken stick regression. Applying the same methodology to the location difference plot produces the following fitment:

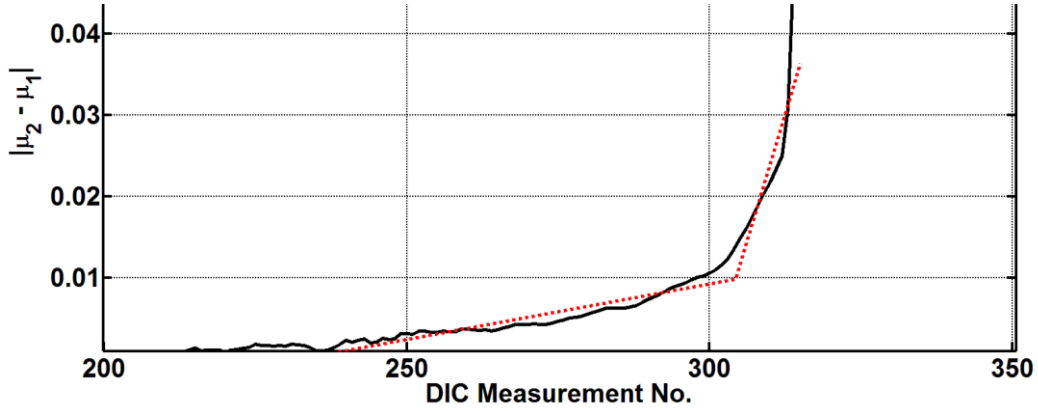

Figure 30: Broken stick regression lines applied to the $|\mu_2 - \mu_1|$ history of a specimen of 1.2mm AA6111T4 undergoing plane strain deformation

The intersection of the regression lines locates the inflection point of the GMM location curve at the 304th measurement. By comparison, the method of **Merklein et al.** (**2010**) locates the onset of localised necking at the 307th measurement and the method of **Volk & Hora** (**2010**) at the 309th measurement. These results show that the onset of localised necking determined using the new statistical method is comparable to that achievable by alternative "time dependent" methods. This proves the hypothesis that GMM parameters can be used to determine the onset of localised necking.

3.6 Representing Formability

Advancements proposed in this chapter are able to overcome obstacles which have previously prohibited accurate measurement of a localised neck at the forming limit. Overcoming these obstacles inevitably directs the research engineer towards addressing the outstanding problem - translating strains measured at the forming limit into an industrially desirable formability criterion. Constructing formability criteria requires the resolution of two problems: 1) how should strains be represented on the FLD, and 2) how should these strains be interpreted?

A simple solution is to plot strains clustered inside the neck on the FLD, and describe the measurements using linear regression. **Strano & Colosimo** (**2006**) identified that prediction intervals

calculated from a linear regression can describe the expected strain dispersion at the forming limit by an FLB. Figure 31 shows strains measured on specimens of 1.2mm AA6111T4 deformed in a Marciniak test during the benchmarking exercises. The strains are located inside the localised neck, at the onset of localised necking, using the new statistical method described earlier in this chapter. A polynomial regression (recommended by **Strano & Colosimo** (**2006**)) is fitted to the strains, with the 95% prediction intervals shown on the FLD. The linear regression model is summarised in Table 3.

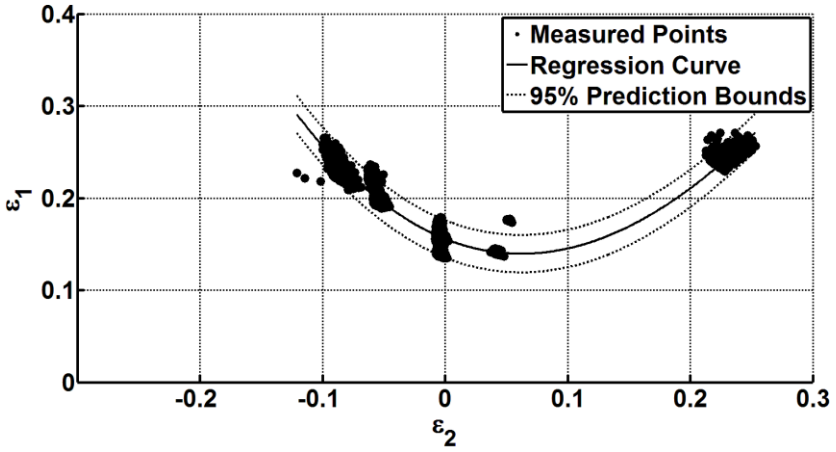

Figure 31: FLB fitted to strains of 1.2mm AA6111T4 measured at the forming limit

Regression model: $\varepsilon_1 = a{\varepsilon_2}^3 + b{\varepsilon_2}^2 + c\varepsilon_2 + d$

Coefficient	Regression Value	Upper 95% Confidence Bound	Lower 95% Confidence Bound
a	-2.378	-3.186	-1.571
b	4.521	4.383	4.659
c	-0.5356	-0.5504	-0.5208
d	0.1558	0.1553	0.1563

Table 3: Linear regression results for an FLB fitted to limit strains of 1.2mm AA6111T4

The review of the literature highlighted that whilst linear regression can account for the variability of strains at the forming limit, it is only suitable for modelling continuous data. The nature of the data reported using the GMM is non-continuous (dichotomous, in fact) - there are strains which are highly likely to neck, and there are strains which are unlikely to neck. **Strano & Colosimo** (**2006**) have shown that logistic regression is a more applicable technique for describing the transition between the two states. **Strano & Colosimo** (**2006**) explained how a Formability Map (FM) is constructed from a fitted logistic regression model. The FM provides a probabilistic representation of formability, accounting for, and accurately reflecting the inherent variation in strains at the forming limit.

Logistic regression models are fitted to strain measurements classified as “safe” (outside the necking region) or “failed” (inside the necking region). The accuracy of the fitted model relies on “safe” and “failed” strains being recognisable within experimental measurements. The methodology presented in this research resolves the subjectivity in recognising “safe” and “failed” strains by statistically distinguishing between the two states. Figure 32 shows strains measured on specimens of 1.2mm AA6111T4 at the onset of localised necking. Clustering these strains using the GMM enables the two strain states to be observed on the FLD. Formability Maps can therefore be objectively constructed from strains measured at the forming limit obtained using the GMM method.

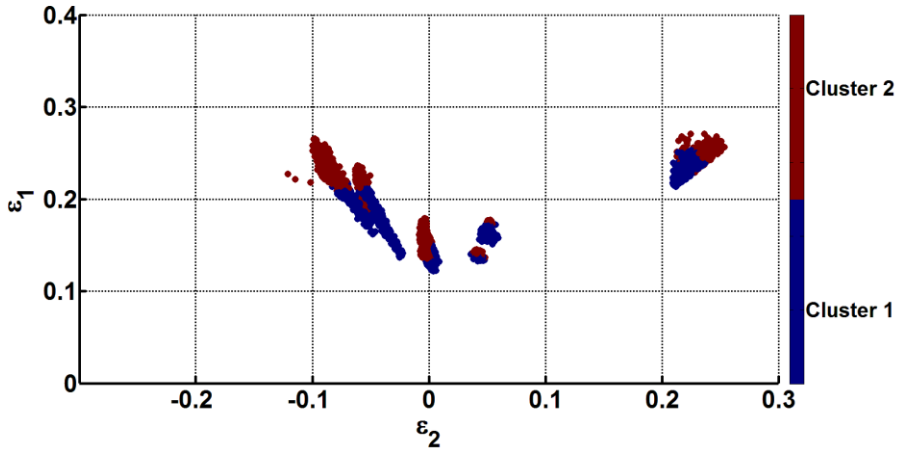

Figure 32: Strains measured on specimens of 1.2mm AA6111T4 at the onset of localised necking, showing their affinity to Cluster 1 (outside the neck) or Cluster 2 (inside the neck)

Each material benchmarked in Section 3.1 is re-evaluated using the statistical methodology developed in this chapter. 2-component GMMs are fitted to the DIC strain history of each tested specimen, with the onset of necking determined from the rate of separation of the two components. Once strains at the forming limit are identified and clustered according to the condition in Eq. 33, the FLDs are populated with clustered strains as per Figure 32.

To perform logistic regression, a suitable prediction variable structure must be identified. **Strano & Colosimo** (**2006**) determined a suitable variable structure by performing a trial and error study. Logistic regression models with different prediction structures were fitted to the data, with each model reporting the deviance (goodness of fit of the model) and the p-values (significance of each predictor variable). The optimal prediction variable structure was selected as the model which minimised the deviance using the minimum number of variables (the Parsimony principle). A trial and error study was conducted in this research, where it was found that a second-order polynomial function, as described by Eq. 34, best fits the strains obtained in the tests:

$$ln\left(\frac{P_1}{1-P_1}\right) = a\varepsilon_1^2 + b\varepsilon_2^2 + c\epsilon_1 + d\varepsilon_2 + e \qquad \textit{Eq. 34}$$

Using this structure, a logistic regression model is fitted to the clustered data obtained for each of the tested materials using the MATLAB statistical toolbox. The contours of the Formability Map are calculated using Eq. 17, and plotted on the FLD. Finally, the FMs are benchmarked against FLCs previously calculated by the standardised and “time-dependent” methods.

3.6.1 Results

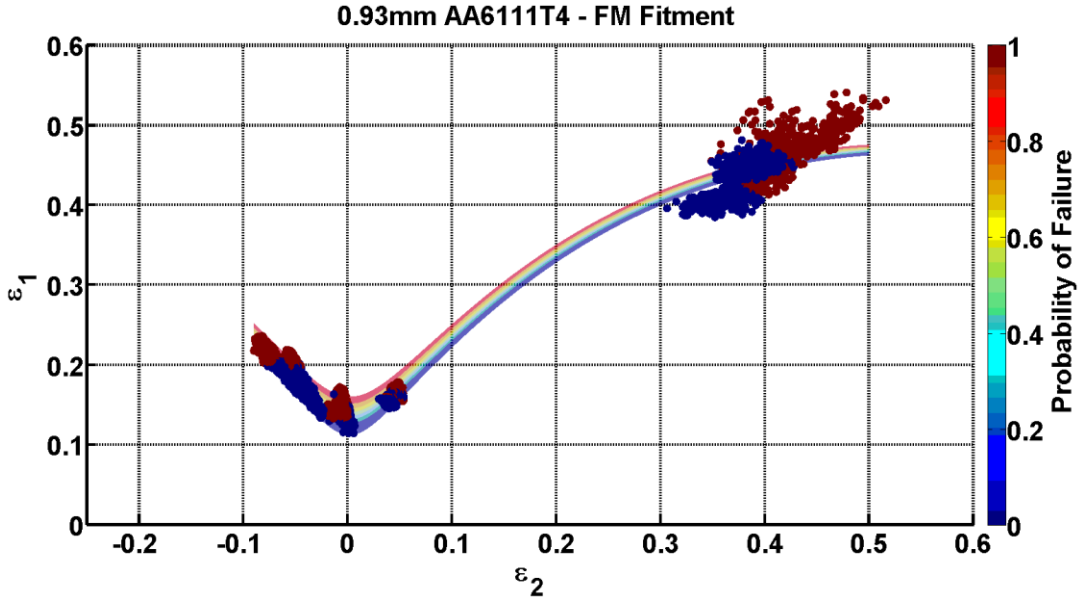

Figure 33: A FM of 0.93mm AA6111T4 fitted to GMM-clustered DIC measurements

Variable	Coefficient	Regression Value	Standard Error	p-Value	Deviance
ε_1^2	*a*	-741.9899	6.8467	0	**9.98 x10^4**
ε_2^2	*b*	502.4183	5.4216	0	
ε_1	*c*	9.9613	0.3236	0	
ε_2	*d*	833.0662	7.5189	0	
Constant	*e*	-12.4184	0.1130	0	

Table 4: Optimised logistic regression model fitted to DIC measurements of 0.93mm AA6111T4

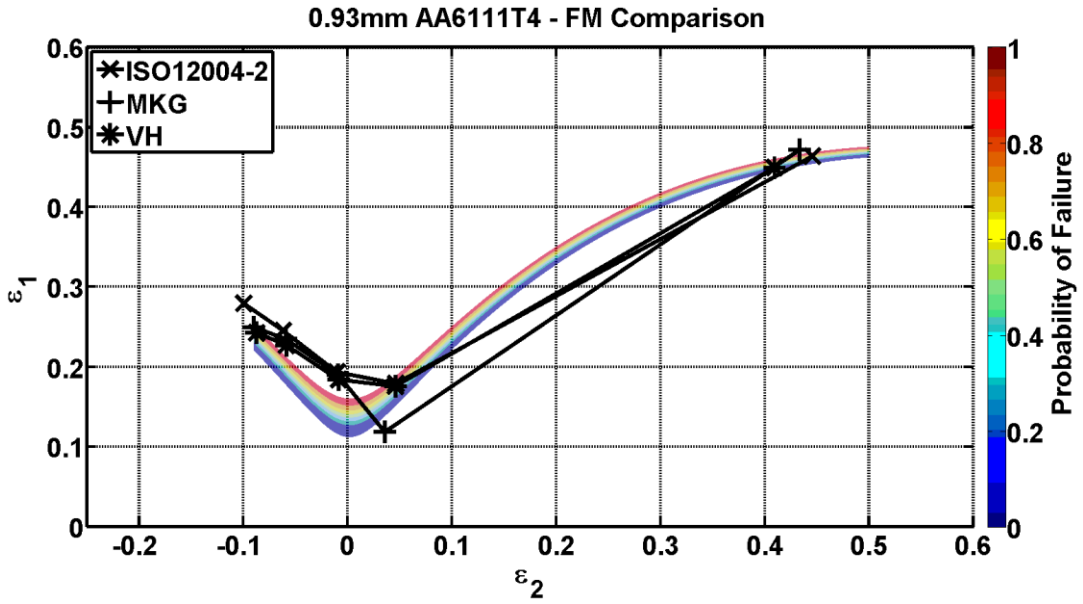

Figure 34: A FM of 0.93mm AA6111T4 compared to FLCs calculated by established methods

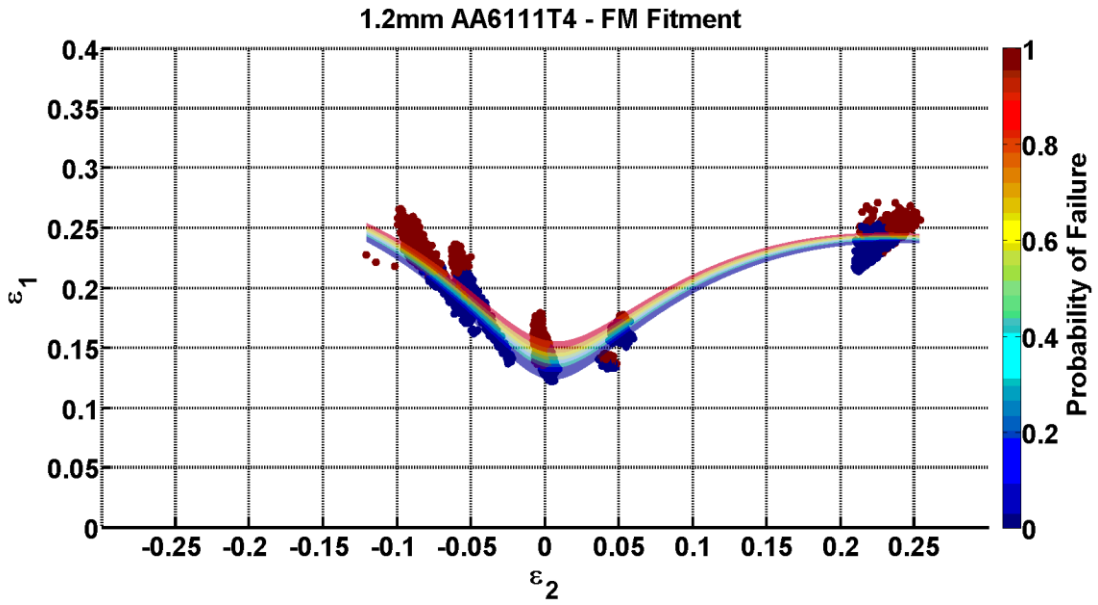

Figure 35: A FM of 1.2mm AA6111T4 fitted to GMM-clustered DIC measurements

Variable	Coefficient	Regression Value	Standard Error	p-Value	Deviance
ε_1^2	*a*	-1.4531 x10^3	29.8248	0	**3.15 x10^3**
ε_2^2	*b*	2.1043 x10^3	51.3340	0	
ε_1	*c*	0.0344 x10^3	1.3255	0	
ε_2	*d*	1.5971 x10^3	30.6312	0	
Constant	*e*	-0.0202 x10^3	0.2429	0	

Table 5: Optimised logistic regression model fitted to DIC measurements of 1.2mm AA6111T4

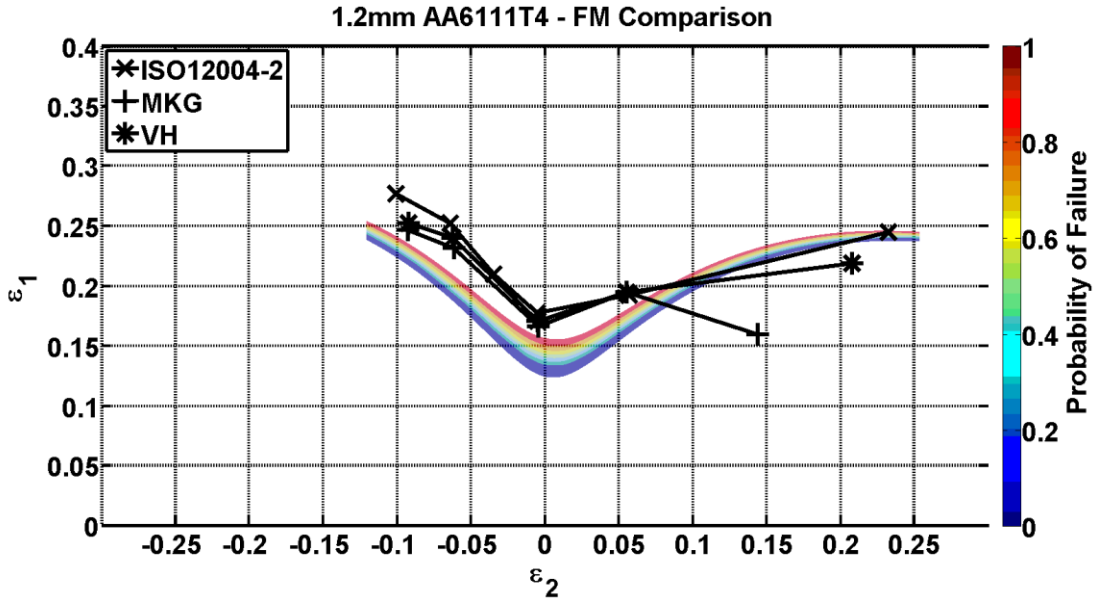

Figure 36: A FM of 1.2mm AA6111T4 compared to FLCs calculated by established methods

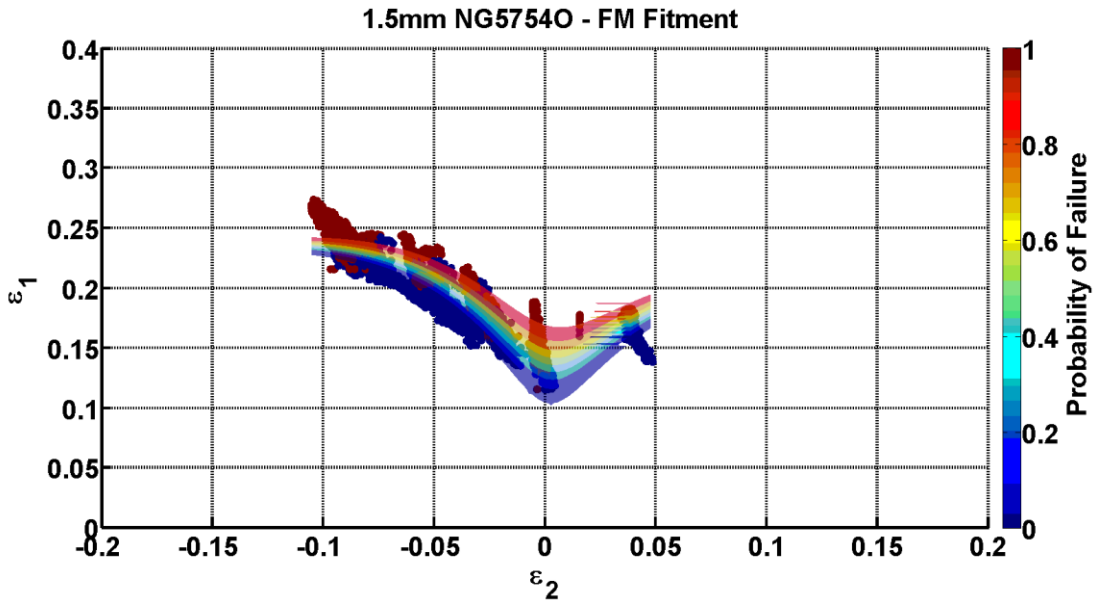

Figure 37: A FM of 1.5mm NG5754O fitted to GMM-clustered DIC measurements

Variable	Coefficient	Regression Value	Standard Error	p-Value	Deviance
ε_1^2	*a*	-2.8305 x10^3	95.9349	0	**4.64 x10^3**
ε_2^2	*b*	5.4263 x10^3	195.8943	0	
ε_1	*c*	0.0408 x10^3	2.3760	0	
ε_2	*d*	2.9121 x10^3	97.7421	0	
Constant	*e*	-0.0112 x10^3	0.4538	0	

Table 6: Optimised logistic regression model fitted to DIC measurements of 1.5mm NG5754O

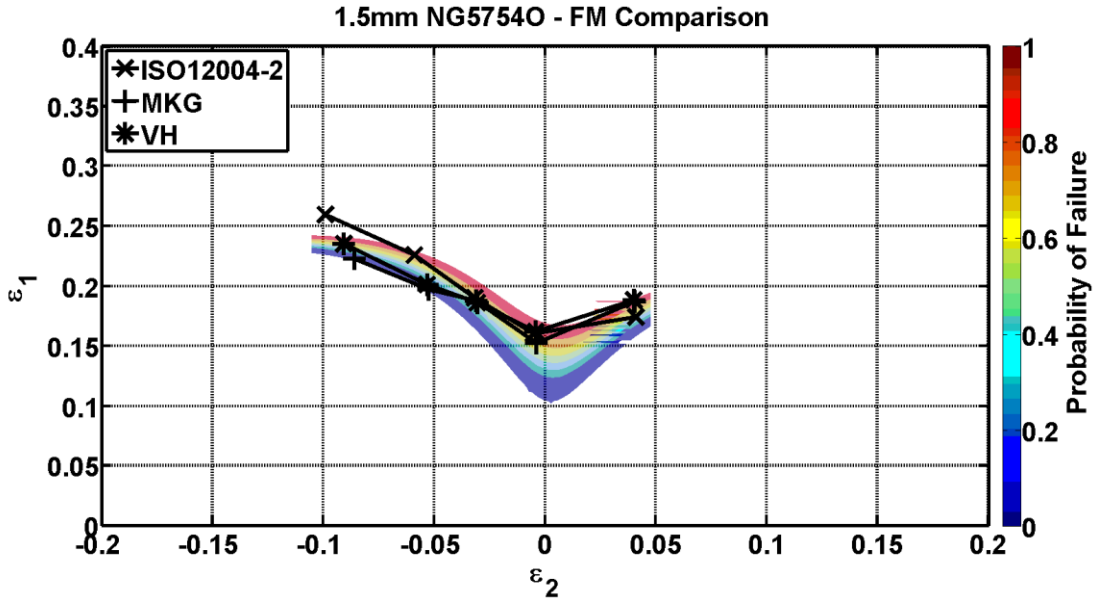

Figure 38: A FM of 1.5mm NG5754O compared to FLCs calculated by established methods

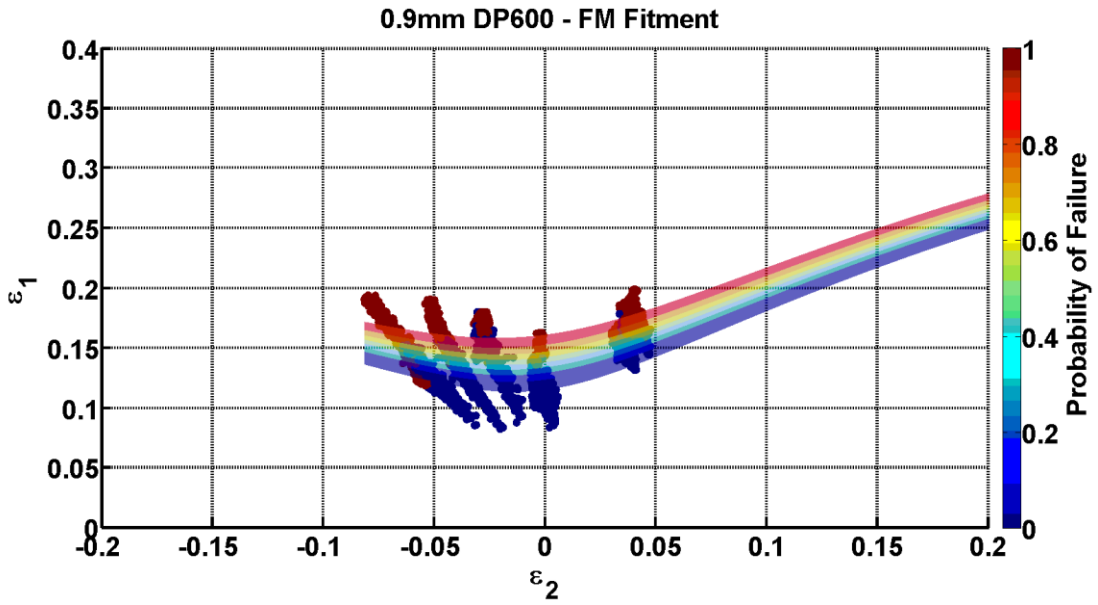

Figure 39: A FM of 0.9mm DP600 fitted to GMM-clustered DIC measurements

Variable	Coefficient	Regression Value	Standard Error	p-Value	Deviance
ε_1^2	*a*	-362.6514	14.9612	0	**2.72 x10^3**
ε_2^2	*b*	410.9325	23.0650	0	
ε_1	*c*	-36.1552	1.1535	0	
ε_2	*d*	473.3308	15.5562	0	
Constant	*e*	-14.9711	0.1646	0	

Table 7: Optimised logistic regression model fitted to DIC measurements of 0.9mm DP600

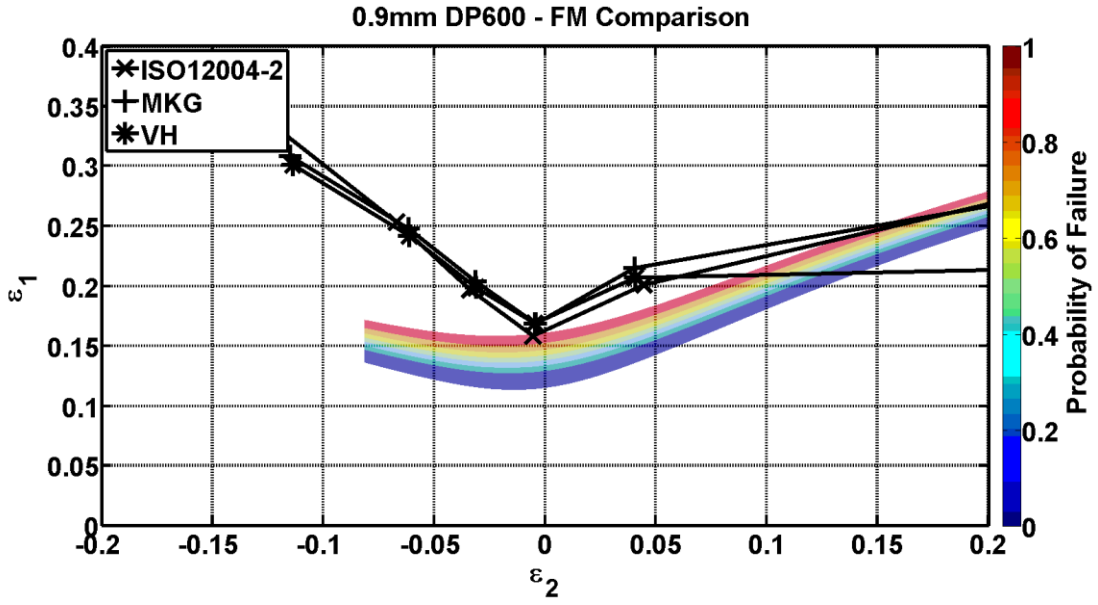

Figure 40: A FM of 0.9mm DP600 compared to FLCs calculated by established methods

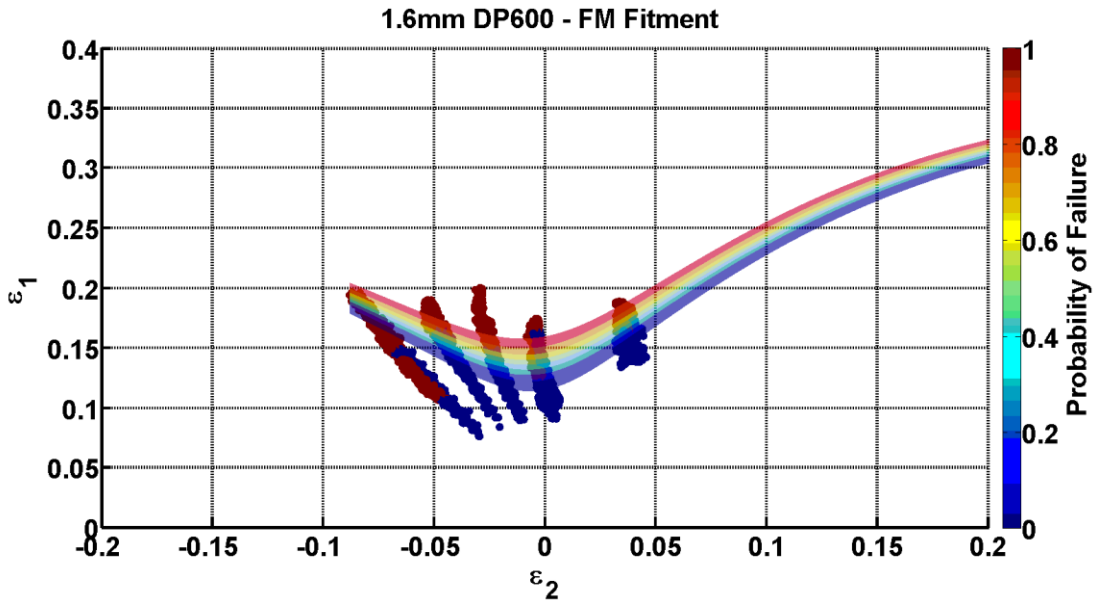

Figure 41: A FM of 1.6mm DP600 fitted to GMM-clustered DIC measurements

Variable	Coefficient	Regression Value	Standard Error	p-Value	Deviance
ε_1^2	*a*	-783.2766	15.1988	0	**5.03 x10^4**
ε_2^2	*b*	881.0639	21.8903	0	
ε_1	*c*	-34.3747	1.0707	0	
ε_2	*d*	881.7548	15.4024	0	
Constant	*e*	-13.5174	0.1072	0	

Table 8: Optimised logistic regression model fitted to DIC measurements of 1.6mm DP600

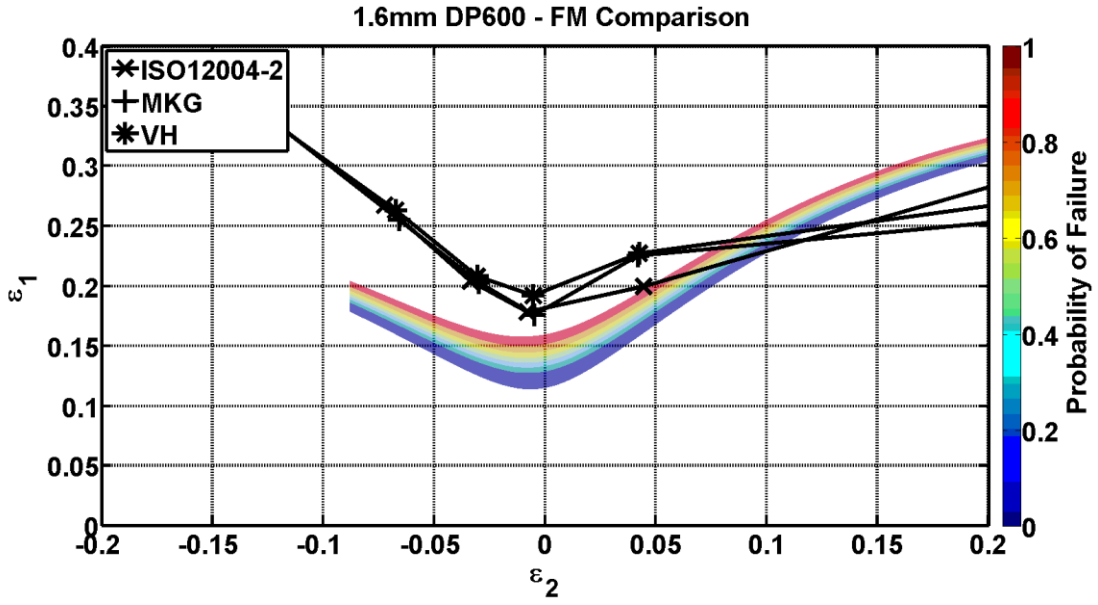

Figure 42: A FM of 1.6mm DP600 compared to FLCs calculated by established methods

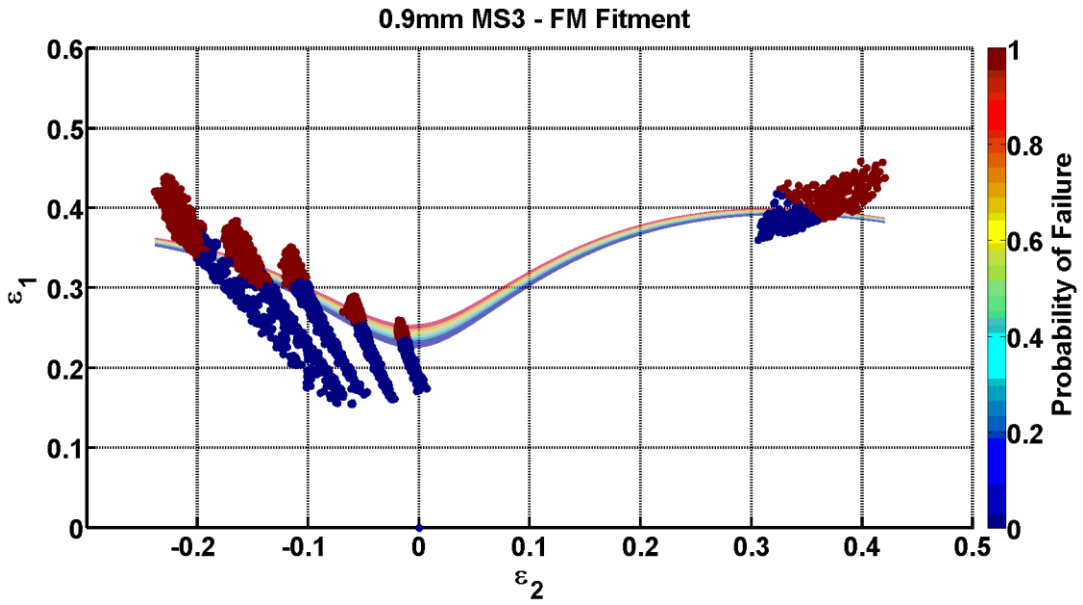

Figure 43: A FM of 0.9mm MS3 fitted to GMM-clustered DIC measurements

Variable	Coefficient	Regression Value	Standard Error	p-Value	Deviance
ε_1^2	*a*	-1.499 x10^3	91.5580	0	**1.92 x10^3**
ε_2^2	*b*	1.505 x10^3	108.0523	0	
ε_1	*c*	-0.0226 x10^3	3.7983	0	
ε_2	*d*	1.6474 x10^3	93.0075	0	
Constant	*e*	-0.0356 x10^3	1.4135	0	

Table 9: Optimised logistic regression model fitted to DIC measurements of 0.93mm MS3

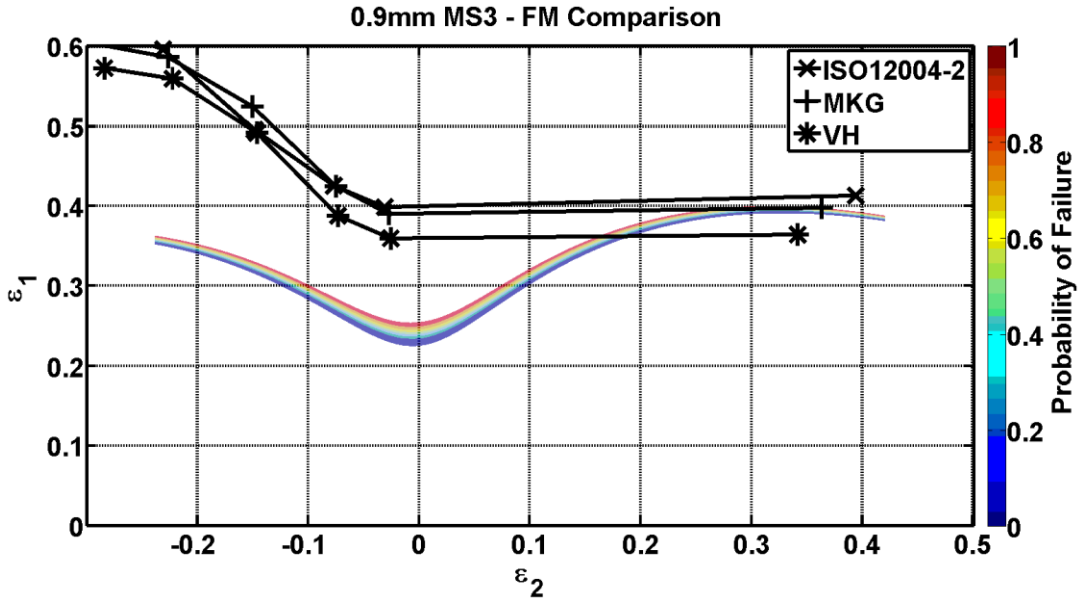

Figure 44: A FM of 0.9mm MS3 compared to FLCs calculated by established methods

The geometries of the FMs calculated using logistic regression have similar geometries to the FLCs. The lowest amount of formability still occurs at plane strain, with formability being higher in uniaxial tension and equibiaxial tension.

The transition between P(Failure)=0 and P(Failure)=1 varies across materials and strain paths. The FM narrows where there is a clear separation between the safe and failed strains, and broadens in regions where the two states overlap. The narrowest FM is seen for MS3, which has a width of approximately 0.025 true major strain in plane strain. NG5754 exhibits the widest FM, spanning approximately 0.075 true major strain in plane strain.

For aluminium alloys deformed under uniaxial tension and plane strain conditions, the contours of P(Failure)=0.9 are most closely aligned to the FLCs. Under biaxial tension the shapes of the Formability Maps exhibit greater curvature than the interpolated FLCs. This characteristic is attributable to the prediction variables used in the logistic regression models.

Greater discrepancy is seen between the Formability Maps and the FLCs calculated for steels. Under uniaxial and plane strain conditions, the contour lines of P(Failure)=0.9 are consistently lower than the FLCs. The most extreme example is in MS3 where the Formability Map is ≈0.2 true major strain lower than the FLCs under uniaxial tension conditions. An explanation for this discrepancy is found from the rate of separation of GMMs fitted to a uniaxial sample of MS3. Figure 45 shows that the rate of separation of the GMM components does not display as sharp an inflection as that exhibited by 1.2mm AA6111T4 (Figure 29b). This implies that the development of a localised neck is more gradual in MS3 than in AA6111T4. Consequently, the onset of localised necking is less prominent in MS3. The large discrepancy between the FM and the benchmark FLCs suggests that the inflection point found in Figure 45 is more likely to correspond to the onset of diffuse necking than localised necking, resulting in a lower perceived forming limit.

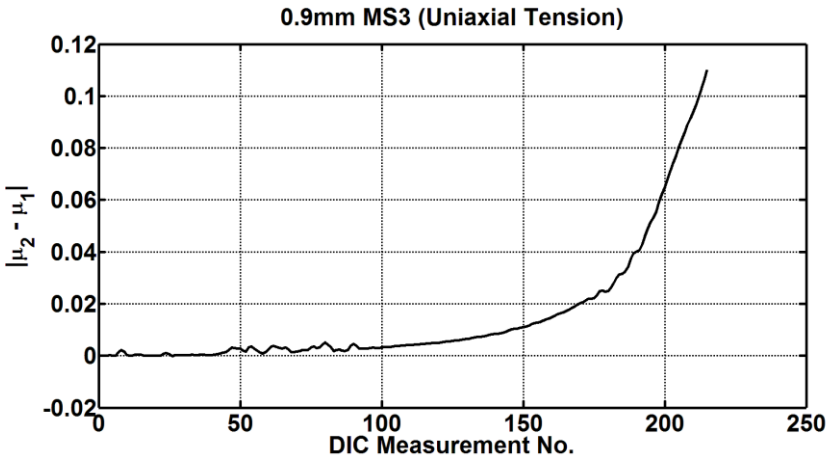

Figure 45: Rate of separation of GMM components fitted to the strain history of a sample of 0.9mm MS3 subject to uniaxial tension deformation

The FMs calculated in this section confirm **Strano & Colosimo's** (**2006**) conclusion that the risk of failure can be obtained by logistic regression. The application of GMM to DIC strain measurements improves the previously subjective process of classifying strains as safe and failed by using statistical clustering to distinguish between strain measurements. Combining the GMM methodology with logistic regression has resulted in a fully impartial method for determining and representing formability. The resulting FM provides forming engineers with a quantifiable risk of failure, enabling engineers to more precisely quantify the feasibility of a stamped panel.

3.7 CONCLUSIONS

Central to the innovations created in this chapter is the recognition that the Zone of Evaluation of a Marciniak specimen is not a homogeneous entity. By treating strain measurements heterogeneously, it is shown that the strain topography exhibits statistically significant characteristics. Modelling these statistical characteristics enables heterogeneous behaviour to be quantified and assists the identification of the localised neck, thereby fulfilling the research objective. Consequently, one of the main sources of limit strain scatter which typifies formability tests is better understood and more precisely characterised.

- Heterogeneous strain characteristics evolve with increasing plastic deformation. Describing strain topography statistically demonstrates that increasing plastic deformation affects the central tendency, dispersion, and shape of the strain distribution
- PDFs of strain measurements are unimodal during early plastic deformation. During later deformation PDFs tend towards bimodality for specimens exhibiting a localised neck before fracture
- Plastic strain PDFs are modelled by 2-component Gaussian Mixture Models. During localised necking the first component of a fitted 2-component GMM characterises strain measurements made outside the localised neck, and the second component characterises strain measurements made inside the localised neck.
- The GMM can be used to cluster strain measurements during necking. This enables the strains responsible for bimodality to be identified within the DIC measurement distribution, and locate the neck on the specimen
- The onset of localised necking is determined from the rate of separation of the GMM components, when the neck develops over a short period of time. Further work is required to definitively identify the onset of localised necking for materials which exhibit more gradual necking, such as MS3
- Logistic regression is used to characterise clustered strains at the forming limit. Creating a Formability Map from the regression model results in a contour map showing the probability of failure, where failure is defined as a strain inside the neck, at the onset of localised necking

4 USING THE FORMABILITY MAP TO PERFORM A DESIGN FEASIBILITY STUDY

The research documented in this innovation report has led to the development of a new methodology for determining and representing formability. The motivation behind developing this methodology was to provide the industrial sponsor with a more accurate and precise tool for conducting design feasibility studies. Feasibility studies are used to interpret the results of stamping simulations and predict defects which could arise during production. Accurately quantifying the risk of a defect occurring is important to the Stamping Engineering department since their responsibility is to minimise cost and manufacture safe, high quality panels. The conventional practice for determining the risk of failure is to compare a simulated panel's surface strains to an FLC. In Chapter 1 it was demonstrated that combining the FLC with a pre-determined safety margin partitions the FLD into three areas: a safe region (area below the safety margin); a marginal region (area between the safety margin and FLC); and a failed region (area above the FLC). It was further highlighted that the safety margin causes ambiguity in determining the risk of failure for strains which fall inside the marginal region. This was attributed to the fact that the risks posed to formability, purportedly mitigated by the safety margin, have not been quantified: the risk that the formability criterion is incorrectly positioned due to the scatter which typifies ISO-standard limit strain measurements; the risk that mechanical property variation causes formability variation between blanks; or the risk that conditions imposed by the stamping operation cause premature failure.

The innovative research performed in this Engineering Doctorate has focussed on addressing the risk that comes with incorrectly positioning the FLC within scattered limit strains. By employing a statistical methodology to measure the forming limit, a probabilistic (rather than deterministic) representation of formability has been realised. The Formability Map (FM) is objectively positioned using a regression model, based on the statistical character of strains at the forming limit. Furthermore, the ambiguity caused by interpreting the risk of failure from strains' proximity to an FLC is overcome by the precise measure of the risk of failure provided by the Formability Map.

To exemplify the improved utility of the Formability Map over the conventional FLC, and to exploit the innovative solution created in this research, the feasibility of a current production panel will be assessed using an FLC and a FM. The results will be correlated to the performance of a physical panel.

4.1 METHOD

A rear fender outer used in a current production vehicle is considered. This panel was chosen because the size and value of the panel make defects costly. Production records show that 13% of the panels manufactured (at the time of writing) exhibit one or more defects which require manual rework, or exhibit defects which are sufficiently severe to scrap the panel entirely. At the current rate of production, it is estimated that the cost of reworking and scrapping these panels over the lifetime of the vehicle will be approximately £2m. Figure 46 highlights the locations of these defects on the panel. The majority of defects appear in the drawn shell during the first stamping operation. Two of the defects (marked 4 and 7 on Figure 46) are splits, which suggests that the forming limit has been exceeded in these areas.

The fender is manufactured from AA6111T4. Using a historic stamping simulation of the drawing operation, which was performed by a Jaguar Land Rover engineer, two feasibility studies of the drawn shell are conducted. These are performed by comparing the simulation results to two

different formability criteria. The first assessment is made against an FLC produced by the material supplier some years before the publication of the ISO12004-2 test standard. The precise details of the test procedure are unknown but are believed to broadly follow the standardised method. A safety margin is positioned 0.08 (true major strain) below the curve, as is mandated by Jaguar Land Rover. This mirrors the original feasibility assessment which was performed during the panel's development. The second assessment is made against the equivalent Formability Map that was developed in this research, shown in Figure 33.

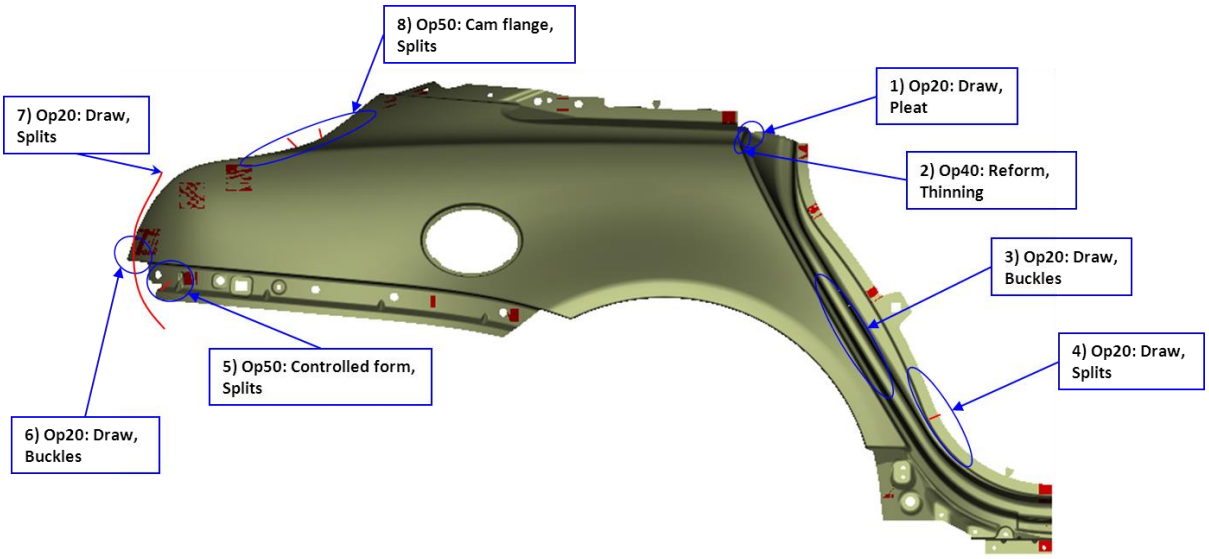

Figure 46: Defects recorded in the production of a rear fender outer

4.2 RESULTS

The results of each assessment are shown in Figure 47 and Figure 48. Figure 47a shows the predicted strain in the panel with respect to the FLC and safety margin. Figure 48a makes the same comparison to the Formability Map and additionally highlights each strain's probability of failure. Figure 47b shows the location of the safe/marginal/failed strain classifications made against the FLC on the drawn shell. Similarly, Figure 48b highlights the locations and probabilities to failure expected in the stamping operation.

When compared to the deterministic FLC (Figure 47), the strains predicted by the simulation lie in three regions of the FLD. The majority of the elements in the model contain strains that lie in the safe region (area below the safety margin) and are considered robust to failure. Around 3% of strains lie in the marginal region (area between the safety margin and FLC) and are considered to have a risk to failure. The risk of failure is not quantified within this region.

When the strains are compared to the FM (Figure 48), the strains are represented as a probability to failure from 0 to 1. When the probability of failure numbers are extracted from Figure 48, it shows that approximately 96% of the elements in the panel have a strain of less than 0.1 chance of failure. The elements with the greatest probability to failure lie in the plane strain path. Approximately 0.8% of the elements in the model are likely to fail (having a greater than 0.5 chance of failure), with 0.2% of the elements having a greater than 0.8 chance of failure.

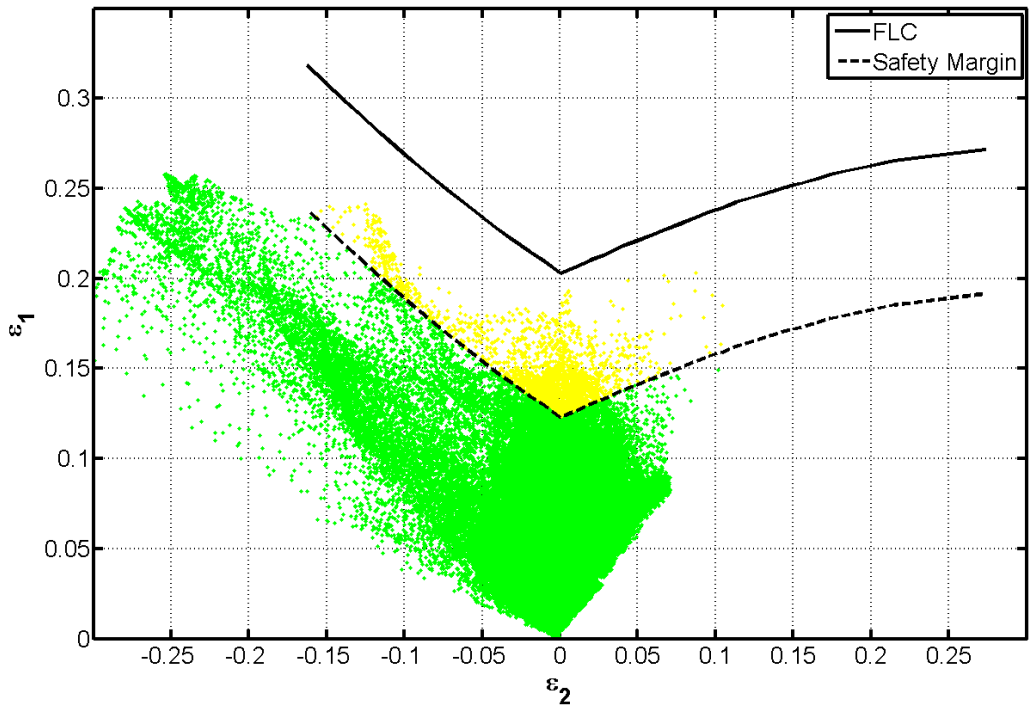

(a)

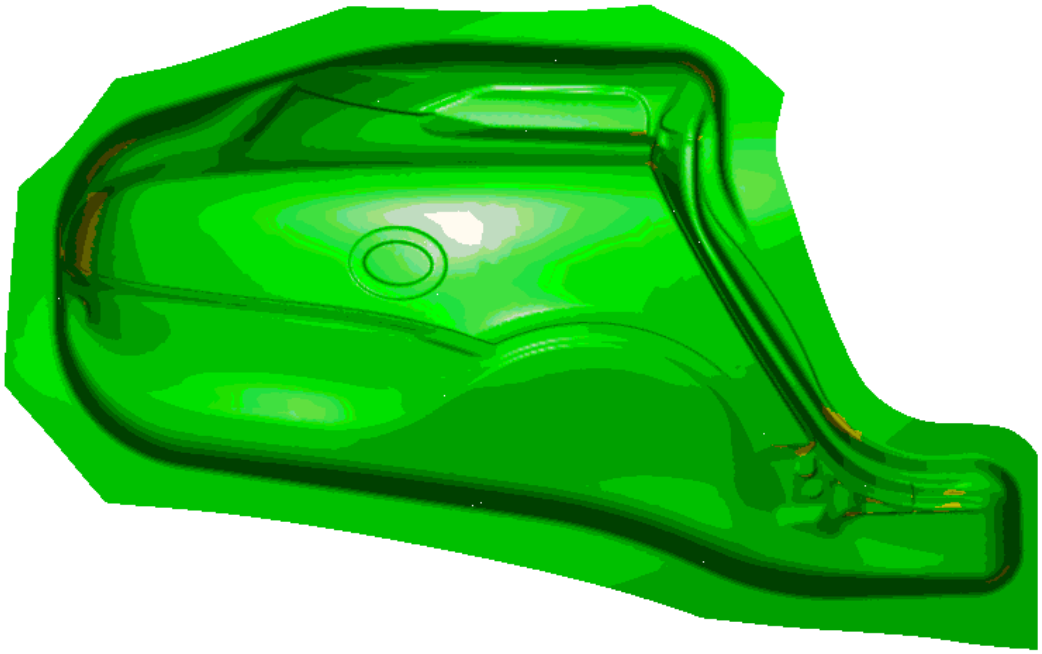

(b)

Figure 47: (a) Feasibility assessment made using the original FLC, and (b) results superimposed on the simulated panel

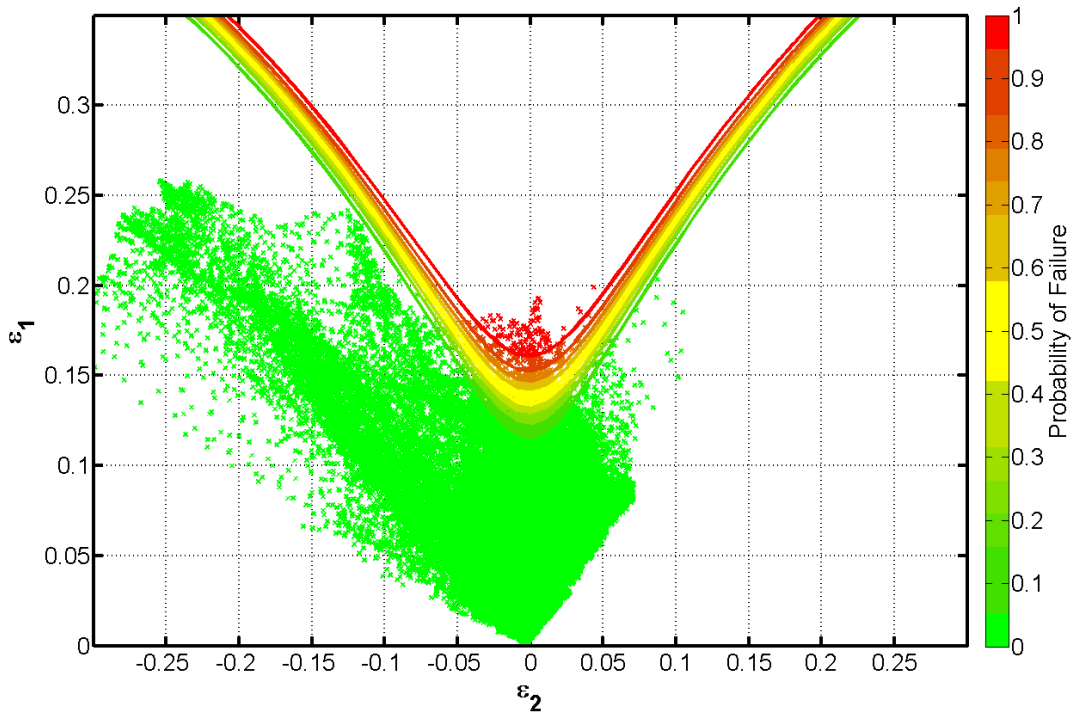

(a)

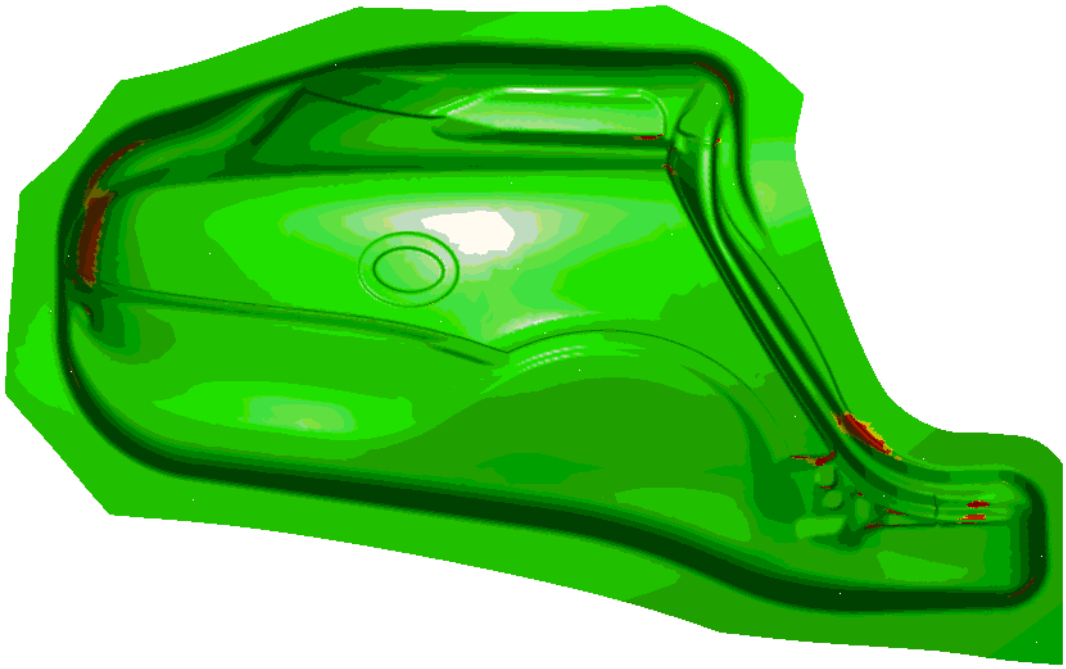

(b)

Figure 48: (a) Feasibility assessment made using the Formability Map, and (b) results superimposed on the simulated panel

4.3 DISCUSSION

The two studies predict there is a risk of a defect occurring in particular areas of the drawn shell. The results of the simulation interpreted in Figure 47b and Figure 48b show that areas of risk identified by the two methods are in broadly the same locations. The first area is located in the lower right hand corner of the panel, adjacent to the door aperture. The second area is located on the left hand side of the panel, adjacent to the recess for the rear taillight. These two areas emulate the locations of the splits seen in production, highlighted 4 and 7 in Figure 46. However, whilst the two formability assessments are aligned with respect to identifying the areas of risk, the predicted significance of the risks varies between the two techniques.

The FLC assessment highlighted areas of the panel which are “marginal”, signifying that there is a risk a defect will occur in these areas. Obtaining a precise measure of the risk of failure for these areas is not possible using the FLC technique. Since it is not possible to quantify risk using an FLC, Jaguar Land Rover’s engineers used their engineering judgement to assess the likely risk during manufacturing. They came to the conclusion that the risk was acceptably low and the panel was declared feasible. The subsequent problems in manufacturing the panel show the limitations of this judgement, particularly when assessing a complex panel.

The Formability Map removes the ambiguity of risk that is associated with a safety margin and shows that the design of the rear fender outer has a severe risk of failure. The “marginal” elements which were considered to have an acceptably low risk of failure in the first assessment have a high risk of failure when compared to the Formability Map. 0.2% of the elements on the panel have a greater than 0.8 chance of failure, and is a closer reflection of the problems seen on the shop floor. It is therefore highly likely that a defect will occur in these areas. When inspecting the locations of these elements on the simulated panel in Figure 48b, it can be seen that these areas correlate to the splits that have manifested in production, shown in areas 4 and 7 of Figure 46.

The comparison between the FLC and FM shows the utility of quantifying the risk to failure, particularly in the assessment of large, complex panels. Since these panels tend to have high piece, tooling, and development costs, the FM will reduce the commercial risk associated with these panels, and reduce the likelihood of corrective actions required to rectify a suboptimal process.

4.3.1 The Cost of Improving the Performance of the Rear Fender Outer Toolset

The FLC-based feasibility assessment has led to a large proportion of panels that have either undergone corrective action or been scrapped. The design of the draw punch is shown in Figure 49. The Formability Map highlights areas A and B on the punch as being responsible for the high-risk strains in the panel. It can be seen that both A and B contain features with sharp radii. The sharp radius identified in A is used to ensure the mating surface between the fender and the rear door is smooth, so that the rear door can open and close without hindrance. The sharp radius identified in B is used to form an aesthetic styling feature near the rear light cluster.

The likelihood of defects appearing on the drawn shell can be reduced by re-designing the features of the draw die identified by the Formability Map. Reducing the likelihood of failure would also decrease the projected cost of reworking and scrapping panels over the lifecycle of the vehicle. One design change which could be implemented is to increase the radius of the tool in these areas. Increasing the radii reduces the physical constraint on the panel, thereby allowing the material greater freedom to flow during the draw. Increasing the radii also decreases the through thickness strain gradient and reduces straining on the outer surface, thereby reducing the likelihood of initiating a neck or fracture on the outer surface.

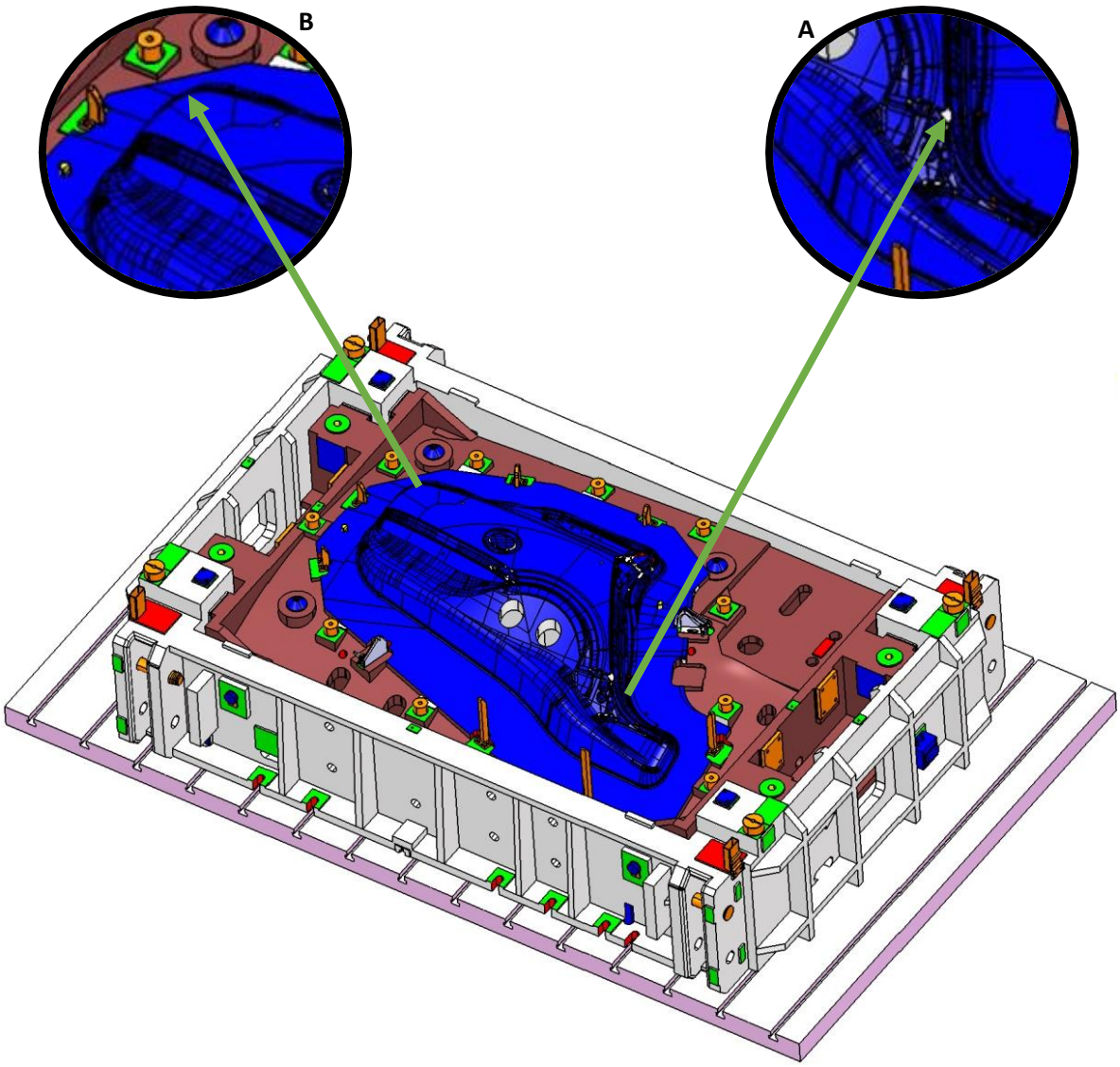

Figure 49: Draw die used to manufacture the rear fender outer, highlighting features responsible for splits in the drawn shell

Discussions with Jaguar Land Rover's engineers reveal that the feasibility of this design change would be evaluated using three different solutions. The first solution is to re-design the existing tooling, and modify the current draw die in the areas which cause the defects. Implementing this solution requires the existing die to be re-cut to a new design, and is often the cheapest solution available. If a safe panel cannot be obtained from a re-design of the existing die, a replacement draw die will be designed. Designing, commissioning, and manufacturing a new draw die is more expensive than altering an existing die. Finally, if it is concluded that a defect-free panel cannot be manufactured to the existing panel design, the outstanding solution is to alter the design and/or styling of the panel itself. Implementing this solution requires an entirely new suite of tools (five tools for the rear fender outer) to be developed, which is occasionally done as part of a vehicle facelift. This solution is the most expensive of the three. Clearly, the type of solution adopted will dictate the level of cost which can be avoided. The cost of each solution and the resulting reduction in process cost, which was estimated by a Jaguar Land Rover engineer, is shown in Table 10.

Solution	Estimated Cost of Solution	Reduction in Additional Process Cost
Major tooling re-cut and re-commission	£350,000	£1,650,000
Manufacture and commission a new draw die	£500,000	£1,500,000
Panel change as part of a facelift: A completely new tool suite is required	£1,400,000	£600,000

Table 10: Estimated costs to change the die designs of the rear fender outer

It must be recognised that the impact of the proposed design change to the rear fender outer will be wider than simply reducing the probability of failure. Firstly, in region A, increasing the radius along the periphery of the panel will change the shape of the door aperture. This could affect the ability of the current door panel to close correctly. Secondly, the die features in region B are responsible for a styled surface which is in the direct line of sight of the customer. Changing the die features in this area will alter the aesthetics in this region the vehicle. A radius change to region B could result in a misalignment of a styling feature which traverses across neighbouring panels (the bootlid and rear bumper). To accommodate a re-design of the rear fender outer, a complimentary re-design of the rear door panels (both skin and structural), the bootlid, and the rear bumper may have to be performed. The implications of performing the suggested modification to the two areas identified by the Formability Map will most likely require a panel re-design. It is therefore likely that the most viable solution to solve the splits which occur in the drawn shell is to perform a panel design change as part of a vehicle facelift.

4.3.2 Further Comments on the Application of a Formability Map to an Industrial Panel

The analysis of the industrial panel described in this chapter has shown that the probabilistic measure of formability developed in this research provides the level of precision required to a) identify and quantify regions of a panel which are likely to form a defect; and b) assist in making design decisions to rectify an existing defect. However, despite the improved precision offered by the Formability Map over the FLC, the Formability Map retains certain limitations which preclude a fully accurate assessment of formability.

The three risks to formability that have been identified are the risk that the formability criterion is incorrectly positioned; the risk that mechanical property variation causes formability variation between blanks; and the risk that conditions imposed by the stamping operation cause premature failure. The objective positioning and statistical nature of the Formability Map is able to describe the risk associated with the positioning the criterion. However, no provision has been made to account for the non-linear strain paths which arise in an industrial stamping operation.

An example of a typical non-linear strain path on the rear fender outer is shown in Figure 50. Figure 50b shows that the path taken by the element highlighted in Figure 50a begins in uniaxial tension, before changing direction halfway through the draw and continuing along a biaxial strain path. This path change has consequences for the level of formability achievable by this element, and the ability to measure the element's formability using the Formability Map. Research published by **Graf & Hosford (1994)** demonstrated that the pre-straining in uniaxial tension raises the forming limits for subsequent biaxial tension, when the direction of the principal strains is preserved. Therefore, it is expected that the actual formability achievable by the element identified in Figure 50a will be higher than that prescribed by the Formability Map.

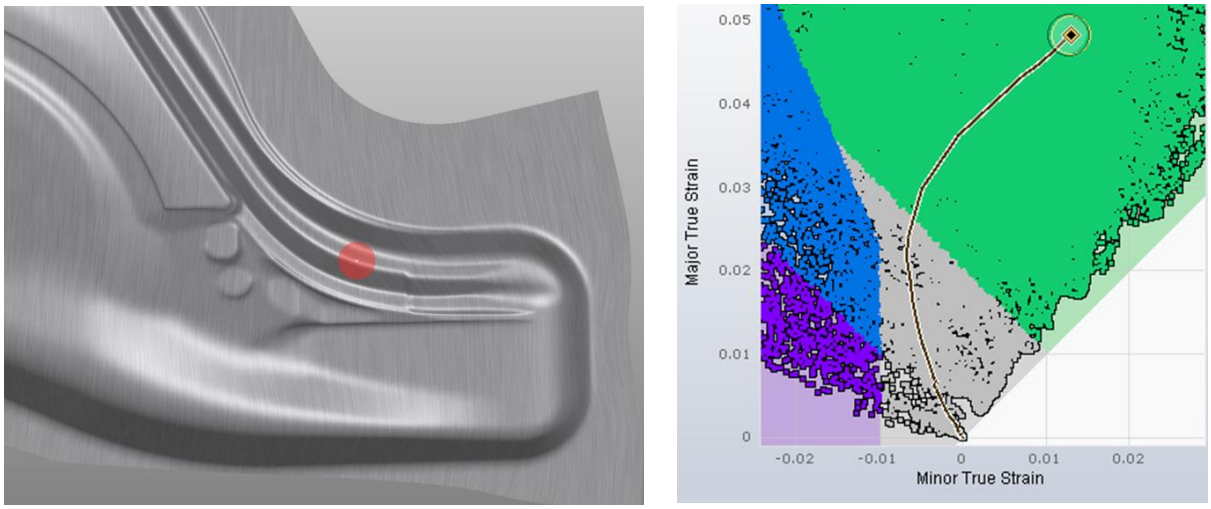

(a) *(b)*

Figure 50: Example of a nonlinear strain path) taken by an element in the drawing operation of the rear fender outer

Unique strain paths taken by each element in the simulated panel draws attention to the ability of the "initial-strain" based Formability Map to accurately describe the formability of an industrial panel. Although not measured in this research, it is realistic to expect that the shape and location of the Formability Map is as sensitive to strain path changes as the FLC. It is therefore unlikely that a single "initial-strain" based Formability Map is an accurate technique for assessing the risk of failure of an entire panel. However, the central argument of this work, that failure is better described statistically, still holds true when deformation takes place along non-linear paths because plastic deformation in polycrystal metals is not uniform. Further research is required to adapt the characteristics of the Formability Map to the path taken by each element, similar to that proposed by **Volk et al.** (**2012**).

4.4 CONCLUSIONS

- The statistical nature of the Formability Map provides engineers with the precise measure of the risk of failure that is missing from feasibility studies conducted using the FLC
- Increased precision provided by the Formability Map enables engineers to identify areas of a simulated panel which are likely to fail, and help prioritise areas of rework on the tool
- Whilst the Formability Map provides a precise measure of the risk of failure, it is recognised that to fulfil industrial requirements the accuracy of this assessment method needs further improvement. In particular, the accuracy of risk assessments made using the Formability Map should be improved to account for the non-proportional deformation conditions that occur in an industrial panel

5 PREDICTING STRAIN BEHAVIOUR AT THE FORMING LIMIT USING THE MARCINIAK-KUCZYNSKI MODEL

Research presented in this report has shown that surface heterogeneity is an inherent feature of plastic deformation, and at the macroscopic scale, it can be characterised using a GMM. In Chapter 2 it was suggested that one source of surface heterogeneity is microstructural deformation which fails to homogenise at the macroscopic scale. Heterogeneous deformation at the micro-scale is a consequence of metals' inherently heterogeneous structure: the anisotropy of grains; the occurrence of slip on particular slip systems; and differences in orientation between interfacing grains. These features cause micro-scale strain variation from the onset of deformation.

An outcome of this deformation is a variation in the normal displacements of grains at the sheet's surface. In turn, this produces a surface roughness. This behaviour can manifest at the macroscopic scale as "orange peel" or banding, which arises from single and collective granular distortions respectively. The review of the literature in Chapter 2 identified that the primary influencers of free surface roughening are the material's grain size, crystallographic structure; and texture.

The pertinence of surface heterogeneity to formability was discussed by **Parmar et al.** (**1977**) who hypothesised that deformation-induced surface roughening reduces the sheet's effective thickness in localised areas. Occurrence of such defects can initiate a tensile instability at lower surface strains than those predicted by classical instability analysis, thereby lowering the forming limit. **Yamaguchi et al.** (**1995**) recognised that the formability of thin sheets is particularly sensitive to this phenomenon, since thin sheets have a small number of grains across the thickness. Having observed that incipient necking initiates in the trough of the deepest surface asperity, **Yamaguchi et al.** (**1995**) proposed a new forming technique whereby the roughness developed during deformation is polished to eliminate the weak portions of the sheet. The results demonstrated that interim polishing delays the initiation of a geometric instability, and improves the formability of thin (<0.2mm) sheets by up to 140%. More recently **Yoshida** (**2014**) simulated the roughening behaviour of sheet metals with different thickness to grain size (*Ng*) ratios. The results showed that decreasing values of *Ng* increase the magnitude of surface roughening with respect to the sheet thickness, resulting in large geometric imperfections. Yoshida concluded that formability reduces with decreasing *Ng*, particularly for $Ng < 30$.

The impact of surface roughness on the onset of instability has led to several researchers incorporating microstructural parameters into forming limit prediction models. For example, **Jain et al.** (**1996**) used the model of **Parmar & Mellor** (**1978**) to incorporate the effect of surface roughening for formability predictions of 5XXX and 6XXX series aluminium alloys. **Parmar & Mellor's** (**1978**) model is based on observations made by **Tadros & Mellor** (**1975**) that a structural instability only develops after the onset of diffuse necking. The proposed model is a hybrid of **Swift's** (**1952**) instability condition and **Marciniak & Kuczyński's** (**1967**) imperfection model, where the surface roughness develops according to **Osakada & Oyane's** (**1971**) relationship up to the diffuse neck, and the M-K model describes the growth of the greatest asperity up to the localised neck. **Jain et al.** (**1996**) found that increasing the grain size increases the rate of surface roughening, thereby initiating a local instability at lower strains and reducing the forming limit. This conclusion was drawn independently by **Gronostajski & Zimniak** (**1992**) who used a modified M-K model to predict formability of steel and aluminium under linear and complex loading conditions.

Research published in the literature shows that combining microstructural parameters with continuum plasticity models leads to accurate FLC predictions. Whilst predictions of formability have

been extensively studied, less focus has been given to predicting the variation in strain behaviour anticipated at the forming limit. Certainly, no focus has been given to predicting the statistical character of formability that was measured in this research. The objective of this chapter is to determine whether strain heterogeneity at the forming limit can be predicted using a microstructure-based model, and whether such a model predicts the heterogeneity seen in the FMs derived in Chapter 3.

5.1 PREDICTING FORMABILITY

Many attempts have been made to predict formability, taking into account the theory of plasticity, material properties, and instability conditions. One of the most popular techniques is the rigid-plastic model proposed by **Marciniak & Kuczyński** (**1967**).

5.1.1 The Marciniak-Kuczynski Model

5.1.1.1 Overview

The Marciniak-Kuckzynski (M-K) model is based on observations made by **Marciniak** (**1965**) that under biaxial straining, instability in sheet metal manifests as a line perpendicular to the major stress direction. **Marciniak & Kuczyński** (**1967**) hypothesised that the location of the instability corresponds to some pre-existing defect, such as a geometric heterogeneity (e.g. a thickness imperfection) or a microstructural heterogeneity (e.g. crystallographic impurity, texture variation, grain size/orientation). To describe the deformation of a sheet, **Marciniak & Kuczyński** (**1967**) proposed a hypothetical specimen - depicted in Figure 51 - which is divided into two distinct regions: region A represents the material bulk with an initial thickness t_0^A and region B the thin groove with an initial thickness t_0^B. The magnitude of the initial heterogeneity is expressed by a heterogeneity coefficient f_0, defined in (Eq. 35), which is equivalent in effect to the ratio of thicknesses between the two regions.

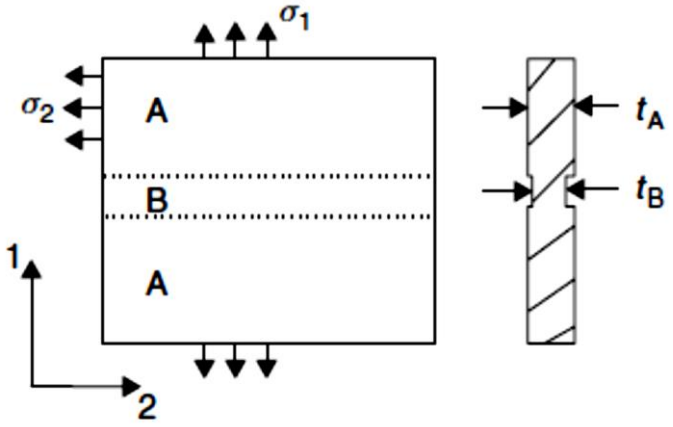

Figure 51: Schematic of the specimen hypothesised in the M-K model (image obtained from Marciniak et al. **(**2002**)***

$$f_0 = \frac{t_0^B}{t_0^A} < 0 \qquad \textit{Eq. 35}$$

When the bulk material is subjected to a constant stress ratio (governed by the principal stresses σ_1 and σ_2) and deforms by a constant strain ratio, the deformation of the M-K specimen is analysed with respect to the major strain increments in each region ($\delta\varepsilon_1^A$ and $\delta\varepsilon_1^B$). Deformation in the groove is subject to a geometrical constraint ($\delta\varepsilon_2^A = \delta\varepsilon_2^B$) and a load equilibrium condition ($\sigma_1^A t^A = \sigma_1^B t^B$). As a consequence of these boundary conditions, a constant strain increment in the bulk material

causes a higher strain increment inside the groove. With continued deformation, $\delta\varepsilon_1^B \gg \delta\varepsilon_1^A$ and the thickness of the groove reduces proportionally more than the bulk material. The strain ratio in the groove eventually tends towards plane strain, meaning the M-K specimen is representative of a sheet metal undergoing localised necking. When this instability condition is met, principal strains in region A are deemed to represent the forming limits of the specimen for the applied loading condition. Varying the loading condition enables forming limits to be calculated for a variety of strain paths, thereby facilitating the prediction of an FLC.

5.1.1.2 Modelling the Deformation of the M-K Specimen

The precise deformation of the M-K specimen is described using continuum plasticity models. Before a description is given, additional boundary conditions for the specimen's deformation are defined:

- The specimen is only subjected to proportional planar stresses (ρ^A = constant, $\sigma_3 = 0$)
- The principal stress axis is aligned to the specimen's orthotropic axis, with the initial geometric defect perpendicular to the major stress direction
- The specimen is subject to loads which do not cause tangential stresses ($\sigma_{12} = \sigma_{21} = 0$) or strain increments ($\delta\varepsilon_{12} = \delta\varepsilon_{21} = 0$)

The applied loading conditions dictate that principal stresses in region A (σ_1^A and σ_2^A) must follow a linear loading path, as shown by the line OP in principal stress space in Figure 52. Boundary conditions dictate that principal stresses in region B do not follow a linear trajectory. During initial loading, the imperfection causes principal stresses in region B to reach the yield curve before those in region A (represented by points A and B in Figure 52). Under these conditions, further loading is required for region A to yield and for the specimen to begin plastic deformation. Subsequent loading causes point A to continue travelling along OP until the path intersects the yield curve. Accordingly, the model's boundary conditions force point B to traverse around the yield curve (towards plane strain). The actual initial yielding of the M-K specimen occurs at two different points on the yield locus, shown by points A_0 and B_0.

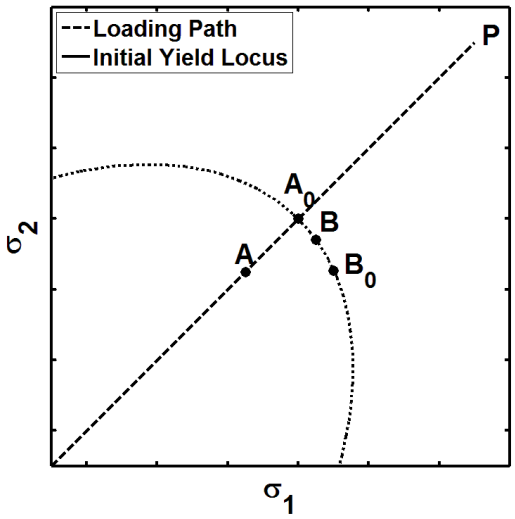

Figure 52: Principal stresses in regions A and B at yield

Boundary conditions imposed on the M-K model mean that subsequent plastic deformation in regions A and B occurs simultaneously with equal minor strain increments. The differing positions of points A_0 and B_0 on the yield curve dictate that regions A and B are subject to different stress ratios, and will deform along different strain paths. Assuming the associated flow rule, the strain increment

vector for each region is found by a perpendicular projection from points A_0 and B_0, shown in Figure 53a. Figure 53a shows that to satisfy the geometric constraint, a greater major strain increment occurs in region B than in region A ($\delta\varepsilon_1^B > \delta\varepsilon_1^A$). Consequently, $\delta\bar{\varepsilon}^B > \delta\bar{\varepsilon}^A$ and $\bar{\sigma}^B > \bar{\sigma}^A$. As a result, regions A and B evolve along two separate yield curves. Figure 53b shows that due to the slightly larger plastic strain increment, the yield curve defining region B expands slightly quicker than the yield curve defining region A. With the yield curve in region B leading the corresponding curve in region A, the groove deforms at higher rate than the bulk material. t^B reduces quicker than t^A, thereby decreasing f (increasing the magnitude of the defect) with continued deformation:

$$f = f_0 e^{(\varepsilon_3^B - \varepsilon_3^A)} \qquad \textit{Eq. 36}$$

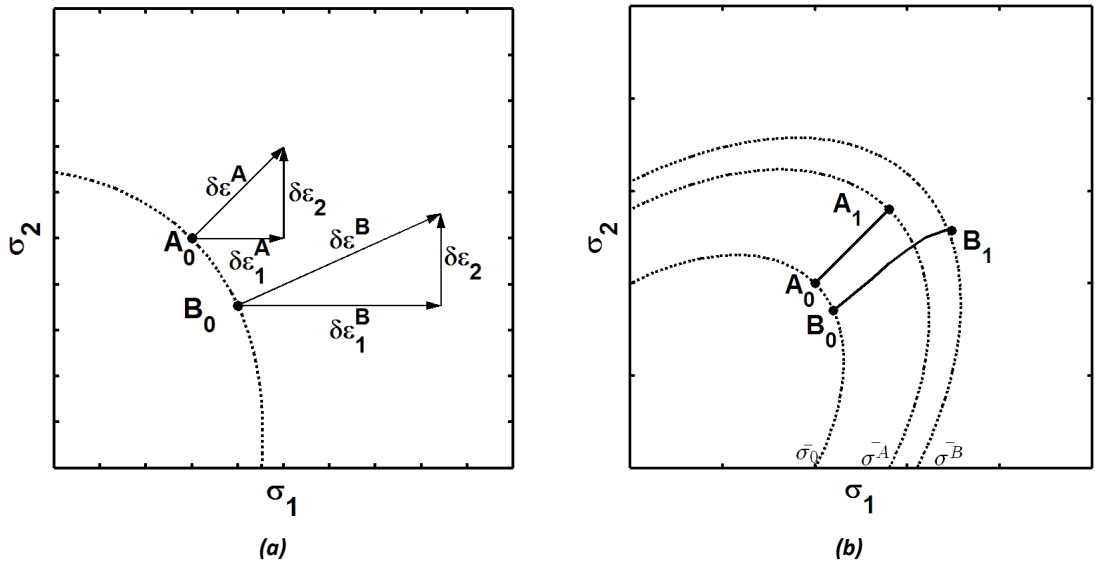

Figure 53: (a) Strain vectors at yield for the uniform and imperfection regions, (b) subsequent yield curves for regions A and B after strain increment

Under sustained loading, the stress ratio in the groove continues to traverse around the yield locus towards plane strain, shown by point B_F in Figure 54. As the yield stress in B tends towards plane strain the angle of the projected strain vector $\delta\bar{\varepsilon}^B$ becomes more acute and the strain parallel to the groove diminishes. Consequently, $\delta\varepsilon_1^B \gg \delta\varepsilon_1^A$, and the local instability condition is met.

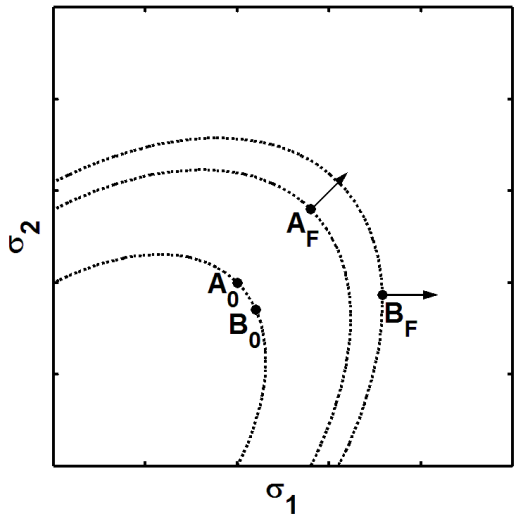

Figure 54: Initial and final yield curves of the M-K model, highlighting the differences in strain ratios at failure

5.1.2 Advancements to the M-K Model

From the explanation above it is obvious that f_0 is a mathematical representation of the magnitude of an initial defect, where f_0 << 1 indicates a severe defect and f_0 = 1 assumes the material is homogeneous. A common criticism of the M-K model is the lack of a precise physical definition for f_0. **Azrin & Backofen** (**1970**) performed in-plane stretching experiments on specimens of mild steel, stainless steel, copper, and brass. The thickness profiles of each material were measured before deformation, where it was found that f_0 was always greater than 0.997. To obtain close correlation to the measured forming limits, formability as predicted by the M-K model required f_0 to be much lower than the measured values. Azrin & Backofen concluded that the heterogeneity should include provision for the accumulated strain and the ratio of surface strains. Similar experiments by **Tvergaard** (**1978**) corroborated Azrin & Backofen's findings that unrealistically large initial imperfections must be used to match the M-K model to experimental results. **Ghazanfari & Assempour** (**2012**) noted that several researchers attempt to improve M-K model predictions by calibrating the model to a single experimental limit strain - commonly FLC_0 - to obtain a suitable value of f_0. The disadvantage of this technique is that the predictive capability of the M-K model relies on experimental measurements other than mechanical properties.

In order to overcome this deficiency, several researchers have proposed that the imperfection in the M-K model should correlate to a measurable source of heterogeneity, such as surface roughening. Modifications to the M-K model proposed by **Gronostajski & Zimniak** (**1992**) and **Nurcheshmeh** (**2011**) are based on a suggestion that the heterogeneity coefficient *f* evolves in the same manner as a surface roughness. The extension proposed by **Gronostajski & Zimniak** (**1992**) and **Nurcheshmeh** (**2011**) assumes that the initial thickness imperfection of the M-K specimen is represented by the initial surface roughness of the sheet, such that:

$$f_0 = \frac{t_0^A - 2R'_{MAX}}{t_0^A} \qquad \textit{Eq. 37}$$

where R'_{MAX} is the maximum surface roughness of the sheet, illustrated in Figure 55.

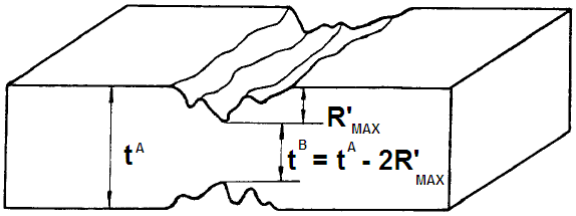

Figure 55: Alternative M-K specimen based on surface roughening (image adapted from Gronostajski & Zimniak **(**1992**)*)***

Research by **Osakada & Oyane** (**1971**) has shown that surface roughness increases in proportion to equivalent strain, and that the rate of surface roughening depends on the average grain size. To ensure that the M-K model evolves in the same manner as a surface roughness, the relationship derived by **Osakada & Oyane** (**1971**) (described in Eq. 38) is combined with Eq. 37 to describe the evolution of heterogeneity in the M-K specimen (Eq. 39). Both **Gronostajski & Zimniak** (**1992**) and **Nurcheshmeh** (**2011**) report that this modified M-K model improves limit strain prediction, with limit strains correlating more closely to experimental measurements than those predicted using the original M-K model.

$$R' = R'_0 + kd\bar{\varepsilon} \qquad \textit{Eq. 38}$$

$$f = \frac{t_0^A - 2(R_0' + kd\bar{\varepsilon}^B)}{t_0^A} e^{(\varepsilon_3^B - \varepsilon_3^A)} \quad \textit{Eq. 39}$$

Incorporating surface roughening behaviour into the M-K model provides an opportunity to predict strain heterogeneity (caused by surface roughening) at the forming limit. When surface roughness is modelled with the M-K model, the geometry of the asperities is represented by the different thicknesses of the M-K specimen. The cross-section of region A represents the highest surface peak and the cross-section of region B the lowest surface trough. Correspondingly, it is expected that regions A and B will experience different levels of strain. The difference in strains between the two regions is the range of strains that can be expected from the surface roughness. When the M-K specimen is deformed to the instability condition, the range of strains caused by surface roughening at the forming limit can be predicted.

5.2 METHOD

Each of the materials tested earlier in this report are simulated using the modified M-K model. To ensure materials' macroscopic behaviour is accurately described, suitable strain-hardening laws and yield surfaces are selected. Following the recommendations of the material suppliers, **Holloman's** (**1945**) hardening law (Eq. 3) is used to describe steels' strain hardening behaviour, and **Voce's** (**1948**) hardening law (Eq. 4) aluminium alloys' strain hardening behaviour. The parameters used for each material studied in this research are shown in Table 11. **Hosford's** (**1979**) criterion (Eq. 40) is used to describe steels' yielding characteristics, and **Barlat & Lian's** (**1989**) criterion (Eq. 41 - Eq. 45) aluminium alloys' yielding characteristics. The mechanical properties of each material are shown in Table 12.

Property/Parameter	AA6111T4	NG5754O	DP600	MS3
***K* (Holloman)**	-	-	950	230
***n* (Holloman)**	-	-	0.17	0.24
***A* (Voce)**	136	95	-	-
***B* (Voce)**	282	286	-	-
***C* (Voce)**	10.32	11.88	-	-

Table 11: Parameters used to describe strain hardening behaviour of tested materials

$$R_{90}\sigma_1^a + R_0\sigma_2^a + R_0R_{90}(\sigma_1 - \sigma_2)^a = R_{90}(R_0 + 1)\bar{\sigma}^a \quad \textit{Eq. 40}$$

$$a(k_1 + k_2)^M + a(k_1 - k_2)^M + c(2k_2)^M = 2\bar{\sigma}^M \quad \textit{Eq. 41}$$

$$k_1 = \frac{\sigma_1 + h\sigma_2}{2} \quad \textit{Eq. 42}$$

$$k_2 = \left[\left(\frac{\sigma_1 - h\sigma_2}{2}\right)^2 + p^2\sigma_{12}^2\right]^{\frac{1}{2}} \quad \textit{Eq. 43}$$

$$a = 2 - c = 2\sqrt{\frac{R_0}{1 + R_0} \cdot \frac{R_{90}}{1 + R_{90}}} \quad \textit{Eq. 44}$$

$$h = 2\sqrt{\frac{R_0}{1+R_0}.\frac{1+R_{90}}{R_{90}}} \qquad \textit{Eq. 45}$$

Property/Parameter	AA6111T4	NG5754O	DP600	MS3
R_0	0.71	0.84	0.87	2.28
R_{90}	0.71	0.84	1.09	2.51
a (Hosford)	8	8	-	-
M (Barlat)	-	-	6	6

Table 12: Parameters used to describe yield characteristics of tested materials

The modified definition of the material imperfection f, shown in Eq. 39, is based on observations made by **Osakada & Oyane** (**1971**) and others that surface roughening of forming grade sheet metals is linearly dependent on the material's grain size and plastic strain. The advantage of using this relationship is that easily obtainable microstructural parameters can be used to incorporate surface roughening behaviour into the M-K model, without relying on detailed crystallographic analysis. Measurements of materials' grain size and initial surface roughness are taken from research published in the literature.

The average grain diameter of NG5754O is obtained from research performed by **Jain et al.** (**1996**). Optical micrographs taken by Jain et al. showed that the grains are equiaxed with an average grain diameter of 21µm. The average grain diameter of AA6111T4 is also obtained from the research performed by **Jain et al.** (**1996**). Optical micrographs showed that the grains of AA6111T4 are elongated along the rolling and transverse directions. The average grain diameters were measured as 31µm and 18µm in the length and thickness directions respectively. Jain et al. argued that since surface roughening is caused by through-thickness deformation, surface roughening should be more influenced by the grain thickness than the grain length. Therefore, the average grain thickness of AA6111T4 is used in this research.

The granular dimensions of mild steel are obtained from research performed by **Gronostajski & Zimniak** (**1992**), who measured the average grain diameter to be 21µm. The average grain diameter of DP600 is obtained from research performed by **Tasan et al.** (**2014**). The average grain size of the martensite was measured as 2.7µm, and the average grain size of the ferrite matrix was 8.4µm. An analysis of the microstructure of DP600 showed that volumetric fraction of martensitic particles was 17.2%. The distribution of grain sizes in dual phase steels presents a complexity if the granular dimensions are to be represented by a single value. In this research, the microstructure is summarised by the weighted average grain diameter, which is calculated to be 7.4µm.

Initial roughness measurements for each material are also taken from research published in the literature. **Jain et al.** (**1996**) measured the initial maximum surface roughness (R'_{MAX}) of AA6111T4 and AA5754 as 3.6µm and 3.4µm respectively. **Gronostajski & Zimniak** (**1992**) measured the maximum surface roughness of mild steel as 2µm. Measurements made by the material suppliers show that the maximum surface roughness of DP600 is approximately 2µm.

The M-K model is explicitly computed using the numerical methodology described by **Hosford & Caddell** (**2011**). The methodology is briefly summarised below:

- The tensile load transfer between regions A and B of the specimen is balanced, so that:

$$\sigma_1^A t^A = \sigma_1^B t^B \qquad \textit{Eq. 46}$$

- The principle of equivalent plastic work entails that under planar stress conditions, principle stresses and principal strain increments are related by:

$$\bar{\sigma}\delta\bar{\varepsilon} = \sigma_1\delta\varepsilon_1 + \sigma_2\delta\varepsilon_2$$

$$\bar{\sigma}\delta\bar{\varepsilon} = \sigma_1\delta\varepsilon_1(1 + \alpha\rho) \quad \textit{Eq. 47}$$

  where α and ρ represent the principal stress and strain increment ratios respectively. The values of these ratios are calculated from the selected yield curve and the Levy-Mises flow rule:

$$\alpha = \frac{\sigma_2}{\sigma_1} \quad \textit{Eq. 48}$$

$$\rho = \frac{\delta\varepsilon_2}{\delta\varepsilon_1} \quad \textit{Eq. 49}$$

- For the purpose of this explanation, it is assumed that the material's hardening behaviour is described by Holloman's power law:

$$\bar{\sigma} = K\bar{\varepsilon}^n \quad \textit{Eq. 50}$$

- Combining the strain hardening relationship with Eq. 46 and Eq. 47 results in the following compatibility equation between regions A and B:

$$\frac{\sigma_1^A}{\bar{\sigma}^A}K\bar{\varepsilon}^{A\,n} = f\frac{\sigma_1^B}{\bar{\sigma}^B}K\bar{\varepsilon}^{B\,n} \quad \textit{Eq. 51}$$

- In the M-K model strains are incremented to find the onset of instability. The compatibility equation above is modified to include provision for strain increments:

$$\frac{\sigma_1^A}{\bar{\sigma}^A}(\bar{\varepsilon}^A + \delta\bar{\varepsilon}^A)^n = f\frac{\sigma_1^B}{\bar{\sigma}^B}(\bar{\varepsilon}^B + \delta\bar{\varepsilon}^B)^n \quad \textit{Eq. 52}$$

The iterative procedure to calculate limit strains from the M-K model is described below:

1. Select a stress ratio α^A to be constant throughout the calculation
2. Calculate ρ^A from the yield criterion and flow rule
3. Impose an increment $\delta\varepsilon_2$
4. Calculate the increment $\delta\varepsilon_1^A$
5. Estimate the corresponding increment $\delta\varepsilon_1^B$
6. Calculate f, ρ^B, α^B, and $\delta\bar{\varepsilon}^B$ for the groove
7. Substitute values into Eq. 47 to calculate $\delta\bar{\varepsilon}^A$
8. Use the compatibility equation to calculate $\delta\varepsilon_1^A$
9. Compare the value of $\delta\varepsilon_1^A$ to the originally estimated value. Iterate stages 4-9 until the estimated and calculated strains are equal
10. Calculate $\delta\varepsilon_1^B/\delta\varepsilon_1^A$ to check if the instability condition has been met
11. Impose a new strain increment $\delta\varepsilon_2$, and repeat the procedure until the instability condition is met
12. At the instability limit, record the principal strains ε_1^A, ε_2^B, ε_1^A, ε_2^B.
13. Reset the model parameters and apply a new stress ratio α^A to find limit strains under a different load path

The methodology above is compiled into a MATLAB script, where the inbuilt "fzero" solver (described in the **Mathworks** (**2015**) reference documentation) is used to find the roots of the compatibility equation. "fzero" uses a combination of bisection, secant, and inverse quadratic interpolation methods to find the roots of a non-linear function. Following the recommendations of **Hosford & Caddell** (**2011**) $\delta\varepsilon_2$ is incremented at values of 0.005. Limit strains are calculated for each material over a minimum of four deformation paths (uniaxial tension, plane strain, intermediate biaxial tension, and equibiaxial tension) to compliment the range of strains which were experimentally measured.

Conventional protocol is to report the results of each M-K model as a series of limit strains, where each limit strain reflects the principal strains in region A at the onset of instability. However, the aim of this investigation is to predict the range of strains that occurs at the onset of instability. Strain variation, caused by surface roughening, is recognisable from the behaviour of the modified M-K specimen. From Figure 55 it is apparent that region A is reflective of the highest surface peak, and region B the lowest surface trough. It is expected that the lowest strains will occur at the surface peaks, and the highest strains in the troughs. Therefore, strains calculated in region A represent the lower bound of strains in the specimen, and strains in region B the upper bound of strains. The difference in strains between the two regions provides a prediction for the range of strains in the specimen, caused by surface roughening.

The upper and lower strain bounds predicted by the modified M-K model will be represented on the FLD as two deterministic boundaries (similar in character to an FLB). Figure 56 shows the strain paths taken by regions A and B, under five different loading conditions, up to the onset of local instability, and the corresponding lower and upper bounds.

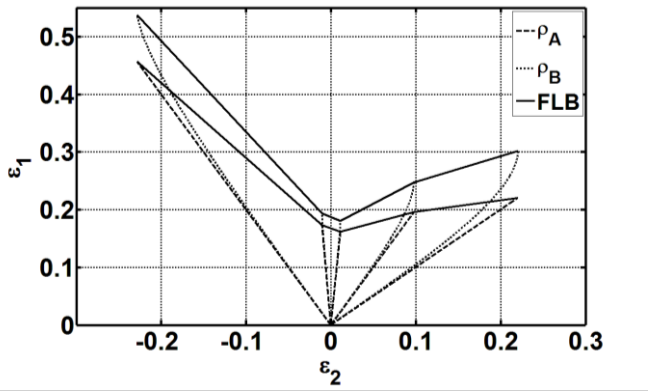

Figure 56: Strain paths predicted by the modified M-K model for AA6111T4

To facilitate a comparison between the strain bounds predicted by the modified M-K model and the strain measurements made in this research, strain bounds will be benchmarked against two sets of data. Firstly, to benchmark the predictions against the innovative statistical strain characterisations that were made, the bounds will be compared to the Formability Maps created in Section 3.6. Secondly, to benchmark the predictions against a standardised dataset, the bounds will also be compared to the ISO12004-2 limit strain measurements made in Section 3.1.

5.3 RESULTS

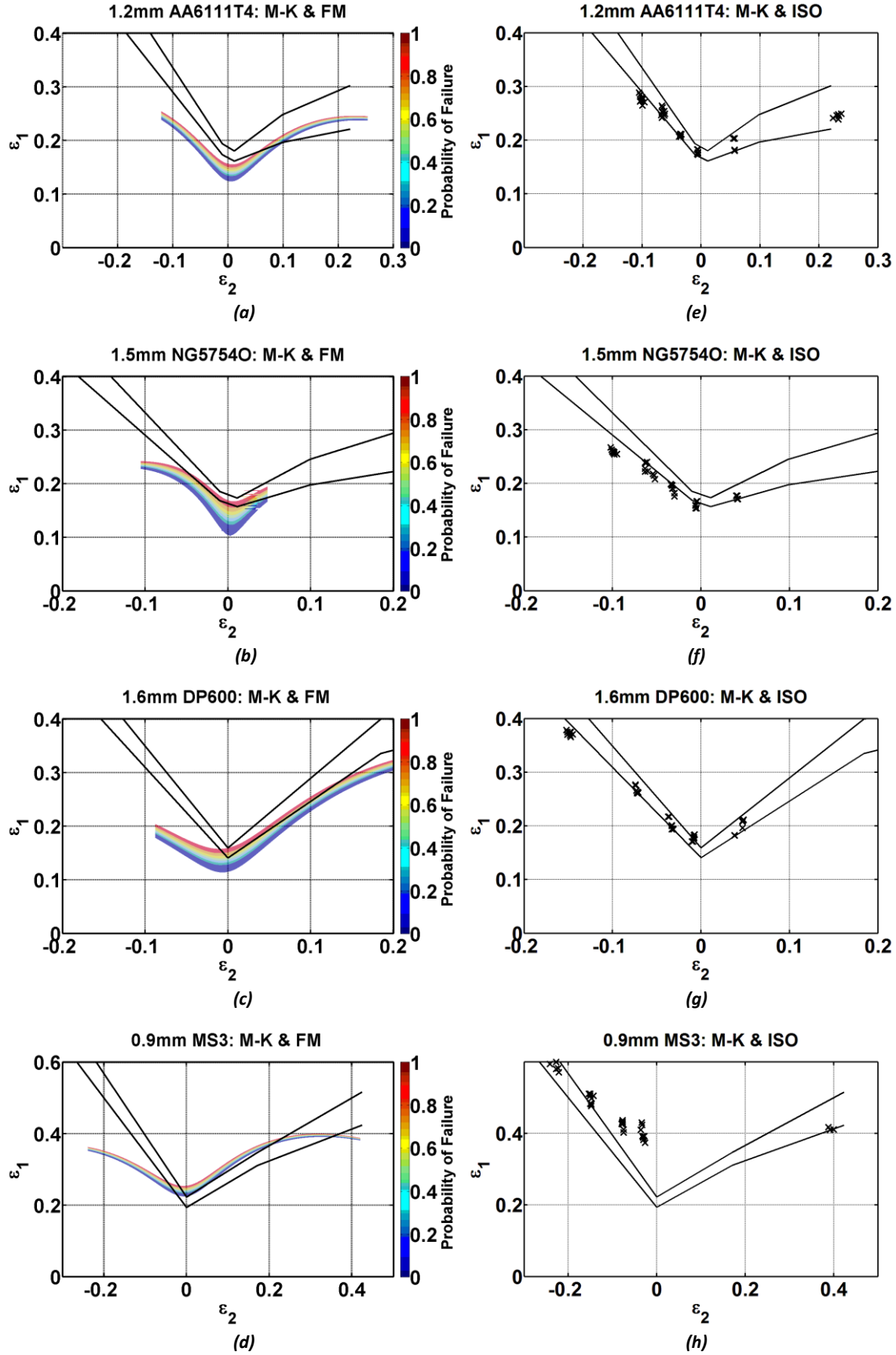

Figure 57: Marciniak-Kuckzynski predictions using the extension proposed by Gronostajski & Zimniak **(**1992**) *compared to (a-d) the Formability Maps, and (e-h) ISO-derived limit strains***

Figure 57 shows that the range of strains at the forming limit, predicted by the M-K model, varies between materials and strain paths. The range is narrowest in plane strain for all the simulated materials. NG5754 exhibits the narrowest range in plane strain spanning approximately 0.015 (true major strain), with MS3 exhibiting the widest range spanning approximately 0.025 (true major strain). Strain bounds progressively widen towards uniaxial tension, and rapidly widen towards equibiaxial tension. In the plane strain region the difference in strains reflects the definition of necking, i.e. $\delta\varepsilon_1^B / \delta\varepsilon_1^A = 10$. In the uniaxial and biaxial regions the increased difference is due to the neck having to change strain path from uniaxial/biaxial tension to plane strain. These predictions conflict with the measured FMs which are broadest in the plane strain and narrow towards uniaxial and equibiaxial tension.

The M-K model predicts that for each of the simulated materials, formability in uniaxial tension and biaxial tension is higher than that which was measured for the FM. These results corroborate **Ghosh's** (**1978**) findings that the M-K model tends to overestimate formability in equibiaxial tension.

For the two aluminium alloys, the predicted lower bound closely follows the P(Failure) = 0.9 contour of each FM – particularly in plane strain and equibiaxial tension. Under uniaxial tension the lower bounds deviate above the FM with increasing minor strain. For DP600 the lower bound of the FLB is very close to the P(Failure) = 0.9 contour under biaxial tension, but falls below the contour under plane strain. Under increasing uniaxial tension, the FLB rapidly deviates above the FM. The characteristics of the strain predictions made for MS3 are markedly different to the other materials. Under plane strain, the upper bound is below the lowest contour of the FM. Between plane strain and intermediate biaxial tension, the upper bound matches the P(Failure) = 0.1 contour of the FM. Between intermediate and equibiaxial tension the upper and lower bounds cross the FM and rise above the P(Failure) = 0.1 contour. Under compressive minor strains the bounds cross the FM and rises significantly above the FM, where under uniaxial tension formability predicted by the modified M-K model is almost double that which was measured for the FM.

For AA6111T4 and DP600, the predicted strain bounds offer a remarkably good replication of the limit strains measured using the standard ISO12004-2 method. The predicted strain bounds for these two materials almost totally encompass the limit strains. For NG5754O the limit strains are not entirely encapsulated by the prediction bounds, with most of the limit strains falling slightly below the lower bound. For MS3, however, the predictions are less accurate. Formability in plane strain is under-estimated by around 50% (around 0.2 true major strain), although better predictions are achieved in uniaxial and equibiaxial tension.

5.4 DISCUSSION

Differences between the predicted range of strains and the measured Formability Maps raise questions concerning the origin of these discrepancies. One possibility is that is that evolution of the heterogeneous region B does not fully conform to physical reality. For example, in this work it is assumed (as in the original work of **Marciniak & Kuczyński** (**1967**)) that the orientation of the initial surface defect runs perpendicular to the major stress direction, and remains so during deformation. However, work by **Hutchinson & Neale** (**1978**) shows that the defect (and, by association, the neck) does not remain in its initial orientation throughout deformation. Rather, it was demonstrated that due to in-plane shear increments the band undergoes a rotation. It was proposed that the rotation (φ) of the defect is a function of the amount of deformation incurred (described in Eq. 53). **Hutchinson & Neale** (**1978**) found that limit strains predicted using this modified model were more accurate than the original theory – particularly in the uniaxial region where the M-K model was shown to over-estimate the forming limit. The modified M-K model constructed in this research

makes no account for changes in the orientation of the inherent heterogeneity. Consequently the predicted limit strains can be considered optimistic, thereby providing a partial explanation of the discrepancy between the results of the model and the measured Formability Maps.

$$\tan(\varphi + d\varphi) = \tan(\varphi)\frac{1 + d\varepsilon_1^A}{1 + d\varepsilon_2^A} \qquad \textit{Eq. 53}$$

Another possibility is that the definition of intrinsic heterogeneity used in the modified M-K model does not fully consider the underlying mechanisms responsible for surface strain variation. The modified f-value (defined in Eq. 39) was based on the surface roughening equation derived by **Osakada & Oyane** (**1971**). It was assumed that strain variation in the M-K specimen is the result of surface roughening, influenced by the material's average grain size and plastic strain. However, the distortion of individual grains is unlikely to be the sole cause of the DIC-measured strain variation which was observed in this research.

The (statistical) variation in DIC-measured surface strains reflects the reality that plastic deformation does not occur smoothly and homogeneously. The review of the literature documented in Chapter 2 highlighted that the surface conditions (and associatively, the surface strains) of plastically deformed sheet metals are influenced by the crystalline structure; the grain size; the textures present; and the existence of multiple phases. Whilst the modified M-K model has provision for the influence of the grain size, the influence of the microstructure is not accounted for.

The materials tested in this research each have microstructural characters that are known to impact surface strain behaviour. Using data published in the literature, each material is discussed in turn.

In AA6111T4, as well as other aluminium alloys and stainless steels, the collective deformation of hard and soft grain colonies causes differential straining that results in macroscopic surface banding. **Wittridge & Knutsen** (**1999**) observed banding during tensile deformation of an aluminium alloy when the tensile load was perpendicular to the specimen's rolling direction. An explanation for this behaviour was given from the illustrations shown in Figure 58. In Figure 58a it is shown that the microstructure of this alloy contains colonies of R-component grains elongated along the rolling direction, situated within a mainly cubic matrix. In Figure 58b it is shown that when straining commences, anisotropic grain roughening occurs due to the incompatibility between the two textures. Specifically, the R-component colonies are more resistant to thinning in the normal direction, and it is in these regions where the "peaks" of the surface bands occur. In Figure 58c it is shown that the lower strain hardening capacity of the cubic texture invokes "recesses" in the material, which eventually nucleate to form "troughs" that lie perpendicular to the loading direction. Once the macroscopic bands have fully formed, shown in Figure 58d, the material experiences macro-scale strain variation, with localised necking initiating in the deepest trough (analogous to the M-K model described previously).

A key observation made by **Wittridge & Knutsen** (**1999**) was that a banded surface profile only manifests when the tensile axis is perpendicular to the rolling direction. This was attributed to the continuity of the texture distribution along the rolling direction. When the tensile axis is parallel to the rolling direction, the texture is less continuous along the direction perpendicular to the load. Consequently the formation of bands is less likely. Anisotropic surface roughening makes the orientation of the sheet important for macroscopic strain localisation, and helps explain why a localised instability initiates at different levels of strain when the major strain axis is aligned to different sheet orientations, as shown by the FLCs of **Stoughton & Yoon** (**2012**).

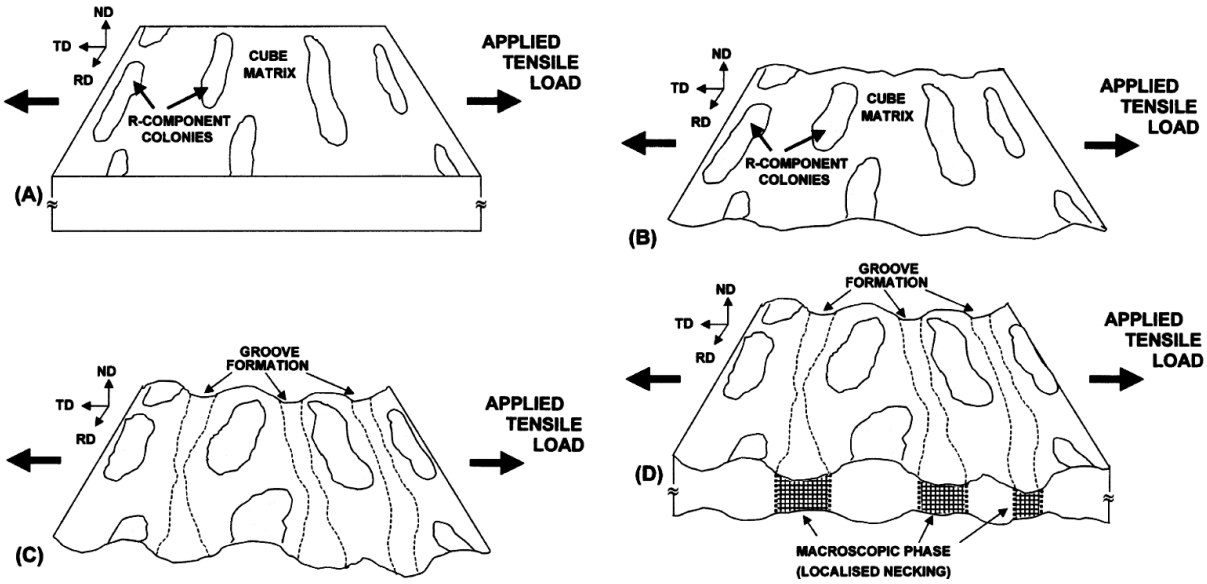

Figure 58: Schematic illustration made by Wittridge & Knutsen **(**1999**)** ***showing (a) the occurrence of R-component colonies within a cube matrix aligned perpendicular to the tensile load, (b) initial development of surface roughening, (c) linking of valleys to form continuous bands, (d) macroscopic phase leading to strain localisation through the specimen thickness***

Raabe et al. (**2003**) also performed an investigation into the relationship between texture and strain heterogeneity in an AA6XXX alloy. Micro-strain measurements demonstrated that changes to the surface topography are dictated by the spatial and through-thickness distribution of Goss, Cube, and rotated Goss grains. This investigation was extended by **Guillotin et al.** (**2011**) who concluded that the first three or four grain layers are important to the surface property. More recently, **Stoudt et al.** (**2011**) investigated the fundamental relationships between microstructure and strain heterogeneity in AA6022. EBSD was used to construct microstructural maps of Taylor factors, which were then overlain on corresponding maps of surface strain topography. It was found that large topographic differences (areas of high strain) were situated at triple grain junctions where a large difference in Taylor factors exists between the neighbouring grains. This corroborates the findings of **Wittridge & Knutsen** (**1999**) and **Raabe et al.** (**2003**) that strains develop at the boundaries of hard and soft grains. It was also noted by **Stoudt et al.** (**2011** that different sized grains within the microstructure contribute towards strain heterogeneity. The highest strains were observed at grain boundaries adjacent to the smallest grains. This was attributed to the Hall-Petch effect, where the yield strengths of small grains are expected to be higher than larger grains.

In DP600 the microstructure is characterised by dispersed martensitic particles set within a ferrite matrix. **Tasan et al.** (**2014**) have recently shown that the dimensions and dispersion of the two phases have a significant influence on spatial strain heterogeneity at the micro-scale. For dual phase steels with large ferrite grains and small martensite particles, strain heterogeneity is strongly influenced by the ferrite grain size. Experimental measurements showed that in this type of microstructure, intra-granular straining manifests as narrow bands which eventually spread evenly throughout the material. Conversely, for dual phase steels which have smaller ferrite grains and higher martensite content, strain behaviour is dictated by the distribution of martensite. When fine particles of martensite are homogeneously distributed throughout the ferrite matrix, plastic deformation manifests as a series of thin strain bands spread over the microstructure. This ensures that strains are homogeneously-dispersed throughout the ferrite matrix. However, when the microstructure contains predominantly bulky particles of martensite, the martensite is able to accommodate higher levels of stress. This causes straining to be concentrated in a sample of ferritic

grains that lie in locations of highest shear, resulting in a more heterogeneous strain distribution. As a consequence, macroscopic strain localisation occurs at low(er) strain levels for microstructures with bulky martensitic particles than for microstructures with finely dispersed particles.

In NG5754O, surface strain behaviour is dominated by the Portevin-Le-Chatelier (PLC) effect, which manifests as a series of localised bands of high strain rate. The PLC effect is a deformation-induced mechanism caused by solute Mg atoms temporarily pinning dislocations' motion. High stresses are required to overcome these pinned dislocations, following which deformation is rapid until the dislocation is blocked by another set of Mg atoms. As a consequence of this intermittent dislocation motion, AA5XXX alloys deform heterogeneously through a series of localised strain bands. These bands are either static, or propagate along the length of the material. An example of a strain topography caused by PLC is shown in Figure 59. Figure 59 shows the DIC-measured strain topography of a NG5754O specimen which was deformed during the experiments conducted in Chapter 3. The specimen is deformed under plane strain conditions; with the DIC measurement showing deformation approximately midway through a Marciniak test (i.e. before the onset of necking). The topography shows that the PLC bands' amplitude is approximately 0.03 (true thinning strain) - higher than the variation predicted using the modified M-K model.

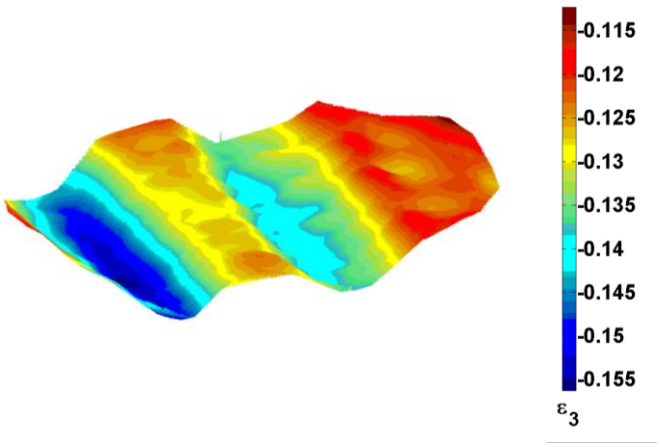

Figure 59: Strain topography of specimen of NG5754O undergoing plane strain deformation, demonstrating the PLC effect

The published research discussed in this section helps highlight the limitations of the modified M-K model used in this Chapter, and helps explain the discrepancies between the predictions made and the measured FMs.

Firstly, summarising the impact of grain size on surface roughening using an average grain diameter is not suitable for all materials. This approach cannot account for elongated grains present in certain alloys, such as AA6111T4. If grain rotation is a prominent mode of surface roughening, the grains' elongation could become pertinent to the surface condition. **Jain et al.** (**1996**) suggested that the grain aspect ratio may be a more appropriate measure to account for the effect of grain geometry on the surface behaviour. Furthermore, an average grain diameter cannot account for materials which exhibit a broad range of grain sizes, and whose interactions also contribute towards heterogeneous strain behaviour. To account for this behaviour in surface strain predictions, the distribution of grain sizes should be considered.

Secondly, describing the evolution of surface roughening as a scalar function (as is done in Eq. 38) is not appropriate for materials that exhibit strong anisotropic texture components. Textural anisotropy makes the angle between the loading direction and sheet orientation important to the surface condition. This helps explain the differences in surface strain variation that were measured

for different strain paths. The distribution and orientation of elongated textures is pertinent to the spatial distribution of surfaces strains of aluminium alloys, and the initiation of a macroscopic instability. Due to the textural anisotropy caused by the rolling process, surface roughening should be treated as a tensorial rather than scalar problem. To improve the predictions made in this research, a crystal plasticity model could be integrated into the M-K model. One option would be to adopt the method of **Moore & Bate** (**2002**) who based the *f*-value of the M-K specimen on initial texture. **Moore & Bate** (**2002**) assumed that a localised neck forms in a region of the material which exhibits a high texture density close to the ideal Cube orientation. Reasonable limit strain predictions were reported using this method, although the authors accepted that better consideration for textural evolution within the M-K model is required. A second option would be to adopt the methods of **Tóth et al.** (**1996**) and **Lee & Wen** (**2006**) who combined the M-K model with a generalised Taylor-type polycrystal model.

Thirdly, the modified M-K model makes no consideration for the complex PLC behaviour evident in AA5XXX series alloys. Whilst the modifications made by **Gronostajski & Zimniak** (**1992**) did not claim to account for this behaviour, strain heterogeneity caused by the PLC effect is prominent on the surfaces of NG5754O specimens measured in this research. **Hopperstad et al.** (**2007**) numerically demonstrated that the PLC effect is significant for the onset of instability, where an increase in PLC bands causes a reduction in formability in uniaxial and biaxial tension. Therefore, the PLC effect should be considered when predicting both strain behaviour at the forming limit, and the level of formability itself. One option would be to utilise the model of **McCormick & Ling** (**1995**), who recognised that to model dynamic strain aging, it is necessary to describe the diffusion of solute atoms towards the (temporarily) pinned dislocations. **McCormick & Ling** (**1995**) derived a relationship between the concentrations of atoms, the average “waiting time” at the dislocation, and the resulting flow stress behaviour. This relationship was incorporated into a finite element model by **Hopperstad et al.** (**2007**) who was able to study the orientation, width, velocity, and strain rates of the bands and their respective influences on surface strain behaviour. **Hopperstad et al.** (**2007**) also constructed a finite element M-K model to study the impact of the PLC effect on biaxial limit strains. An increase in formability with increasing strain rate was predicted. This model is an ideal solution to improve upon the strain predictions made in this research.

Finally, to predict the full statistical character of formability (rather than just the range of strains at the forming limit), the existence of statistical features at the micro-scale must be established. A fundamental characterisation of the distribution of grain dimensions, orientations, and the size of texture colonies is required to establish the core statistical features of the microstructure, and to understand how its character evolves during deformation. Further work is required to obtain a statistical correlation over different length scales between the granular distortion, micro-scale strain heterogeneity, and the macro-scale strain heterogeneity measured in this research.

5.5 CONCLUSIONS

- Levels of formability predicted in plane strain using the modified M-K model are broadly similar to experimental measurements. Under uniaxial and equibiaxial tension, formability predictions are optimistic
- The range of strains predicted by the M-K model in plane strain is smaller than the range of strains measured in this research, described by the FM. Under uniaxial and equibiaxial tension, the predicted range of strains is larger than that described by the FM
- Surface roughness arising from individual granular distortions does not explain the heterogeneous strain distribution observed in this work

- Improvements to predictions of strain variation at the forming limit should be made by considering the influence of the microstructure – specifically the inherent variation in grain geometries, the spatial distribution of texture components, and the cumulative effect of deforming colonies of grains on the surface strain
- To provide a full statistical prediction, such as was measured in Chapter 3, the statistical behaviour at the micro-scale should be established

6 CONCLUSIONS

The FLC characterises strains that lead to the failure of a sheet metal along an industrially relevant range of strain paths. Conventionally, it defines failure for materials that undergo deformation along linear paths. Failure is assumed to occur deterministically - either in the form of a localised neck or fracture - so there is a discrete boundary between “safe” and “unsafe” strains.

The FLC is based on forming limit experiments along a range of strain paths, which are usually repeated between 3 and 5 times for each path. The individual strains tend to produce a spread of strains. In some materials the spread may be as large as 0.05 true strain in the direction of the strain path. FLCs fitted to this data typically do not reflect this uncertainty.

One factor that gives rise to the scattered strain data is the test method advocated by ISO12004-2. In particular, there are two aspects of the method that are open to subjective interpretation. The first is the use of a “position-dependent” technique for determining the limit strains, which selectively analyses strains in a pre-determined area of the specimen. The second is the determination of the time at which necking occurs.

Another factor which contributes towards the scattered strain data is the inherent behaviour of sheet metals. At the measurement scale used in formability measurement, strains are typically expected to behave in a homogeneous manner. DIC strain measurements presented in Chapters 2 and 3 conflicts with this assumption, and show that surface strains behave in a heterogeneous manner. These measurements imply that the neck is an inherently heterogeneous entity.

The surface strain heterogeneity measured in this work has a statistical character. Statistical trends are identifiable in the DIC-measured strain populations of specimens subject to in-plane formability tests. Plastic deformation is accompanied by discernible changes to the location, dispersion, and shape of the surface strain distribution. The most prominent trend is the emergence of a bimodal shaped distribution during necking. The central argument of this research is that due to the statistical nature of deformation, failure (necking) must be also described statistically.

In this research, an innovative statistical model is used to quantify DIC-measured strain behaviour in specimens undergoing a Marciniak test. The 2-component Gaussian Mixture Model provides an excellent replication of the evolving strain distribution, and quantitatively describes the statistical trends that occur. This work is the first example of an adaptive statistical model being used to characterise intra-specimen strain behaviour in a formability test.

The utility of the GMM is able to resolve the limitations of ISO12004-2. Using the GMM, a new methodology is proposed to objectively characterise the statistical nature of formability and eliminate the subjectivity required by the current ISO-standard method.

The GMM can objectively identify a localised neck on a specimen from the characteristics of the bimodal strain distribution that occurs during necking. The GMM is used to perform statistical clustering, where the strains responsible for the bimodal strain distribution are grouped into two clusters. Strains that are responsible for the uppermost mode, and which are also responsible for changing the shape of the strain distribution, are located inside the neck. The GMM objectively identifies the sample of strains responsible for the neck, and locates them on the test specimen.

The GMM can objectively identify the onset of localised necking from within a DIC-measured strain history. The trends that occur in the strain population are caused by the emergence of a neck, and are recognisable by tracking the parameters of the GMM. When a neck initiates, the difference in

strain rates in the specimen causes the GMM components to diverge. At the onset of localised instability, the GMM locations rapidly diverge, and the component weights unbalance. Constructing a time series for the GMM parameters over the course of an experiment makes the onset of localised necking visually recognisable, and is objectively identifiable using a linear regression model.

The formability of a single specimen is conventionally described by a single limit strain. Summarising the localised neck by a single strain value, without considering the dispersion of strains attributed to it, does not describe the statistical nature of the neck. The GMM describes formability as a risk of failure, where “failure” is defined as the probability of observing a strain inside the neck at the onset of localised necking. This provides a more precise portrayal of the forming limit, and removes the ambiguity caused by summarising formability by a single strain value.

Deterministic FLCs do not describe the nature of strains at the forming limit, as reported by the GMM. Strains clustered at the forming limit by the GMM are not a continuous dataset. The data is in binary form. Fitting a logistic regression to strains clustered by a GMM translates the measurements into a complimentary probabilistic formability criterion. The logistic regression describes the transition between strains classified as “safe” by the GMM and strains classified as “failed”. The results are presented as a Formability Map, which shows the probability of failure contours on the Forming Limit Diagram.

Formability Maps measured for six automotive-grade sheet metals have similar geometries to FLCs obtained from the standard ISO12004-2 method. The lowest amount of formability still occurs at plane strain, with formability being higher in uniaxial tension and equibiaxial tension. FMs measured for aluminium alloys and high strength steels are closely aligned to the FLCs. Greater discrepancy occurs between the Formability Maps and the FLCs calculated for mild steel. This was attributed to the sensitivity in identifying the onset of localised necking for this material.

An outcome of this research is that formability should not be treated as a deterministic boundary between “safe” and “unsafe” strains. The statistical nature of the Formability Map provides stamping engineers with the precise measure of the risk of failure that is missing from the FLC. When used to interpret the results of a stamping simulation, the increased precision provided by the Formability Map enables engineers to identify areas of a simulated panel which are likely to fail, and removes the ambiguity caused by estimating the risk of failure from the proximity of surface strains to an FLC. Since automotive panels tend to have high piece, tooling, and development costs, the FM will reduce the commercial risk associated with these panels, and reduce the likelihood of corrective actions required to rectify a suboptimal process

Predicting the statistical nature of formability requires consideration for the microstructural behaviours responsible for surface strain heterogeneity. It was postulated in this research that one source of surface heterogeneity is microstructural deformation which fails to homogenise at the macroscopic scale. Incorporating an empirical surface roughening relationship into the Marciniak-Kuckzynski shows that the level of formability can be reasonably predicted from microstructural parameters. However, to more accurately predict the strain variation at the forming limit, more detailed models of the collective behaviour of polycrystals during plastic deformation must be considered. Specifically, models that predict strain variation arising from discontinuous strains steps within grains, at grain boundaries, and at phase boundaries are required.

In summary, the aim of this Engineering Doctorate, which was to understand and characterise the uncertainty in scattered limit strains, and develop a more accurate and precise method for determining and representing formability, has been met. Innovation is demonstrated in the creation

of a statistical method for determining and representing formability, based on the novel application of a Gaussian Mixture Model.

6.1 Future Research

This research has shown that plastic deformation has a statistical character that adds an uncertainty to the measurement of forming limits, which is currently neglected. Using appropriate tools such as the GMM, a "time-dependent" procedure was found to be more sensitive to identifying the onset of necking. Re-casting the formability of a material in statistical terms allows a more realistic assessment of the feasibility of production panels that may otherwise be described as "marginal". Despite these improvements to the description of formability, three areas of future research have been identified:

1. Improve the description of the diffuse neck during the formation of a localised neck to more precisely determine the onset of localised necking
2. Develop an alternative method for conducting feasibility assessments of automotive panels to account for the impact of the stamping process on formability
3. Increase the resolution of DIC measurements to (statistically) correlate micro-scale strain behaviour to macro-scale strain behaviour

6.1.1 Improving the Description of the Transition from Diffuse to Localised Necking

The statistical characterisation performed in this research shows that the distribution of strains in a Marciniak specimen changes character during the evolution of the neck. A bimodal distribution forms during incipient necking, where the upper mode encompasses strains inside the diffuse neck. When a localised neck forms, the upper mode changes to exclusively describe strains inside the localised neck. Strains which remain in the diffuse neck are "absorbed" into the lower mode, demonstrating they have a closer statistical relationship to the bulk material than the localised neck. When absorbed into the lower component, the statistical character of the diffuse neck is lost. Figure 27d shows how the diffuse neck is recognised by the GMM on a Marciniak specimen before the formation of the localised neck, and Figure 28d demonstrates how it (statistically) merges back into the bulk material when the localised neck has matured.

An inability to simultaneously differentiate between the localised neck, diffuse neck, and bulk material causes difficulty in precisely identifying the onset of localised necking. Specifically, difficulty occurs when the transition from diffuse to localised necking is gradual, as demonstrated by the MS3 specimen studied in Figure 45. The prolonged necking behaviour of MS3 causes the 2-component GMM to separate gradually, and doesn't demonstrate the sharp inflection point that characterises other materials. Consequently, the forming limit is less easily identifiable. This behaviour explains why a conservative Formability Map was obtained for MS3, shown in Figure 44, compared to standardised forming limit measurements. To more precisely identify the onset of localised necking and improve the description of the necking process, it is necessary to track the behaviour of the bulk material, diffuse neck, and localised neck simultaneously.

To simultaneously characterise all three states on the specimen, further research is required to recover the strains describing the diffuse neck from the strain distribution. This could be examined by extending statistical clustering to strains which are not the responsibility of the localised neck. For example, the diffuse neck could be recovered by fitting a second 2-component GMM to the strains which are not attributed to the localised neck. Alternatively, a 3-component GMM could be fitted to the entire strain population to find, and differentiate between, all three states. The cogency of applying more detailed statistical models to the strain distribution requires further investigation.

6.1.2 Quantifying the Impact of the Stamping Operation on the Formability Map

The main focus of this Engineering Doctorate was the identification and characterisation of the localised neck. Whilst this research has advanced the understanding of strain behaviour at the forming limit, and has proposed an innovative technique for precisely determining and representing formability, it does not provide a full and accurate solution for assessing the formability of industrial panels. This is because not all the risks to formability, which were identified at the project's outset, have been addressed. In particular, this research has not addressed the uncertainty caused by applying a formability criterion derived under proportional planar loading conditions to assess the formability of industrial panels which have undergone non-proportional loading. Tackling this discrepancy is necessary to address the outstanding issues related to quantifying the risk of failure for an automotive panel.

The complex tooling geometries required to form automotive panels mean that proportional planar loading conditions, as invoked by standardised formability tests, are rarely realised in industry. Non-linear strain paths and non-planar stress states are an inherent characteristic of automotive panels. Evidence published in the literature, such as **Graf & Hosford** (**1994**), show that non-linear strain paths can cause either an increase or decrease in formability, depending on the paths taken. Other evidence published in the literature, such as **Allwood & Shouler** (**2009**), show that compressive stress states can significantly enhance the level of achievable formability. The majority of the published research appears to focus on examining the effects of these conditions in isolation. Little experimental evidence was found to quantify the impact of concurrent conditions, e.g. a material undergoing changing strain path and a change in planar loading conditions, on formability, as would be expected in an actual manufacturing operation. To accurately assess the risk of failure in an industrial panel, further research is required to quantify the cumulative impact of deformation conditions on the Formability Map.

6.1.3 Correlating Microscopic Plasticity to Macroscopic Strain Behaviour using High-Resolution DIC

It was postulated in the review of the literature (Chapter 2), and in the discussion following formability prediction (Chapter 5), that the surface strain topographies characterised in this research are caused by micro-scale heterogeneities which fail to homogenise at the macro-scale. The potential impacts of the surface, grain size, texture, and the presence of multiple phases were discussed. However, due to the resolution of the DIC measurements which were made during the Marciniak tests, the relationships between microscopic distortions and the measured macroscopic statistical behaviour have only been postulated. To affirm the postulations made around the influence of grain size, texture, and phases, on the statistical behaviour, and to ascertain whether statistical features exists at the micro-scale, higher resolution DIC measurements should be made.

The DIC measurement resolution achieved in this work is limited by the airbrush technique used to create the stochastic surface speckle pattern. In Submission 3 it was found that due to the size of the speckles, accurate cross-correlation was only possible when the un-deformed DIC element was 0.9x0.9mm or greater. Consequently, granular-scale distortions are (to a certain extent) smoothed out within the locus of each element. To obtain higher resolution DIC measurements, a finer pattern is necessary.

Several investigations have been identified in the literature which have used alternative methods of surface pattern generation to obtain sub-millimetre DIC resolutions. For example, **Gioacchino & Quinta da Fonseca** (**2012**) used gold vapour deposition to produce a stochastic pattern with speckle sizes between 50nm and 150nm. Consequently, a small (0.2x0.2μm) DIC element size was achieved to enable a higher measurement resolution. Alternatively, **Tasan et al.** (**2014**) used a colloidal silica

solution to generate speckles between 4nm and 15nm, thus obtaining sub-micron resolution. **Tasan et al.** (**2014**) performed DIC on a series of SEM images taken at different levels of deformation. By overlaying the DIC-measured strain maps onto corresponding EBSD measurements, Tasan et al. were able to recognise intra-granular slip bands and differential straining at the grain and phase boundaries of DP600 and DP800. Further research is required to statistically characterise micro-scale strains of the materials studied in this research. Furthermore, any micro-scale characterisations should be correlated to the underlying plastic behaviour of the tested materials, and to the statistical behaviours measured in this research.

LIST OF REFERENCES

Abspoel, M. et al., 2011. Inherent influence of strain path in Nakazima FLC testing. In *Proceedings of the IDDRG Conference*. Bilbao.

Abspoel, M., Scholting, M. & Droog, J., 2013. A new method for predicting Forming Limit Curves from mechanical properties. *Journal of Materials Processing Technology*, 213(5), pp.759–769.

Allwood, J.M. & Shouler, D.R., 2009. Generalised forming limit diagrams showing increased forming limits with non-planar stress states. *International Journal of Plasticity*, 25(7), pp.1207–1230.

Arrieux, R. et al., 1985. Determination of the Strain Path Influence of the Forming Limit Diagrams, from the Limit Stress Curve. *CIRP Annals - Manufacturing Technology*, 34(1), pp.205–208.

Atzema, E. et al., 2002. Appreciation of the determination of the Forming Limit Curve. In *Numisheet*. Jeju Island, pp. 471–476.

Azrin, M. & Backofen, W.A., 1970. The deformation and failure of a biaxially stretched sheet. *Metallurgical Transactions*, 1(10), pp.2857–2865.

Baczynski, G.J. et al., 2000. Development of roping in an aluminum automotive alloy AA6111. *Acta Materialia*, 48(13), pp.3361–3376.

Banabic, D. et al., 2013. Development of a new procedure for the experimental determination of the Forming Limit Curves. *CIRP Annals - Manufacturing Technology*, 62(1), pp.255–258.

Banabic, D., 2010. *Sheet Metal Forming Processes* 2nd ed., Springer.

Banabic, D. & Dannenmann, E., 2001. Prediction of the influence of yield locus on the limit strains in sheet metals. *Journal of Materials Processing Technology*, 109(1-2), pp.9–12.

Banabic, D. & Vos, M., 2007. Modelling of the Forming Limit Band –A new Method to Increase the Robustness in the Simulation of Sheet Metal Forming Processes. *CIRP Annals - Manufacturing Technology*, 56(1), pp.249–252.

Barata da Rocha, A., Barlat, F. & Jalinier, J.M., 1985. Prediction of the forming limit diagrams of anisotropic sheets in linear and non-linear loading. *Materials Science and Engineering*, 68(2), pp.151–164.

Barlat, F., 1987. Crystallographic texture, anisotropic yield surfaces and forming limits of sheet metals. *Materials Science and Engineering*, 91(null), pp.55–72.

Barlat, F. & Lian, J., 1989. Plastic behaviour and stretchability of sheet metals (Part 1): A yield function for orthotropic sheet under plane stress conditions. *International Journal of Plasticity*, 5, pp.51–56.

Bragard, A., Baret, J.C. & Bonnarens, H., 1972. A simplified technique to determine the the FLD at onset of necking. *Centre for Research in Metallurgy*, 33, pp.53–63.

Chu, X., 2013. *Influence of Temperature and Strain Rate on the Formability of Aluminium Alloys: Comparison between Experimental and Predictive Results*.

Considère, M., 1885. L'emplou du fer et Lacier Dans Les Constructions (in French). *Annales Des Ponts et Chausses*, 9, pp.574–775.

D'Hayer, R. & Bragard, A., 1975. Determination of the limiting strains at the onset of necking. *Centre for Research in Metallurgy*, 42, pp.33–35.

Dantec, 2014. Q400. Available at: http://www.dantecdynamics.com/q-400-dic [Accessed November 24, 2014].

Department for Business Innovation and Skills, 2009. An Independent Report on the Future of the Automotive Industry in the UK. Available at: http://www.bis.gov.uk/files/file51139.pdf

[Accessed January 10, 2013].

Eberle, B., Volk, W. & Hora, P., 2008. Automatic approach in the evaluation of the experimental FLC with a full 2D approach based on a time depending method. In *Numisheet*. Interlaken, pp. 279–284.

European Aluminium Association, 2013. Aluminium in Cars: Unlocking the Light-Weighting Potential. Available at: http://www.alueurope.eu/wp-content/uploads/2012/10/EAA-Aluminium-in-Cars-Unlocking-the-light-weighting-potential.pdf [Accessed January 3, 2014].

European Commission, 2013. EU Transport in Figures: Statistical Pocketbook. Available at: http://ec.europa.eu/transport/facts-fundings/statistics/doc/2013/pocketbook2013.pdf [Accessed June 17, 2015].

Friedman, P.A. & Pan, J., 2000. Effects of plastic anisotropy and yield criteria on prediction of forming limit curves. *International Journal of Mechanical Sciences*, 42(1), pp.29–48.

Geiger, M. & Merklein, M., 2003. Determination of forming limit diagrams – a new analysis method for characterization of materials' formability. *CIRP Annals - Manufacturing Technology*, 52(1), pp.213–216.

Ghazanfari, A. & Assempour, A., 2012. Calibration of forming limit diagrams using a modified Marciniak–Kuczynski model and an empirical law. *Materials & Design*, 34, pp.185–191.

Ghosh, A.K., 1978. Plastic flow properties in relation to localised necking in sheets. In *Mechanics of Sheet Metal Forming*. pp. 287–311.

Ghosh, A.K., 1977. The Influence of Strain Hardening and Strain Rate Sensitivity on Sheet Metal Forming. In *Transactions of the ASME*. pp. 264–274.

Gioacchino, F. & Quinta da Fonseca, J., 2012. Plastic Strain Mapping with Sub-micron Resolution Using Digital Image Correlation. *Experimental Mechanics*, 53(5), pp.743–754.

GOM mbH, 2012. ARAMIS. Available at: http://www.gom.com/metrology-systems/system-overview/aramis.html [Accessed August 22, 2012].

Goodwin, G.M., 1968. Application of strain analysis to sheet metal forming problems in the press shop. In *SAE Paper 680093*.

Graf, A. & Hosford, W.F., 1990. Calculations of forming limit diagrams. *Metallurgical Transactions A*, 21(1), pp.87–94.

Graf, A. & Hosford, W.F., 1993. Effect of changing strain paths on forming limit diagrams of AL 2008-T4. *Metallurgical Transactions A*, 24(11), pp.2503–2512.

Graf, A. & Hosford, W.F., 1994. The influence of strain-path changes on forming limit diagrams of A1 6111 T4. *International Journal of Mechanical Sciences*, 36(10), pp.897–910.

Gronostajski, J.Z. & Zimniak, Z., 1992. The effect of changing of heterogeneity with strain on the forming limit diagram. *Journal of Materials Processing Technology*, 34(1-4), pp.457–464.

Grumbach, M. & Sanz, G., 1972. Influence of various parameters on forming limit curves. *Revue de Metallurgie*, 61, pp.273–290.

Guillotin, A. et al., 2011. Correlation of Surface Roping with Through-Thickness Microtextures in an AA6xxx Sheet. *Metallurgical and Materials Transactions A*, 42(7), pp.1919–1924.

Hecker, S.S., 1972. A simple forming limit curve technique and results on aluminium alloys. In *Proceedings of the IDDRG Conference*. Amsterdam, pp. 5.1–5.8.

Hill, R., 1948. A theory of the yielding and plastic flow of anisotropic metals. *Proceedings of the Royal Society*, 193, pp.281–297.

Hill, R., 1952. On discontinuous plastic states, with special reference to localized necking in thin

sheets. *Journal of the Mechanics and Physics of Solids*, 1(1), pp.19–30.

Hill, R., 1979. Theoretical plasticity of textured aggregates. *Mathematical Proceedings of the Cambridge Philosophical Society*, 85(01), p.179.

Hockett, J.E. & Sherby, O.D., 1975. Large strain deformation of polycrystalline metals at low homologous temperatures. *Journal of the Mechanics and Physics of Solids*, 23(2), pp.87–98.

Holloman, J.H., 1945. Tensile Deformation. *Transaction of the Society of Mining Enigneers*, 162, pp.268–272.

Holmberg, S., Enquist, B. & Thilderkvist, P., 2004. Evaluation of sheet metal formability by tensile tests. *Journal of Materials Processing Technology*, 145(1), pp.72–83.

Hopperstad, O.S. et al., 2007. A numerical study on the influence of the Portevin–Le Chatelier effect on necking in an aluminium alloy. *Modelling and Simulation in Materials Science and Engineering*, 15(7), pp.747–772.

Hosford, W.F., 1979. On yield loci of anisotropic cubic materials. In *Proceedings of the 7th North American Metalworking Conference*. Dearborn, pp. 191–197.

Hosford, W.F. & Caddell, R.M., 2011. *Metal Forming: Mechanics and Metallurgy* 4th ed., Cambridge University Press.

Hotz, W. & Timm, J., 2008. Experimental Determination of Forming Limit Curves (FLC). In *Numisheet*. Interlaken.

Hutchinson, J.W. & Neale, K.W., 1977. Influence of strain-rate sensitivity on necking under uniaxial tension. *Acta Metallurgica*, 25(8), pp.839–846.

Hutchinson, J.W. & Neale, K.W., 1978. Sheet Necking II. Time-independent behaviour. In *Mechanism of Sheet Metal Forming*. Plenum, pp. 127–153.

ISO12004-2, 2008. Metallic Materials - Sheet and Strip - Determination of Forming Limit Curves - Part 2: Determination of Forming Limit Curves in the Laboratory.

Jain, M., Lloyd, D.J. & MacEwen, S.R., 1996. Hardening laws, surface roughness and biaxial tensile limit strains of sheet aluminium alloys. *International Journal of Mechanical Sciences*, 38(2), pp.219–232.

Janssens, K. et al., 2001. Statistical evaluation of the uncertainty of experimentally characterised forming limits of sheet steel. *Journal of Materials Processing Technology*, 112, pp.174–184.

Keeler, S.P., 1961. *Plastic Instability and Fracture in Sheet Stretched Over Rigid Punches (PhD Thesis)*. Massachusetts Institute of Technology.

Keeler, S.P. & Backofen, W.A., 1963. Plastic instability and fracture in sheets stretched over rigid punches. *ASM Transactions*, 56, pp.25–98.

Kienzle, O. & Mietzner, K., 1967. *Atlas Umgeformter Metallischer Oberflächen*,

Kleemola, H.J. & Nieminen, M.A., 1974. On the strain-hardening parameters of metals. *Metallurgical Transactions*, 5(8), pp.1863–1866.

Koffler, C. & Rohde-Brandenburger, K., 2009. On the calculation of fuel savings through lightweight design in automotive life cycle assessments. *The International Journal of Life Cycle Assessment*, 15(1), pp.128–135.

Kohara, S., 2005. Influence of strain path on the forming-limit curve in aluminum. *Metallurgical and Materials Transactions A*, 36(4), pp.1033–1037.

Laukonis, J.V. & Ghosh, A.K., 1978. Effects of Strain Path Changes on the Formability of Sheet Metals. *Metallurgical Transactions A*, 9A, pp.1849–1856.

Lazarescu, L. et al., 2012. Characterization of plastic behaviour of sheet metals by hydraulic bulge

test. *Transactions of Nonferrous Metals Society of China*, 22, pp.s275–s279.

Lee, W.B. & Wen, X.Y., 2006. A dislocation-based model of forming limit prediction in the biaxial stretching of sheet metals. *International Journal of Mechanical Sciences*, 48(2), pp.134–144.

Leppin, C., Li, J. & Daniel, D., 2008. Application of a method to correct the effect of non-proportional strain paths in Nakazima test based forming limit curves. In *Numisheet*. Zurich, pp. 217–221.

Li, H., 2012. *A Study of Surface Roughness in the Metal Forming Process*. University of Wollongong.

Lian, J., Barlat, F. & Baudelet, B., 1989. Plastic behaviour and stretchability of sheet metals. Part II: Effect of yield surface shape on sheet forming limit. *International Journal of Plasticity*, 5(2), pp.131–147.

Marciniak, Z., 1965. Stability of plastic shells under tension with kinematic boundary condition. *Archiwum Mechaniki Stosorwanej*, 17, pp.577–592.

Marciniak, Z., Duncan, J.L. & Hu, S.J., 2002. *Mechanics of Sheet Metal Forming*, Butterworth-Heinemann.

Marciniak, Z. & Kuczyński, K., 1967. Limit strains in the processes of stretch-forming sheet metal. *International Journal of Mechanical Sciences*, 9(9), pp.609–620.

Marciniak, Z., Kuczyński, K. & Pokora, T., 1973. Influence of the plastic properties of a material on the forming limit diagram for sheet metal in tension. *International Journal of Mechanical Sciences*, 15(10), pp.789–800.

Mathworks, 2015. MATLAB Reference Documentation: fzero. Available at: http://uk.mathworks.com/help/matlab/ref/fzero.html.

McCormick, P.G. & Ling, C.P., 1995. Numerical modelling of the Portevin—Le Chatelier effect. *Acta Metallurgica et Materialia*, 43(5), pp.1969–1977.

Merklein, M., Kuppert, A. & Geiger, M., 2010. Time dependent determination of forming limit diagrams. *CIRP Annals - Manufacturing Technology*, 59(1), pp.295–298.

van Minh, H., Sowerby, R. & Duncan, J.L., 1974. Variability of forming limit curves. *International Journal of Mechanical Sciences*, 16(1), pp.31–44.

Moore, M. & Bate, P., 2002. Microstructural inhomogeneity and biaxial stretching limits in aluminium alloy AA6016. *Journal of Materials Processing Technology*, 125-126, pp.258–266.

Morales, D. et al., 2009. Bending effect in the failure of stretch-bend metal sheets. *International Journal of Material Forming*, 2(S1), pp.813–816.

Nakazima, K., Kikuma, T. & Hasuka, K., 1971. Forming limits under biaxial stretching of sheet metals. *Yawata Technical Report*, 284, pp.678–680.

Neale, K.W. & Chater, E., 1980. Limit strain predictions for strain-rate sensitive anisotropic sheets. *International Journal of Mechanical Sciences*, 22(9), pp.563–574.

Nurcheshmeh, M., 2011. *Numerical Prediction of Sheet Metal Forming Limits*. University of Windsor.

Osakada, K. & Oyane, M., 1971. On the Roughening of Free Surface in Deformation Processes. *Bulletin of JSME*, 14(68), pp.171–177.

Painter, M.J. & Pearce, R., 1974. Instability and fracture in sheet metal. *Journal of Physics D: Applied Physics*, 7(7), pp.992–1002.

Parmar, A. & Mellor, P.B., 1978. Predictions of limit strains in sheet metal using a more general yield criterion. *International Journal of Mechanical Sciences*, 20(6), pp.385–391.

Parmar, A., Mellor, P.B. & Chakrabarty, J., 1977. A new model for the prediction of instability and limit strains in thin sheet metal. *International Journal of Mechanical Sciences*, 19(7), pp.389–398.

Pearce, R., 1970. A User's Guide to the FLD. *Sheet Metal Industries*, 48, pp.943–949.

Priadi, D. et al., 1992. A new tensile test on notched specimens to assess the forming limit diagram of sheet metals. *Journal of Materials Processing Technology*, 32(1-2), pp.279–288.

Raabe, D. et al., 2003. Grain-scale micromechanics of polycrystal surfaces during plastic straining. *Acta Materialia*, 51(6), pp.1539–1560.

Raghavan, K.S., 1995. A simple technique to generate in-plane forming limit curves and selected applications. *Metallurgical and Materials Transactions A*, 26(8), pp.2075–2084.

Sowerby, R., Chu, E. & Duncan, J.L., 1982. Determination of large strains in metalforming. *The Journal of Strain Analysis for Engineering Design*, 17(2), pp.95–101.

Sowerby, R. & Duncan, J.L., 1971. Failure in sheet metal in biaxial tension. *International Journal of Mechanical Sciences*, 13(3), pp.217–229.

Stoudt, M.R. et al., 2011. The fundamental relationships between grain orientation, deformation-induced surface roughness and strain localization in an aluminum alloy. *Materials Science and Engineering: A*, 530, pp.107–116.

Stoudt, M.R. & Ricker, R.E., 2002. The relationship between grain size and the surface roughening behavior of Al-Mg alloys. *Metallurgical and Materials Transactions A*, 33(9), pp.2883–2889.

Stoughton, T.B. & Yoon, J., 2012. Path independent forming limits in strain and stress spaces. *International Journal of Solids and Structures*, 49(25), pp.3616–3625.

Stoughton, T.B. & Yoon, J.W., 2005. Sheet metal formability analysis for anisotropic materials under non-proportional loading. *International Journal of Mechanical Sciences*, 47(12), pp.1972–2002.

Strano, M. & Colosimo, B.M., 2006. Logistic regression analysis for experimental determination of forming limit diagrams. *International Journal of Machine Tools and Manufacture*, 46, pp.673–682.

Swift, H.W., 1952. Plastic instability under plane stress. *Journal of the Mechanics and Physics of Solids*, 1(1), pp.1–18.

Tadros, A.K. & Mellor, P.B., 1978. An experimental study of the in-plane stretching of sheet metal. *International Journal of Mechanical Sciences*, 20(2), pp.121–133.

Tadros, A.K. & Mellor, P.B., 1975. Some comments on the limit strains in sheet metal stretching. *International Journal of Mechanical Sciences*, 17(3), pp.203–210.

Tasan, C.C. et al., 2014. Strain localization and damage in dual phase steels investigated by coupled in-situ deformation experiments and crystal plasticity simulations. *International Journal of Plasticity*, 63, pp.198–210.

Tharrett, M.R. & Stoughton, T.B., 2003. Stretch-bend forming limits of 1008 AK steel, 70/30 brass, and 6010 aluminium. In *Proceedings of Plasticity 2003: The 10th International Symposium on Plasticity and its Current Applications*. pp. 567–569.

The AutoSteel Partnership, 2003. *Report of Enhanced Forming Limit Diagram Project*,

Tóth, L.S., Hirsch, J. & Van Houtte, P., 1996. On the role of texture development in the forming limits of sheet metals. *International Journal of Mechanical Sciences*, 38(10), pp.1117–1126.

Tvergaard, V., 1978. Effect of kinematic hardening on localized necking in biaxially stretched sheets. *International Journal of Mechanical Sciences*, 20(9), pp.651–658.

United Nations Framework Convention on Climate Change, 1998. Kyoto protocol to the United Nations framework convention on climate change. Available at: http://kyotoprotocol.com/resource/kpeng.pdf [Accessed March 28, 2012].

Vacher, P., Haddad, A. & Arrieux, R., 1999. Determination of the Forming Limit Diagrams Using

Image Analysis by the Corelation Method. *CIRP Annals - Manufacturing Technology*, 48(1), pp.227–230.

Veerman, C., 1971. Determination of appearing and admissable strains in cold-reduced sheets. *Sheet Metal Industries*, pp.687–694.

ViALUX GmbH, 2012. AutoGrid in-process. Available at: http://www.vialux.de/HTML/en_vario.htm [Accessed August 22, 2012].

Voce, E., 1948. The relationship between stress and strain for homogeneous deformation. *Journal of the Institute of Metals*, 74, p.537.

Volk, W. et al., 2012. Failure prediction for nonlinear strain paths in sheet metal forming. *CIRP Annals - Manufacturing Technology*, 61(1), pp.259–262.

Volk, W., 2006. New experimental and numerical approach in the evaluation of the FLC with the FE-method. In *FLC-Zurich*. Zurich, pp. 26–30.

Volk, W. & Hora, P., 2010. New algorithm for a robust user-independent evaluation of beginning instability for the experimental FLC determination. *International Journal of Material Forming*, 4(3), pp.339–346.

Wang, K. et al., 2014. Measuring forming limit strains with digital image correlation analysis. *Journal of Materials Processing Technology*, 214(5), pp.1120–1130.

Wilson, D. V., Roberts, W.T. & Rodrigues, P.M.B., 1981. Effect of Grain anisotropy on limit strains in biaxial stretching: part i. influence of sheet thickness and grain size in weakly textured sheets. *Metallurgical Transactions A*, 12(9), pp.1595–1602.

Wittridge, N.. & Knutsen, R.., 1999. A microtexture based analysis of the surface roughening behaviour of an aluminium alloy during tensile deformation. *Materials Science and Engineering: A*, 269(1-2), pp.205–216.

Woodthorpe, J. & Pearce, R., 1970. The effect of r and n upon the FLD of sheet steel. In *Proceedings of the ICTIS Conference*. Tokyo, pp. 822–827.

Yamaguchi, K., Takakura, N. & Imatani, S., 1995. Increase in forming limit of sheet metals by removal of surface roughening with plastic strain (Balanced biaxial stretching of aluminium sheets and foils). *Journal of Materials Processing Technology*, 48(1-4), pp.27–34.

Yoshida, K., 2014. Effects of grain-scale heterogeneity on surface roughness and sheet metal necking. *International Journal of Mechanical Sciences*, 83, pp.48–56.

Yoshida, K., Kuwabara, T. & Kuroda, M., 2007. Path-dependence of the forming limit stresses in a sheet metal. *International Journal of Plasticity*, 23(3), pp.361–384.

Zhang, L. & Wang, J., 2012. Modeling the localized necking in anisotropic sheet metals. *International Journal of Plasticity*, 39(null), pp.103–118.

Zhao, L., Sowerby, R. & Sklad, M.P., 1996. A theoretical and experimental investigation of limit strains in sheet metal forming. *International Journal of Mechanical Sciences*, 38(12), pp.1307–1317.